PARTICLE DYNAMICS IN INERTIAL MICROFLUIDICS

vorgelegt von
Master of Science

Christian Schaaf

ORCID: 0000-0002-4154-5459

an der Fakultät II – Mathematik und Naturwissenschaften
der Technischen Universität Berlin
zur Erlangung des akademischen Grades
Doktor der Naturwissenschaften
– Dr. rer. nat. –

genehmigte Dissertation

Promotionsausschuss:

Vorsitzender:	Prof. Dr. Michael Lehmann
Erster Gutachter:	Prof. Dr. Holger Stark
Zweiter Gutachter:	Prof. Dr. Roland Netz

Tag der wissenschaftlichen Aussprache: 17. September 2020

Berlin 2020

Zusammenfassung

Die inertiale Mikrofluidik beschäftigt sich mit laminaren Strömungen von Flüssigkeiten durch mikroskopische Kanäle, bei denen die Trägheitseffekte der Flüssigkeit nicht vernachlässigt werden können. Befinden sich Teilchen in diesen inertialen Strömungen, ordnen sie sich von selbst an bestimmten Positionen auf der Querschnittsfläche an. Da diese Gleichgewichtspositionen von den Teilcheneigenschaften abhängen, können so beispielsweise Zellen voneinander getrennt werden.

In dieser Arbeit beschäftigen wir uns mit der Dynamik mehrerer fester Teilchen, sowie dem Einfluss der Deformierbarkeit auf die Gleichgewichtsposition einer einzelnen Kapsel. Wir verwenden die *Lattice-Boltzmann*-Methode, um dieses System zu simulieren.

Einen wichtigen Grundstein für das Verständnis mehrerer Teilchen bildet die Dynamik von zwei festen Partikeln. Zunächst klassifizieren wir die möglichen Trajektorien, von denen drei zu ungebundenen Zuständen führen und eine über eine gedämpfte Schwingung in einem gebundenem Zustand endet. Zusätzlich untersuchen wir die inertialen Hubkräfte, welche durch das zweite Teilchen stark beeinflusst werden. Dieser Einfluss hängt vor allem vom Abstand der beiden Teilchen entlang der Flussrichtung ab.

Im Anschluss an die Dynamik beschäftigen wir uns genauer mit der Stabilität von Paaren und Zügen bestehend aus mehreren festen Teilchen. Wir konzentrieren uns auf Fälle, in denen die Teilchen sich lateral bereits auf ihren Gleichgewichtspositionen befinden, jedoch nicht entlang der Flussrichtung. Paare von festen Teilchen, welche sich auf den unterschiedlichen Seiten des Kanals anordnen, ziehen sich auch über große Abstände hinweg an, während sich Teilchen auf der gleichen Kanalseite voneinander entfernen. Das Zusammenziehen eines zigzagartigen Teilchenzugs entsteht durch die kollektive Minderung des Strömungswiderstandes. Lineare Teilchenzüge treiben langsamer auseinander als die entsprechenden Paare. Außerdem beobachten wir, dass sich das führende Teilchen vom Rest des Zuges trennt. Zuletzt untersuchen wir, wie Störungen durch den Teilchenzug wandern.

Im letzten Teil dieser Arbeit betrachten wir eine einzelne, deformierbare Kapsel. Die Deformierbarkeit führt zu einer zur Kanalmitte gerichteten Kraft, während die inertiale Hubkraft die Kapsel nach außen treibt. Welche Kraft dabei dominiert, wird durch die Steifigkeit der Kapsel bestimmt. Wir untersuchen, wie sich die Deformierbarkeit auf die Gleichgewichtsposition sowie die Hubkräfte auswirkt. Wir zeigen, dass die Deformierbarkeit das Skalierungsverhalten der Hubkraft nicht beeinflusst und dass sich die Kraft in einen inertialen Anteil sowie einen Beitrag für die Deformierbarkeit zerlegen lässt. Zuletzt demonstrieren wir, wie die Gleichgewichtslage mithilfe einer externen Kraft entlang der Kanalachse beeinflusst werden kann.

Abstract

Inertial microfluidics deals with laminar fluid flows through microscopic channels where the inertial effects of the fluid cannot be neglected. Particles in an inertial flow assemble at specific positions on the cross-sectional plane. Since these equilibrium positions depend on particle properties, such devises can be used to sort and separate particles.

In this thesis we study the dynamics of multiple rigid particles and the influence of deformability on the equilibrium position of a single capsule. We use the *lattice-Boltzmann* method to simulate this system.

We start our analysis with the dynamics of two rigid particles, which provides a first basis to understand the behavior of multiple particles. First, we classify the possible trajectories, of which three lead to unbound states and one ends in a bound state via damped oscillations. Additionally, we investigate the inertial lift forces acting on the particles which are strongly influenced by the second particle. This influence depends mainly on the axial distance between the two particles along the flow direction.

Subsequently to the dynamics we study the stability of pairs and trains consisting of multiple rigid particles. We concentrate on the case where the particles are already at their lateral equilibrium positions, but are initialized with a non-equilibrium axial spacing. Pairs of rigid particles where the particles are located on opposite sides of the channel attract each other even over large distances, while particles on the same side of the channel move away from each other. The contraction of staggered particle trains is related to collective drag reduction and happens non-uniformly. For linear particle trains, the spreading apart is slower compared to same-streamline pairs. Furthermore, we observe that the leading particle separates from the rest of the train. Finally, we investigate how a displacement pulse migrates through a staggered particle train.

In the last part of this thesis we consider a single deformable capsule. The deformability results in a force that is directed toward the center of the channel, while the inertial lift force pushes the particle outward. The dominating force is determined by the stiffness of the particle. We study how deformability affects the equilibrium position and its influence on the lift force. The deformability does not only affect the distance to the channel center, but also the location of the equilibrium position in channels with a rectangular cross section. We show that the lift force scales like the force for rigid particles and that it can be decomposed into an inertial part and a contribution due to deformability. Finally, we demonstrate how the equilibrium position can be tuned by an external force along the channel axis.

Acknowledgment

At this point I wish to express my gratitude to those who supported me in the preparation of my doctoral thesis.

First, I would like to acknowledge the continuing support by Prof. Dr. Holger Stark. His supervision and guidance played a vital role in shaping this work. He gave me the freedom to pursue my interests and enabled me to present my work at multiple occasions. I am grateful to Prof. Dr. Roland Netz, who kindly examined this work, and Prof. Dr. Michael Lehmann, who chaired the committee.

During my time at the TU Berlin I had the privilege of working with great colleagues. My special thanks go to Reinier van Buel and Felix Rühle for the many interesting discussions and for their help in improving this thesis. I am thankful for my room neighbors Josua Grawitter and Arne Zantop who always had time to discuss a problem. The bureaucratic challenges were significantly simplified by Maximilian Seyrich, who documented the registration processes in our Wiki. I also thank Christopher Prohm for his preparatory work and for providing me a well-documented code.

I also want to thank the members of my former group of Prof. Dr. Stephan Gekle and the group of Prof. Dr. Walter Zimmermann at the University of Bayreuth: Achim Guckenberger, Christian Bächer, Matthias Laumann and Andre Förtsch. Their insights in the behavior of deformable capsules were of great help during my thesis.

As a simulation project, this thesis heavily relies on a functioning IT infrastructure. Peter Orlowski and the team of the computing cluster of the Faculty II always made sure that this infrastructure was working, and they also had some patience with me running out of hard disk space.

Of course, the thesis wouldn't have been possible without funding. For this I thank the German Research Foundation, which supported me in the framework of the Collaborative Research Center SFB910.

The earliest and longest contribution was surely by my parents. Their support and great effort for my education brought me here. I am grateful to my sister Laura for being who she is; an inspiring and joyful companion.

Finally, I want to thank my girlfriend Miriam Jahn. There are no words to express my gratitude for her. Her constant support and company kept me going throughout this thesis.

Contents

List of Figures

List of Tables

"Scientists have long been baffled by the existence of spontaneous order in the universe. The laws of thermodynamics seem to dictate the opposite, that nature should inexorably degenerate toward a state of greater disorder, greater entropy. Yet all around us we see magnificent structures – galaxies, cells, ecosystems, human beings – that have somehow managed to assemble themselves."

Steven Strogatz - Sync

1

Introduction

Whenever order emerges from disorder, scientists are intrigued by the underlying principles [1]. One example of such a process is the inertial focusing named Segré-Silberberg effect [2]. It describes the focusing of an initially uniform distribution of particles on an annulus when the particles flow through a pipe, which provides a simple yet effective way to study and analyze biological cells. This thesis focuses on the dynamics and stability of multi-particle trains and the behavior of a single deformable capsule in inertial microfluidics.

Inertial focusing was first observed experimentally in the 1960s [2, 3]. The two physical chemists, Segré and Silberberg, investigated the flow of particle suspensions in a cylindrical tube. The particles assembled around half-way between the channel center and the walls, independently of their initial distribution. In addition, the particles formed regular trains with a specific spacing along the flow direction. The physical cause of this effect was initially unclear [4]. Although Segré and Silberberg already assumed that the focusing was caused by inertia, it took 28 years and several analytical approaches to identify the exact cause of the migration: a combination of the inhomogenous shear gradient and wall effects [5–8]. At the beginning of the last decade interest in inertial focusing was renewed as technical advances enabled the production of microfluidic devices which withstand the high pressure gradients necessary for the inertial regime.

The field of microfluidics deals with liquids on the μm to mm scale which are often pumped through narrow channels. Common research topics are analysis of blood flow [9, 10] and creation of immiscible droplets [11]. Due to the small dimensions of the channel and the usually small flow rate, inertia of the fluid is typically neglected in microfluidic models [12]. However, technical progress made it possible to produce microchannels that withstand high pressures and thus generate the shear gradients necessary for inertial focusing [13]. A technical application of microfluidic channels is a so-called lab-on-a-chip device, which combines one or more laboratory tests on an area roughly the size of a credit card [14].

An exciting and promising application of lab-on-a-chip devices and inertial microfluidics involves the medical analysis of cells. In the Segré-Silberberg effect the equilibrium positions depend on the inherent properties of the particle like its size or its deformability [15,

16]. Deformability is of particular interest, as it is closely connected to the function and state of the cell [17, 18]. Deformability can thus serve as an intrinsic biophysical marker for infections and diseases. Metastatic cancer cells, for example, are often more compliant than corresponding healthy cells [19, 20], whereas malaria-infected red blood cells are stiffer than uninfected red blood cells [21].

Using deformability as a marker has the advantage that the diagnosis is based on an intrinsic property of the cell [22]. While for conventional biochemical markers the details of a disease must already be well understood, the mechanical properties of cells can be determined empirically [23, 24]. However, since mechanical properties also vary widely in healthy cells, a large number of cells must be analyzed to obtain a reliable diagnosis. In addition, blood contains a variety of different cell types and the concentration of cells of interest may be low [25]. For instance, one medical study counts only 1–500 circulating tumor cells per milliliter of blood [26]. This is where the high flow rates of inertial microfluidics has another advantage, as it allows the analysis of up to 4 ml/min or 6 000 000 cells/s [27]. Using the Segré-Silberberg effect to sort out irrelevant cells and thereby increase the concentration of infected cells allows the use of less sensitive and often cheaper analysis methods [16, 28, 29]. Furthermore, the formation of regular particle trains during the inertial focusing simplifies counting cells or enclosing them in an analysis solution in order to study them in a well-defined chemical environment [30, 31].

In addition to biomedical applications, the physics of inertial microfluidics itself is intriguing. The inertia of the fluid is not negligible as a consequence of high flow velocities. Still, the flows are laminar so that the system evolves deterministically. Due to the non-linearity in the governing Navier-Stokes equations analytical solutions are only possible in limiting cases and results are mostly obtained by experiments [15, 32, 33] and simulation [34–36]. With these tools, the Segré-Silberberg effect for a single solid particle is well understood. It is thoroughly analyzed how the number of equilibrium positions changes with the cross section of the channel [37, 38] and the lift forces acting on a solid particle are well understood [35, 39]. For about 10 years, trains of particles have been investigated in detail [40–42]. The research on particle trains mostly focuses on explaining the spacing between the particles [43–45]. However, the dynamics of multiple particles and the influence of deformability are still open questions.

In this thesis we address two main questions: what determines the interaction between particles in the inertial regime and how does the deformability of particles affect their dynamics? We focus our analysis on straight channels with a quadratic or rectangular cross section. To solve the Navier-Stokes equations we use the lattice-Boltzmann method.

Regarding the particle interaction we study the dynamics and stability of rigid particle pairs and trains. Typical multi-particle structures are shown in Fig. 1.1. Since the typical density in inertial microfluidic experiments is low, multi-particle interactions are dominated by pair interactions. First we concentrate on two particles and determine the different types of trajectories occurring in this system. Depending on the initial conditions, the trajectories lead to either bound or unbound configurations, where the particles form stable pairs or slowly drift apart. In the bound configuration the particles are located on opposite sides of the channel forming a cross-streamline pair. The analysis of bound trajectories suggests
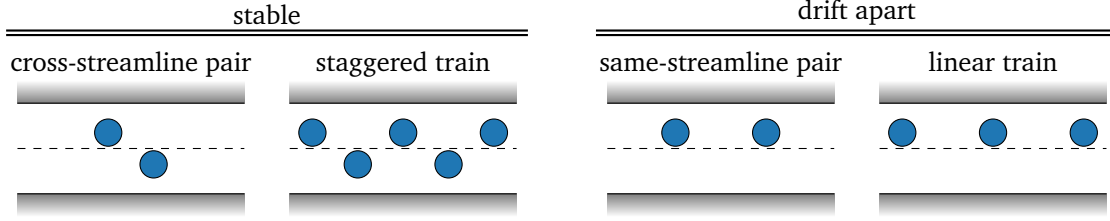
Figure 1.1: Illustration of possible multi-particle structures in inertial channel flow. **Left:** Cross-streamline pairs and staggered trains form stable configurations with a distinct equilibrium distance. **Right:** Same-streamline pairs and linear trains quickly expand to a characteristic axial distance about twice of the distance of cross-streamline pairs and then slowly drift further apart.

that the dynamics of particles is driven by viscous forces, whereas fluid inertia leads to specific equilibrium positions. Furthermore, we analyze the two-particle lift force profiles. The lift forces increase in strength compared to the single-particle lift forces, and we find an asymmetry of the forces acting on the leading and lagging particle. The influence of the second particle on the lift force profile decays rapidly with increasing axial spacing. The scaling of the lift force confirms our previous observation that the dynamics of the particles is determined by viscous forces when they are close together. Only when the distance increases the scaling indicates that inertia becomes dominant.

Our findings for the bound trajectories agree with results published in a study at the same time [46]. However, we also obtained results which contradict the current view in the literature, namely we classify states as unbound which appear to be stable in experiments. To further clarify this contradiction, we continue our analysis and focus on the stability of pairs and multi-particle trains. We confirm the stability of cross-streamline pairs by showing how they contract or expand to their equilibrium axial distance. In contrast, same-streamline pairs quickly expand to a characteristic separation, but at long times slowly drift apart. We reproduce the distribution of particle distances with its characteristic peak as measured in experiments [47].

Staggered multi-particle trains initialized with an axial particle spacing larger than the equilibrium distance contract non-uniformly due to collective drag reduction. Linear particle trains, similar to particle pairs, rapidly expand toward a value about twice the equilibrium distance of staggered trains and then slowly drift apart non-uniformly. Again, we reproduce the statistics of particle distances and the characteristic peak observed in experiments [42]. Finally, we thoroughly analyze the damped displacement pulse traveling as a microfluidic phonon through a staggered train and show how a defect strongly damps its propagation.

For the second question, on how deformability influences the Segré-Silberberg effect, we consider a single deformable capsule governed by Skalak's constitutive model [48]. It is important to note that deformable particles, unlike solid particles, migrate across streamlines even when the inertia of the fluid is negligible [49, 50]. Typically, deformable cells migrate to the center of the channel. In this part we are interested in how this inward-directed deformability-induced migration compensates the outward-directed migration of

the Segré-Silberberg effect. As expected, we observe that a softer particle assembles closer to the channel center than a rigid particle. For a channel with quadratic cross section we find a master curve for the equilibrium distance making the results independent of the ratio of inertia and viscous damping. In the case of rectangular channel cross sections the deformability of the particles has a strong influence on the location of the equilibrium position. While solid particles are arranged along the short main axis of the channel, soft particles tend to migrate to the long main axis of the cross section.

A detailed analysis of the lift forces shows that the lift force on a deformable particle behaves similar to the one acting on a rigid particle. The lift force acting on a deformable capsule can be decomposed into an inertial part and a contribution due to deformability. Finally, we demonstrate that the Saffman effect allows us to tune the equilibrium distance of a capsule by using an external force directed along the flow.

The remainder of this work is structured as follows:

Chapter 2 briefly discusses the technical applications of inertial microfluidics and introduces the basic physical concepts of this work. We continue by reviewing the underlying mechanisms and models for inertial migration and end this chapter with a short summary of the modeling and behavior of deformable particles.

Chapter 3 covers the mesoscopic description of the Boltzmann equations and introduces the lattice-Boltzmann method, which we use to simulate our system. We discuss the fundamentals of this method and focus on how to implement moving interfaces.

Chapter 4 is dedicated to the dynamics of a pair of rigid particles. We determine the different types of trajectories, which depend on the initial configuration, and analyze the two-particle lift force profiles. This chapter is based on my article Ref. [B].

Chapter 5 focuses on the stability of multi-particle structures. We first extend our analysis of pairs and apply these considerations to trains of multiple particles. The last point of this chapter is the analysis of a damped displacement pulse traveling through the train. This chapter is based on my article Ref. [C].

Chapter 6 deals with a single deformable particle. We analyze the influence of deformability on the equilibrium position of the particle. In addition, we determine the lift forces acting on the deformable particle. Finally, we investigate how the equilibrium position can be influenced by an external force. This chapter is based on my article Ref. [A].

Chapter 7 concludes this work and summarizes the results.

2

Basics of inertial microfluidics

Inertial microfluidic devices utilize the effects of fluid inertia on a microscale to sort and align particles or to mix fluids. The non-zero fluid inertia and the still laminar flow profile lead to a deterministic alignment and sorting of particles in the plane perpendicular to the flow and sometimes also in axial direction. Thus, inertial microfluidics is especially well suited for biological and medical applications where it can be used to sort cells based on the inherent properties of particles such as size or deformability. In this chapter we first introduce the idea of lab-on-a-chip devices and briefly review the current understanding of particles in inertial microfluidics. After discussing the governing equations for fluids and particles in the flow, we show that cross-streamline migration can only be explained by inertial effects. We then take a closer look at the individual migration mechanisms of inertial microfluidics. Finally, we briefly summarize the migration mechanism special to deformable capsules.

2.1 Lab-on-a-chip devices

In recent years, medical studies revealed that many diseases change the mechanical properties of cells. One prominent example is the reduced stiffness of *circulating tumor cells* compared to healthy cells [19, 20]. Another example are malaria-infected red blood cells which get stiffer due to the malaria parasite. The question now arises: Is it possible to diagnose diseases based on their effect on the mechanical properties of cells? This is one of the motivations driving this work.

To provide a reliable diagnosis, the method has to detect abnormal cells with a high degree of certainty. For blood tests it is favorable that small samples suffice to run the analysis. Besides these obvious requirements, the health care system, especially in poorer countries, demands for a diagnosis method that is inexpensive, fast, and versatile [51]. Ideally it can be carried out without trained personnel. Promising candidates to meet all these requirements are microfluidic lab-on-a-chip devices [52].

A lab-on-a-chip device integrates one or more laboratory functions on a single chip. These devices are only a few millimeters to centimeters in size. They employ hydrodynamics,

optics or chemical processes on a microscale. Hydrodynamic lab-on-a-chip devices are often made of polymers and contain small channels that can be cast or etched [13, 53]. Depending on the task, different channel designs are available [52, 54]. Possible choices are rectangular channels with varying cross section, spiraling or serpentine channels.

These lab-on-a-chip devices exactly fulfill the above stated requirements. They only require small amounts of fluids to operate (10^{-9} to 10^{-18} l) [14] and typically rely on passive mechanisms. The passive nature of the process enables fast and highly parallel assays so that a single lab-on-a-chip device can analyze up to $\sim 100\,000$ particles per second [55, 56]. In the future, laboratories could use the lab-on-a-chip modules as *plug & play* devices like we used to do with different floppy disks in early computers. Besides the technical application, lab-on-a-chip devices show fascinating physical phenomena, since the small scale of the microfluidic channels significantly changes the hydrodynamic interactions compared to the macroscopic scale.

2.2 Fluid inertia on the microscale

In our daily life we are used to hydrodynamics dominated by fluid inertia. In contrast, on the micron scale fluids are typically dominated by viscous forces [12]. The ratio of fluid inertia to viscous damping is captured by the Reynolds number

$$\mathrm{Re} = \frac{LU}{\nu} \, , \tag{2.1}$$

where L is the characteristic length scale and U is the characteristic speed. The fluid kinematic viscosity ν quantifies the internal friction of the fluid. Large Reynolds number ($\mathrm{Re} > 1 \cdot 10^5$) correspond to turbulent behavior [57]. For small Reynolds numbers ($\mathrm{Re} \ll 1$) the viscous damping is dominant, which is often the case in biological systems such as blood flow and the movement of bacteria. The distinctive swimming techniques of microorganisms compared to humans or fish illustrate the different fluid characteristics of both regimes [58].

There are two physical quantities describing the viscosity of a fluid: the kinematic viscosity ν and the dynamic viscosity η. Both are connected via the density ρ of the fluid

$$\eta = \rho \cdot \nu \, . \tag{2.2}$$

The dynamic viscosity η is commonly used in the physical description of fluids. However, we mainly write the equations with the kinematic viscosity ν, as this quantity is an intrinsic parameter of our simulation method.

Until the beginning of this century, microfluidic devices typically had channel dimensions of $l \approx 10\,\mu\mathrm{m}$, flow speeds of $u \approx 100\,\mu\mathrm{m/s}$ and fluid viscosity of $\nu = 10^{-6}\,\mathrm{m}^2/\mathrm{s}$. This leads to a Reynolds number $\mathrm{Re} \approx 1 \cdot 10^{-3}$, thus, fluid inertia was usually neglected. The prevailing opinion at that time is well summarized by Squires and Quake who noted in 2005 [12]:

> *"Of all dimensionless numbers, the Reynolds number is the one most often mentioned in connection with microfluidics. Ironically, it may also be the least interesting number for microfluidics: after all, almost without exception, microfluidic devices employ fluids with Reynolds numbers that are small enough for inertial effects to be irrelevant."*

Only two years later the advances in the production process of the channels and the realization of high throughput opened the field of inertial microfluidics [53].

In an inertial microfluidic device the flow speed reaches typical values of $u \approx 1\,\text{m/s}$ and Reynolds numbers $\text{Re} \approx 10 - 100$ [53, 55]. The finite fluid inertia rapidly extended the possible applications of lab-on-a-chip devices, which allow fluids to be mixed at the microscopic scale, move particles from one medium to another, and separate particles of different properties from each other. Without inertia, these applications require using special geometries [59, 60] or viscoelastic fluids [61–63].

In this thesis we focus on questions related to sorting particles. This is important for the previously introduced diagnosis methods, which rely on the mechanical properties of pathological cells. In the following we discuss the history of inertial microfluidics relevant for this work and outline the main effects.

2.3 An introduction to inertial focusing

The effect of inertial focusing was first observed in 1961 by Segré and Silberberg. Starting from a uniform distribution of mm-sized particles flowing through a 1 cm wide cylindrical pipe they observed the formation of an annulus around half-way between the channel center and the walls [2, 3]. The authors varied the Reynolds number between 4 and 520 [64].

The lateral migration was unexpected at the time. The formation of the annulus hinted at the existence of two opposing contributions which exactly compensate at the annulus. When the authors plotted the measured particle distributions against the Reynolds number, the results collapsed onto a master curve. Experiments with a similar setup but at lower Reynolds number did not report any migration for rigid particles [4]. The master curve and the addition experiments indicated that the effect was dominated by the inertia of the fluid. The formation of the annulus is called Segré-Silberberg effect. It took another 13 years and multiple analytical calculations [5, 6] until the effect could be explained as a combination of the inhomogeneous shear gradient and repulsive wall interactions acting on the particles [7]. We review the underlying migration mechanism in Sec. 2.5.5.

To show that the effect of inertial migration is not expected from our everyday life experience we perform a thought experiment. Segré and Silberberg used a cylindrical channel with a radius of $R = 5.6\,\text{mm}$ and a very viscous fluid ($\nu = 364 \cdot 10^{-6}\,\text{m}^2\text{/s}$). They varied the Reynolds number by choosing different flow velocities. For example a mean flow speed of $\bar{u} = 47.8\,\text{cm/s}$ yields a Reynolds number of $\text{Re} = 2R\bar{u}/\nu = 14.7$. If we increase the channel radius by one order of magnitude ($R = 5.6\,\text{cm}$) one would

Table 2.1: Typical experimental parameters for inertial microfluidics.

Channel dimension	Particle radius	Flow speed	Reynolds number	Ref.
$20\,\mu$m $\times$ $20\,\mu$m $\times$ 4 cm	$0.9\,\mu$m	0.05–2 m/s	1–40	[67]
$50\,\mu$m $\times$ $50\,\mu$m $\times$ 4 cm	$2.1\,\mu$m	0.02–2 m/s	1–100	[68]
$35\,\mu$m $\times$ $60\,\mu$m $\times$ 3 cm	$6\,\mu$m	0.9–3.4 m/s	30–120	[42]
$80\,\mu$m $\times$ $80\,\mu$m $\times$ 60 cm	2.7–$4.4\,\mu$m	0.001–5.25 m/s	0.07–280	[43]
$152\,\mu$m $\times$ $275\,\mu$m $\times$ 6 cm	$30\,\mu$m	0.15–3.6 m/s	21–500	[44]

need a flow velocity of 4.78 m/s to realize the same shear gradient. If the experiment is run with water ($\nu = 10^{-6}\,\text{m}^2$/s) instead of a highly viscous fluid, the Reynolds number yields Re $\sim$ 500 000. Such a high Reynolds number describes a highly turbulent channel flow where inertial migration could not be observed. Even if we use a more viscous fluid, like olive oil ($\nu \approx 82 \cdot 10^{-6}\,\text{m}^2$/s at 20 °C [66]), the corresponding Reynolds number (Re $=$ 3365) would still be in the turbulent regime. Although the required flow rate for a larger channel can be achieved, the resulting flow would be chaotic and turbulent and thus inertial migration could not be observed.

The previous thought experiment shows that it is difficult to utilize the Segré-Silberberg effect on a macroscopic scale, as one needs a highly viscous fluid to suppress turbulence. However, on the microscale one can run inertial experiments with water, making it suitable for medical applications.

Due to the advances in material design and production processes around the beginning of this century it was possible to create the necessary shear rates and open the field of inertial microfluidics [39, 53]. We list some typical experimental parameters for inertial microfluidics in Tab. 2.1. The self-organizing Segré-Silberberg effect allows a highly efficient sorting process of particles. While possible applications are mostly in the area of soft particles, current research concentrates mainly on rigid particles, as these have a reduced complexity.

Inertial migration of a rigid particle is explained by the inertial lift force profile, which acts perpendicular to the flow direction (see Fig. 2.1) [39]. The force profile has an unstable fixed point in the channel center and two off-centered stable fixed points. The existence of the stable fixed points indicates a combination of two opposing forces. The outwards directed force can heuristically be explained by a dynamic pressure difference across the particle surface caused by the flow profile. At the equilibrium positions this outwards-

Figure 2.1: Sketch of the lift force profile as a function of the lateral position perpendicular to the flow direction along the short channel axis. The zero crossings correspond to the equilibrium positions with an unstable fixed point in the channel center and two symmetric off-centered fixed points.
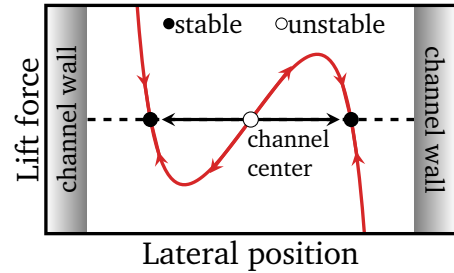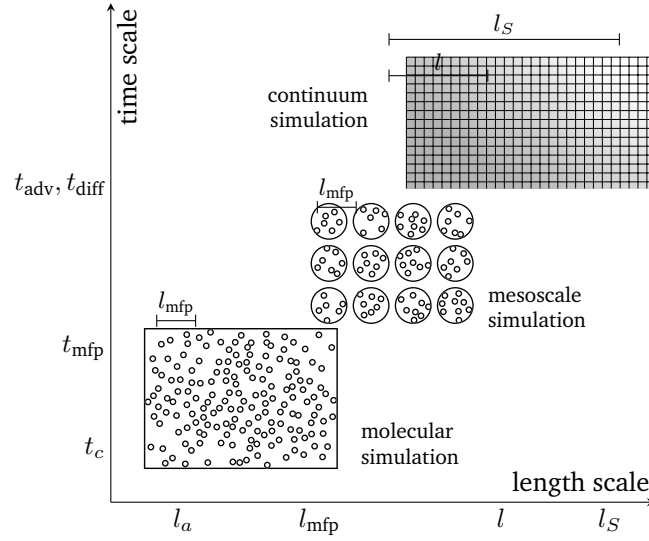
Figure 2.2: Hierarchy of length and time scales within a fluid. Depending on the required resolution different simulation methods are suitable. Adapted from Ref. [69].

directed force is compensated by repulsive particle-wall interaction. For a cylindrical channel this leads to the formation of the annulus of particles reported by Segré and Silberberg [2]. In Sec. 2.5.5 we discuss the underlying processes in more detail.

When the particle density is increased the particles start to interact and form microfluidic crystals or trains [40, 47]. The particles either align on alternating sides of the channel (staggered trains) or all particles assemble at the same side of the channel (linear trains), as illustrated in Ch. 1 (*cf.* Fig. 1.1). Typically, in experiments and simulations a mixture of both types of trains is observed. The particles in these trains assemble with a fixed axial distance ranging from 2.2 to 5 particle diameters for staggered trains and about twice this distance for linear trains [41, 42]. This regular axial spacing simplifies particle counting or cell manipulation [30]. Trains are observed at small particle densities with typical volume fractions between 0.02 to 1 % [42, 43]. In this case, pair interactions of the particles provide an initial step for understanding the dynamics and stability of multi-particle trains. We analyze the interactions for a pair of particles in Ch. 4 and for multiple particles in Ch. 5. Before we look into the details of inertial migration, we introduce the basic concepts of hydrodynamics.

2.4 Basics of hydrodynamics

2.4.1 Relevant numbers and length scales

Fluids are usually described on the continuum level. However, the fluid itself consists of molecules and atoms. Here we briefly consider the typical effects that determine dynamics on the micro-, meso- and macroscale. Here we follow Ref. [69].

We first consider the hierarchy of length scales which are intrinsic to a fluid. The smallest dimension is that of an atom or a molecule l_a (see Fig. 2.2). The typical distance traveled between two collisions of the molecules is the mean free path l_{mfp}. To derive macroscopic quantities such as density ρ or temperature T, we need to average over many molecules. These quantities can vary locally over some distance l, which leads to macroscopic gradients. Finally, a fluid is usually confined by some boundaries which determines the overall system size l_S. Typically, one has $l_a \ll l_{\mathrm{mfp}} \ll l \leq l_S$.

The relation of the mean free path l_{mfp} to the characteristic length scale l is characterized by the Knudsen number

$$\mathsf{Kn} = \frac{l_{\mathrm{mfp}}}{l} \, . \tag{2.3}$$

The Knudsen number is a good indication for the appropriate simulation method. The mesoscopic kinetic theory belongs in the regime where $\mathsf{Kn} \lesssim 1$. A necessary criterion for the continuum picture is $\mathsf{Kn} \ll 1$. In Sec. 3.3.4 we will use the Knudsen number as an expansion parameter to prove that our simulation method can indeed be used to solve the hydrodynamic equations.

Coupled to this hierarchy of length scales is a hierarchy of time scales. In the atomic picture the time of a collision $t_c = l_a/v_T$ is determined by the average thermal velocity $v_T = (k_B T/m)^{1/2}$. It is interesting to note that the thermal velocity v_T is much larger than the macroscopic velocity u of the continuum (v_T is around the same order as the speed of sound c_s [70]). The time between collisions is $t_{\mathrm{mfp}} = l_{\mathrm{mfp}}/v_T$. This is the governing time scale of the kinetic theory, *i.e.* the molecular details are neglected. On this time scale the microscopic system relaxes toward its local equilibrium. The local equilibrium does not necessarily imply that the whole system is in equilibrium. Rather, the local equilibrium assumption allows the derivation of local thermodynamic quantities such as pressure, temperature or internal energy. When the system as a whole is out of equilibrium, which is usually the case, the existing gradients are smoothed out by two effects: advection (inertial regime) and diffusion (viscous regime). The corresponding time scales are $t_{\mathrm{adv}} \sim l/u$ and $t_{\mathrm{diff}} \sim l^2/\nu$. To determine which effect is dominant we form the ratio of the two timescales which yields the Reynolds number:

$$\mathsf{Re} = \frac{lu}{\nu} = \frac{t_{\mathrm{diff}}}{t_{\mathrm{adv}}} \, . \tag{2.4}$$

Yet another important time scale is given by the speed of sound in the fluid c_s. The time $t_{\mathrm{s}} \sim l/c_s$ describes how fast compression waves travel through the system. For an incompressible fluid this time scale has to be small compared to the advective time scale. Their ratio is characterized by the Mach number [71]

$$\mathsf{Ma} = \frac{u}{c_s} = \frac{t_{\mathrm{s}}}{t_{\mathrm{adv}}} \, . \tag{2.5}$$

As the speed of sound in water ($c_s = 1483 \, \mathrm{m/s}$ at $20 \, \mathrm{°C}$ [72]) is much larger than the typical flow speed in microfluidic devices ($u \sim 1 \, \mathrm{m/s}$), the Mach number is $\mathsf{Ma} \approx 1 \cdot 10^{-3}$. Thus, we can neglect compressibility in the analytical description of the fluid. However,
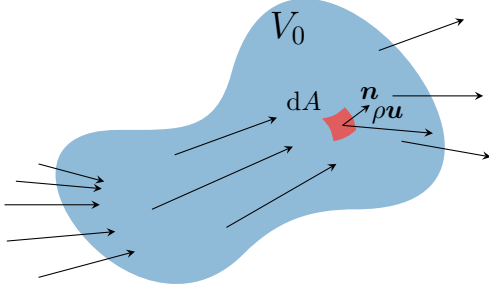
Figure 2.3: The mass inside an enclosed volume can only change by the mass current $\rho\boldsymbol{u}$ through the surface. Figure based on Ref. [73].

our simulation method, the lattice-Boltzmann method, is known for its relatively small speed of sound. We discuss the resulting implications in Ch. 3.

In the following we focus on the continuum picture to derive the relevant hydrodynamic equations for this work. In the continuum picture the movement and collisions of the fluid molecules is averaged out, and we assume that the fluid is locally in thermodynamic equilibrium. We derive the relevant equation for the fluid by using the conservation of mass and momentum, where we follow Ref. [69] and Ref. [73].

2.4.2 Conservation of mass

Let us consider a small fluid element with density ρ, which occupies some stationary volume V_0. The mass of this fluid element is simply $\int_{V_0} \rho \, dV$. The fluid mass is conserved, so any change needs to be transported through the boundary of the volume ∂V_0 (Fig. 2.3):

$$\partial_t \int_{V_0} \rho \, dV = - \oint_{\partial V_0} \rho\boldsymbol{u} \cdot \boldsymbol{n} \, dA \,, \tag{2.6}$$

where the mass moves with the fluid velocity $\boldsymbol{u}$ and $\boldsymbol{n} \, dA$ is the outwards directed surface element. We transform this equation using the Gauss theorem,

$$\int_{V_0} \partial_t \rho \, dV = - \int_{V_0} \nabla \cdot (\rho\boldsymbol{u}) \, dV \,. \tag{2.7}$$

As the volume V_0 is arbitrary and stationary, the integrands on both sides have to be the same and the continuity equation for fluid mass results,

$$\partial_t \rho + \nabla \cdot (\rho\boldsymbol{u}) = 0 \,. \tag{2.8}$$

For most applications we can assume that the density of the fluid is constant and does not change in time or space. Thus, the continuity equation of an incompressible fluid simplifies to

$$\nabla \cdot \boldsymbol{u} = 0. \qquad (2.9)$$

2.4.3 Conservation of momentum

Similar to the density, the momentum of a small fluid volume is changed by convection. Additionally, forces change the momentum by acting on the surface ∂V_0 or as a body force density $\boldsymbol{F}$ on the whole volume V_0.

Before we consider the change of momentum, we first need to introduce the general form of a surface force density:

$$\boldsymbol{T} = \boldsymbol{\sigma}\boldsymbol{n} = (-p\,\mathbb{1} + \boldsymbol{\sigma}')\boldsymbol{n}, \qquad (2.10)$$

where $\boldsymbol{\sigma}$ is the Cauchy stress tensor and $\boldsymbol{n}$ is the normal vector of the surface ∂V_0. Typically, one splits the Cauchy stress tensor into an isotropic pressure component $-p\,\mathbb{1}$ and a viscous stress component $\boldsymbol{\sigma}'$.

Considering all contributions, the change of momentum can be written as

$$\frac{\partial}{\partial t}\int_{V_0} \rho\boldsymbol{u}\,\mathrm{d}v = -\underbrace{\oint_{\partial V_0}(\rho\boldsymbol{u}\otimes\boldsymbol{u})\,\boldsymbol{n}\,\mathrm{d}A}_{\text{convection}} - \underbrace{\oint_{\partial V_0} p\boldsymbol{n}\,\mathrm{d}A + \oint_{\partial V_0}\boldsymbol{\sigma}'\boldsymbol{n}\,\mathrm{d}A}_{\text{surface force}} + \underbrace{\int_{V_0}\boldsymbol{F}\,\mathrm{d}V}_{\text{volume force}}. \qquad (2.11)$$

We use $(\boldsymbol{u}\otimes\boldsymbol{u})_{ij} = u_i u_j$ to denote the dyadic vector product.

Using the Gauss theorem and assuming that the volume is arbitrary yields

$$\partial_t(\rho\boldsymbol{u}) + \nabla\cdot(\rho\boldsymbol{u}\otimes\boldsymbol{u}) = -\nabla p + \nabla\cdot\boldsymbol{\sigma}' + \boldsymbol{F} \qquad (2.12)$$

or in components,

$$\partial_t(\rho u_i) + \partial_j\cdot(\rho u_i u_j) = -\partial_i p + \partial_j \sigma'_{ij} + F_i. \qquad (2.13)$$

Here we define $\partial_j = \partial_{x_j}$ and use the Einstein notation to sum over identical indices.

We are still missing the exact form of the viscous stress tensor $\boldsymbol{\sigma}'$. The viscous stress tensor $\boldsymbol{\sigma}'$ quantifies the internal friction between fluid layers moving with different velocities. The tensor thus depends on the spatial derivative of the velocity. We assume that the changes of the velocity within the fluid are small, so we only consider first-order derivatives. The viscous stress tensor has to vanish for a resting fluid regardless of the reference frame. By considering a resting fluid in a rotating frame of reference one can show that $\boldsymbol{\sigma}'$ cannot depend on asymmetric combinations of the derivatives [71]. The most general tensor of rank two, which satisfies all these conditions, is

$$\boldsymbol{\sigma}' = \eta\left(\nabla\boldsymbol{u} + (\nabla\boldsymbol{u})^T)\right) + \left(\zeta - \frac{2}{3}\eta\right)(\nabla\cdot\boldsymbol{u})\,\mathbb{1}, \qquad (2.14)$$
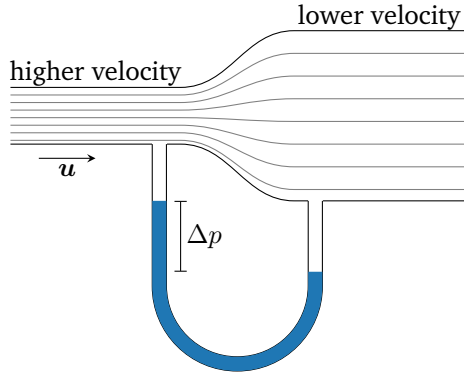
Figure 2.4: Air flow through a Venturi pipe. Due to conservation of mass the flow velocity in the narrower region needs to be higher which leads to a lower pressure. The pressure difference is indicated by the difference in the water levels on the left and right.

where the dynamic viscosity η characterizes the shear stress and the volume viscosity ζ describes the dilatational viscous stress.

For this work we assume that the fluid is incompressible ($\nabla \cdot \boldsymbol{u} = 0$) and that we deal with a Newtonian fluid, where the viscosity is constant. This yields the Navier-Stokes equations

$$\rho\left(\partial_t \boldsymbol{u} + (\boldsymbol{u} \cdot \nabla)\boldsymbol{u}\right) = -\nabla p + \eta \nabla^2 \boldsymbol{u} + \boldsymbol{F}\,. \tag{2.15}$$

2.4.4 Bernoulli's principle

Concerning the conservation of energy we only discuss one of its consequences: the Bernoulli's principle. It introduces the concept of dynamic pressure which allows a heuristic approach to the Segré-Silberberg effect (*cf.* Sec. 2.5.5). The Bernoulli's principle follows from the conservation of energy along a single streamline of the fluid:

$$\frac{1}{2}u^2 + \frac{p}{\rho} + \Psi = \text{const}\,, \tag{2.16}$$

where Ψ denotes a potential energy for example the gravitational potential. The relation is strictly true only for an ideal fluid without internal friction ($\nu = 0$). For a real fluid a small rate of energy dissipation needs to be considered which reduces the dynamic pressure.

Based on Eq. (2.16) we find, that an increase of the kinetic energy of a fluid leads to a reduced pressure. This effect can be nicely demonstrated in a Venturi meter where air is pumped through a constriction (Fig. 2.4). On the left the air flows through a narrow pipe which then rapidly extends to a larger radius. Due to the expansion of the pipe the flow velocity decreases in order to transport the same mass as at the inlet. The decreased flow velocity increases the pressure which can be observed by the different water levels in the connected U-shaped pipe. While Eq. (2.16) is only valid along an individual streamline, the concept of dynamic pressure gives an intuitive explanation to describe the different migration mechanisms of inertial migration (*cf.* Sec. 2.5.5).

2.4.5 Concept of similarity

One important property of fluid flows is the concept of similarity: Two flows behave the same, when the relevant dimensionless numbers are the same. The physics of the Segré-

Silberberg effect is the same whether the experiment is performed in a 1 cm thick pipe or in a microchannel only slightly thicker than a hair as long as the fluid properties are adjusted to obtain the same Reynolds number. As we have already seen in Sec. 2.4.1, the Reynolds number can be expressed as the ratio of advective and diffusive time scales [Eq. (2.4)]. It can also be derived by non-dimensionlizing the Navier-Stokes equation. For each quantity x we introduce a unit-less form by using the characteristic scale X,

$$x = X\tilde{x}. \tag{2.17}$$

There is some freedom in the choice of characteristic scaling factors. For the length L in a channel geometry one can either use the channel width $2w$, the channel height $2h$ or the hydrodynamic diameter $D = (2wh)/(w + h)$. For the velocity U one could either use the average velocity of the channel flow or its maximum velocity in the channel center. We base our definition on the maximum flow velocity $u_{\max}$ and the channel width $2w$. The characteristic timescale T is either given by L/U or, if the system is driven periodically, it is defined by the external driving. Applying Eq. (2.17) on the Navier-Stokes equations Eq. (2.15) yields

$$\rho \frac{U^2}{L} \left(\frac{L}{TU} \tilde{\partial}_t \tilde{u}_i + (\tilde{u}_j \tilde{\partial}_j) \tilde{u}_i \right) = -\frac{\eta U}{L^2} \tilde{\partial}_i \tilde{p} + \frac{\eta U}{L^2} \tilde{\partial}_j \tilde{\partial}_j \tilde{u}_i + \frac{\eta U}{L^2} \tilde{F}_i, \tag{2.18}$$

where $\tilde{\partial}_j = L\partial_j$. Furthermore, in Eq. (2.18) we rescale the pressure by $\eta U/L$ and the external force density by $\eta U/L^2$ [73].

Collecting all characteristic scaling factors we end up with

$$\mathsf{Re} \left(\frac{1}{\mathsf{St}} \tilde{\partial}_t \tilde{u}_i + (\tilde{u}_j \tilde{\partial}_j) \tilde{u}_i \right) = -\tilde{\partial}_i \tilde{p} + \tilde{\partial}_j \tilde{\partial}_j \tilde{u}_i + \tilde{F}_i \tag{2.19}$$

where we identify two non-dimensional numbers: the Reynolds number $\mathsf{Re} = \frac{\rho U L}{\eta}$ and the Strouhal number $\mathsf{St} = \frac{TU}{L}$.

The Strouhal number is only important when the system is driven periodically. In such cases, the Strouhal number relates the external timescale T to the time given by the characteristic length L and velocity U [74]. In this work we use no periodic force to drive the channel flow, thus $\mathsf{St} = 1$.

In this work we use three different forms of the Reynolds number. As we are in general interested in channel flows, the most common form is the channel Reynolds number Re which is defined by the maximum flow velocity $u_{\max}$ and the full channel width $2w$

$$\mathsf{Re} = \frac{2\rho w u_{\max}}{\eta}. \tag{2.20}$$

In the further course of this chapter we consider the friction on a particle which moves relatively to a fluid. In this case the bulk Reynolds number $\mathsf{Re}_p^{\mathrm{bulk}}$ is given by the relative velocity between particle and fluid u_r, and the particle radius a

$$\mathsf{Re}_p^{\mathrm{bulk}} = \frac{2a\rho u_r}{\eta}. \tag{2.21}$$
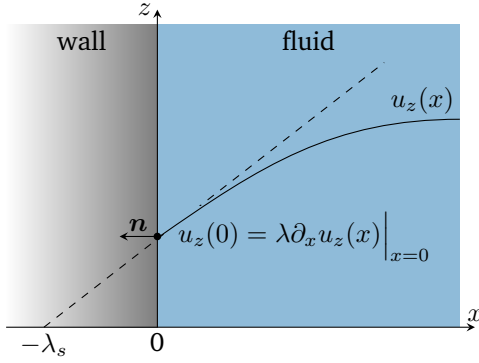
Figure 2.5: The Navier boundary condition with the slip length λ_s. The slip length λ_s corresponds to the distance behind the surface where the linear extrapolation of the velocity is zero. The figure is based on Ref. [73].

The third form of the Reynolds number is the shear particle Reynolds number Re_p, which is given by the change in velocity over a particle in a shear flow with shear rate $\dot{\gamma}$. The change in velocity is then given by $\Delta u = a\dot{\gamma}$. For a parabolic flow profile in a channel flow the mean shear rate is $\dot{\gamma} = u_{\max}/w$. This yields

$$\text{Re}_p = \frac{2a\rho\Delta u}{\eta} = \frac{2\rho u_{\max}a^2}{w\eta} = \text{Re}\left(\frac{a}{w}\right)^2. \tag{2.22}$$

We note that this quantity is based on the mean shear rate. Alternatively, one can also consider a local particle Reynolds number which depends on the particles position.

When the Reynolds number in Eq. (2.19) is low and viscous damping is dominant we can further simplify the Navier-Stokes equations. Neglecting the left side of Eq. (2.19) we get the Stokes equations:

$$\nabla p = \eta\nabla^2\boldsymbol{u} + \boldsymbol{F}. \tag{2.23}$$

In contrast to the full Navier-Stokes equations, these equations are linear partial differential equations and independent of time. Hence, the solutions are unique and allow linear combinations. This simplifies an analytical treatment and allows, at least some, analytical solutions of hydrodynamic problems.

Gases or ideal fluids on the other hand have almost no internal friction and thus vanishing viscosity ($\eta = 0$). In this case the Navier-Stokes equations simplify to the Euler equations

$$\rho\left(\partial_t\boldsymbol{u} + (\boldsymbol{u}\cdot\nabla)\boldsymbol{u}\right) = -\nabla p + \boldsymbol{F}. \tag{2.24}$$

Inertial microfluidics occupy the intermediate regime, where fluid inertia is relevant but the flow field is still laminar. Hence, we need the full Navier-Stokes equations.

2.4.6 Boundary conditions

To determine the solution of the Navier-Stokes equations, we need to define the velocity field on all boundaries. At the interface between the fluid and the solid walls the velocity normal to the boundary has to vanish, as otherwise the fluid would penetrate the boundary,

$$\boldsymbol{u}_\perp = (\boldsymbol{n}\cdot\boldsymbol{u})\boldsymbol{n} = \boldsymbol{0}, \tag{2.25}$$
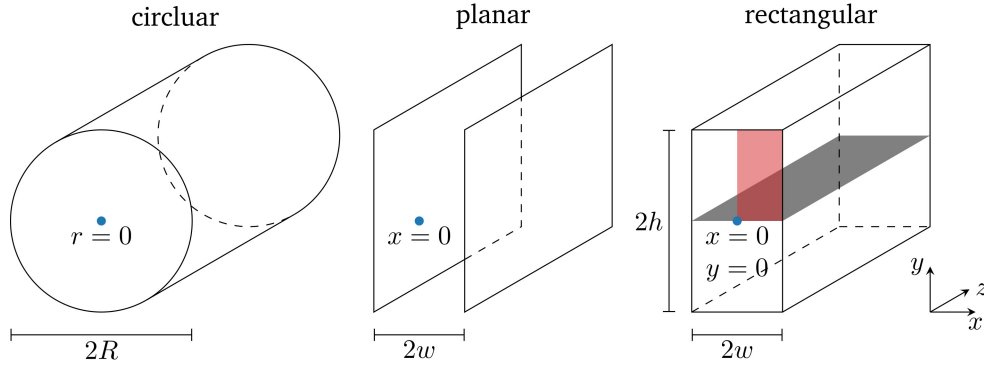
Figure 2.6: Sketch of different channel geometries. The blue dots indicate the center of the coordinate system. If not otherwise stated, we initialize our particles in the x-z-plane in a rectangular channel (gray plane). In chapter 4 and 6 we calculate the lift force profiles, where we only consider the first quadrant (red area). The quantities in the other quadrant can be obtained by symmetry operations.

where $\boldsymbol{n}$ is the outward pointing normal vector. For the tangential component the requirements are not that rigorous. Typical for solid-fluid interfaces is the no-slip boundary condition. For the no-slip boundary condition one assumes that the fluid moves exactly with the velocity of the boundary $\boldsymbol{v}_{\mathrm{wall}}$, which is typically $\boldsymbol{v} = 0$ [75],

$$\boldsymbol{u}\Big|_{\mathrm{wall}} = \boldsymbol{v}_{\mathrm{wall}} \, . \tag{2.26}$$

While the no-slip boundary condition holds for most liquids and boundaries, and certainly all applications in this work, we want to discuss the limits of this condition. At the molecular level the molecules surely slip over the interface. Therefore, from a microscopic view the no-slip boundary condition is questionable. In the 19th century, Navier already introduced a more general condition that is named after him [73],

$$\boldsymbol{u}_{\parallel}\Big|_{\mathrm{wall}} = -\lambda_s (\boldsymbol{n} \cdot \nabla) \boldsymbol{u}_{\parallel}\Big|_{\mathrm{wall}} \, . \tag{2.27}$$

Here some slip velocity over the surface is allowed and the slip or Navier length λ_s is introduced (Fig. 2.5). The slip length λ_s defines the distance behind the wall where the extrapolated velocity is zero. In careful experiments Joseph and Tabeling measured the slip length for water on glass to be $\lambda_s = (50 \pm 50)\,\mathrm{nm}$ [76]. However, for some hydrophobic coatings slip lengths in the order of $1\,\mu\mathrm{m}$ where found [77]. If such surfaces were used in microfluidic systems, they would have a pronounced influence by virtually increasing the channel width.

2.4.7 Poiseuille flow

With the fluid equations and the boundary condition we are equipped to calculate the flow profile which develops in a pressure driven channel flow. Fortunately this flow field can be determined analytically for almost any cross section as long as it is constant along
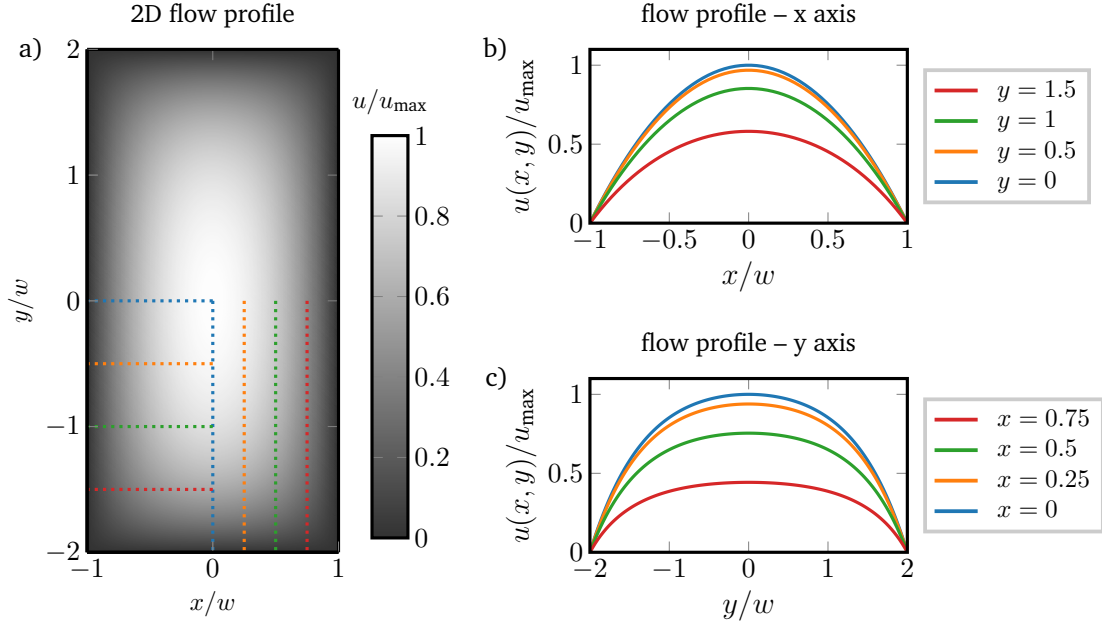
Figure 2.7: Poiseuille flow profile $u(x,y)$ in a channel with aspect ratio $w/h = 0.5$. **(a)** shows the profile in the plane perpendicular to the flow direction. The colored lines indicate the position of the flow profiles along the x-axis **(b)** and the y-axis **(c)**. While the profile along the x-axis always has a parabolic shape, the profile along the y-axis flattens significantly toward the center of the channel.

the flow direction [73]. In this case the flow is parallel to the channel axis and changes only perpendicular to its direction. Thus, the advection term $(\boldsymbol{u} \cdot \nabla)\boldsymbol{u}$ in the Navier-Stokes equations Eq. (2.15) vanishes. Furthermore, we are interested in the steady-state solution $(\partial_t \boldsymbol{u} = 0)$.

Here we consider a channel of length L with a rectangular cross section (width $2w$, height $2h$) where the flow is driven by a pressure gradient $\nabla p = -\Delta p / L \hat{e}_z$. The origin of the coordinate system is located at the center of the channel cross section with the flow in z-direction. We refer to the plane perpendicular to that axis as lateral plane. The x-axis points along the short channel axis (Fig. 2.6).

Based on our definitions we can write the flow as $\boldsymbol{u} = u(x,y)\hat{e}_z$. The Navier-Stokes equation for this problem is given by

$$\frac{\Delta p}{L} = \eta \left(\partial_x^2 + \partial_y^2 \right) u_z(x,y).$$ (2.28)

At the solid walls the flow field has to fulfill the no-slip boundary condition $\boldsymbol{u}|_{\text{wall}} = \boldsymbol{0}$. This yields the solution [73]

$$u_z(x,y) = \frac{16w^2 \Delta p}{\pi^3 \eta L} \sum_{n,\text{odd}}^{\infty} \frac{1}{n^3} \left[1 - \frac{\cosh\left(n\pi \frac{y}{2w}\right)}{\cosh\left(n\pi \frac{h}{2w}\right)} \right] \sin\left(\frac{n\pi}{2} \left(\frac{x}{w} + 1 \right) \right).$$ (2.29)

The solution Eq. (2.29) is plotted in Fig. 2.7. Along the short axis (x-axis) the flow has an almost parabolic shape, while along the long axis the profile flattens toward the center line, resulting in low shear rates in the center of the channel and high shear rates near the walls.

The flow field for the other two geometries shown in Fig. 2.6 has a much simpler parabolic form. The flow profile between two infinite walls placed at $x = \pm w$ follows

$$u_z(x) = \frac{\Delta p}{2\eta L} \left(w^2 - x^2 \right) ,\tag{2.30}$$

and the flow through a cylindrical channel with radius R is given by

$$u_z(r) = \frac{\Delta p}{4\eta L} \left(R^2 - r^2 \right) .\tag{2.31}$$

While the flow field of a rectangular channel has a much more complicated form, the parabolic approximation is often sufficient to get the correct flow profile along the short axis.

2.5 Rigid particles in flow

We have now established the fundamentals for the description of fluids. In the following we examine the interactions of particles and fluids. First, we discuss the drag force and the disturbance flow created by a particle in the regime of vanishing Reynolds numbers. We show that the cross-streamline migration of the Segré-Silberberg effect is not compatible with the Stokes equations and can only be explained by inertial effects. We then review the different mechanisms proposed for inertial migration. Finally, we present a model that explains how particles in channels with non-circular cross section reach their equilibrium positions. In this section, we focus on solid, spherical particles while we discuss the modeling of deformable capsules and the deformability-induced lift force in the next section.

2.5.1 Basic physics

The dynamics of a rigid particle is fully described by its position $\boldsymbol{x}$, its velocity $\boldsymbol{v}$ and its angular velocity $\boldsymbol{\Omega}$. In this work we focus on particles with the same density ρ as the surrounding fluid (neutrally buoyant particles). Since the typical particle size is in the order of 5 to $10\,\mu$m (*cf.* Tab. 2.1), thermal fluctuations do not play a role and the dynamics of a particle is given by Newton's equations of motion [78]:

$$\frac{\mathrm{d}}{\mathrm{d}t}\boldsymbol{x} = \boldsymbol{v} ,\tag{2.32a}$$

$$M\frac{\mathrm{d}}{\mathrm{d}t}\boldsymbol{v} = \boldsymbol{f}_{\text{fluid}} + \boldsymbol{f}_{\text{ext}} ,\tag{2.32b}$$

$$\boldsymbol{I}\frac{\mathrm{d}}{\mathrm{d}t}\boldsymbol{\Omega} = \boldsymbol{T}_{\text{fluid}} + \boldsymbol{T}_{\text{ext}} ,\tag{2.32c}$$

where M is the mass of the particle and $\boldsymbol{I}$ is its moment of inertia. The force $\boldsymbol{f}$ and torque $\boldsymbol{T}$ are split into a contribution of the fluid and a contribution of external forces. The external forces can result from electric or magnetic fields. We will later use such external forces to control the position of a deformable particle (Sec. 6.5).

The force and the torque the fluid exerts on the particle is given by [75]

$$\boldsymbol{f}_{\text{fluid}} = \oint_{\text{particle}} (-p\,\mathbb{1} + \boldsymbol{\sigma}') \cdot \boldsymbol{n}\,\mathrm{d}A\,, \tag{2.33}$$

$$\boldsymbol{T}_{\text{fluid}} = \oint_{\text{particle}} \boldsymbol{x} \times \left((-p\,\mathbb{1} + \boldsymbol{\sigma}') \cdot \boldsymbol{n} \right)\,\mathrm{d}A\,. \tag{2.34}$$

Here $\boldsymbol{\sigma}'$ denotes the viscous stress tensor which we introduced in Sec. 2.4.3. The equations (2.33) and (2.34) are very general and are typically used in simulations and analytical calculations. The difficulty is to determine the pressure and viscous stress tensor on the surface of the particle. We separate f_{fluid} into two components: the drag force f_{drag} and the lift force f_{lift}. The drag force acts in the direction of the flow velocity, while the lift force is perpendicular to it.

In the following we concentrate on the simplest geometry, a rigid sphere. For a rigid sphere the two equations (2.33) and (2.34) can be further simplified resulting in the Stokes drag, which we discuss in the next section.

2.5.2 The Stokes drag and its corrections

One of the most fundamental problems o hydrodynamics is the drag force acting on a sphere when it moves relative to the surrounding fluid. We first discuss the case where a particle moves through a uniform velocity field. Then, we review the following corrections to the drag force: the corrections due to inertial effects, the influence of walls, and, the correction on the drag force due to an inhomogeneous flow. It is important to note that while there is an analytical description for each effect individually, such a solution cannot be found for the combination of all effects. We concentrate on a sphere with radius a, which moves with a velocity $\boldsymbol{v}$ and rotates with an angular velocity $\boldsymbol{\Omega}$. The flow field is described by $\boldsymbol{u}$.

When the particle moves through bulk fluid in a uniform flow field with a different velocity than the fluid, it disturbs the fluid which results in a drag force. In this case Eq. (2.33) can be solved and result in a simpler equation for the drag force [75]

$$\boldsymbol{f}_{\text{drag}} = 6\pi\eta a(\boldsymbol{u} - \boldsymbol{v}) = \xi(\boldsymbol{u} - \boldsymbol{v})\,, \tag{2.35}$$

where η is the viscosity of the fluid and ξ is called drag coefficient. This force is also called Stokes drag in honor of George Gabriel Stokes, who first derived this formula [79].

Similarly, one can derive the torque [*cf.* Eq. (2.34)] acting on the particle when the particle is immersed in a rotating flow field [75],

$$\boldsymbol{T}_{\text{drag}} = 8\pi\eta a^3(\boldsymbol{\omega} - \boldsymbol{\Omega}) = \xi_r(\boldsymbol{\omega} - \boldsymbol{\Omega})\,, \tag{2.36}$$

where $\boldsymbol{\omega} = \nabla \times \boldsymbol{u}$ is the vorticity of the fluid and ξ_r is the rotational drag coefficient. As these formulas for the drag are derived based on the Stokes equation they are only valid for vanishing Reynolds numbers.

In 1911 Oseen extended the formalism and calculated the first order correction term for the influence of the fluid inertia on the drag coefficient [80]. Following his work we consider the full Navier-Stokes equations Eq. (2.15) and analyze the system in the reference frame of the particle. We begin by splitting the flow velocity $\boldsymbol{u}$ into two parts: the uniform, undisturbed flow field $\boldsymbol{u}_0$ and a disturbance flow field $\boldsymbol{u}'$ induced by the particle. The exact form of the disturbance flow is discussed the next section. The advective term in the Navier-Stokes equations is then written as

$$(\boldsymbol{u} \cdot \nabla)\,\boldsymbol{u} = (\boldsymbol{u}_0 \cdot \nabla)\,\boldsymbol{u}_0 + (\boldsymbol{u}_0 \cdot \nabla)\,\boldsymbol{u}' + \left(\boldsymbol{u}' \cdot \nabla\right)\boldsymbol{u}_0 + \left(\boldsymbol{u}' \cdot \nabla\right)\boldsymbol{u}'. \tag{2.37}$$

This term simplifies as the derivative of the uniform field vanishes, and we can neglect $\mathcal{O}(u'^2)$. This yields the Oseen equations for a uniform flow

$$\rho \left(\partial_t \boldsymbol{u}' + (\boldsymbol{u}_0 \cdot \nabla)\,(\boldsymbol{u}')\right) = -\nabla p + \eta \nabla^2 \boldsymbol{u}'. \tag{2.38}$$

As we are only interested in the steady state, we ignore the time derivative. Using these equations the drag on a particle can be solved analytically and yields a correction to the Stokes drag [73]

$$\boldsymbol{f}_{\text{drag}} = 6\pi\eta a \boldsymbol{u} \left(1 + \frac{3}{8}\frac{|\boldsymbol{u}|a}{\nu}\right) = \xi_{\text{Stokes}} \boldsymbol{u} \left(1 + \frac{3}{8}\text{Re}_p^{\text{bulk}}\right) \tag{2.39}$$

where $\text{Re}_p^{\text{bulk}} = |\boldsymbol{u}|a/\nu$ is the bulk particle Reynolds number [*cf.* Eq. (2.21)].

Next we consider the changes when the particle does not move through bulk but close to solid boundaries. Now we again neglect inertial effects. In the following we assume that the fluid is at rest and the particle moves. The particle causes a disturbance flow which still needs to fulfill the no-slip boundary condition at the walls. This leads to an increased friction near the walls as the disturbance flow has to approach the no-slip boundary velocity at a shorter distance. In case of a Stokes flow and small particle sizes this problem can be solved analytically using the method of mirror images [81]. Similar to the method of mirror charges in electrodynamics one places a virtual particle on the opposite side of the boundary and successively solves the no-slip condition on the boundary at the wall and the particle. The drag the particle experiences depends on the direction of its motion relative to the wall [81],

$$\boldsymbol{f}_{\text{drag}} = -\xi_{\text{Stokes}} \left(1 + \frac{9}{8}\frac{a}{d}\right)\boldsymbol{v}_\perp - \xi_{\text{Stokes}} \left(1 + \frac{9}{16}\frac{a}{d}\right)\boldsymbol{v}_\| + \mathcal{O}\left((a/d)^2\right), \tag{2.40}$$

where d is the distance of the center of the particle to the wall and $\boldsymbol{v}_\perp$ and $\boldsymbol{v}_\|$ describe the velocity components perpendicular and parallel to the wall, respectively.

The last correction we want to consider is the effect of an inhomogenous flow. As the flow through a channel leads to an inhomogeneous flow profile, this case is particularly relevant for this work (*cf.* Sec. 2.4.7). Additionally to the relative velocity between the particle and the flow, the change of the flow profile in the vicinity of the particle has to be considered. Faxén calculated the force and the torque on a particle for a Poiseuille flow assuming negligible wall effects [75, 82],

$$\boldsymbol{f}_{\text{drag}} = 6\pi\eta a \left(1 + \frac{a^2}{6}\nabla^2\right)\boldsymbol{u}_0(\boldsymbol{x}_c) - 6\pi\eta a \boldsymbol{v}\,, \tag{2.41}$$

$$\boldsymbol{T}_{\text{drag}} = 8\pi\eta a^3(\boldsymbol{\omega} - \boldsymbol{\Omega})\,, \tag{2.42}$$

where $\boldsymbol{x}_c$ is the position of the center of the particle. While this formula was derived for the Poiseuille flow, it is valid for arbitrary flow profiles. The torque on the particle is not altered compared to Eq. (2.36). The force, however, gets an additional contribution $\propto a^2\nabla^2\boldsymbol{u}_0$, which results in a correction for the drag coefficient. When a particle follows the flow without external force, the drag force vanishes and the particle's velocity is given by

$$\boldsymbol{v} = \left(1 + \frac{a^2}{6}\nabla^2\right)\boldsymbol{u}_0(\boldsymbol{x}_c)\,. \tag{2.43}$$

2.5.3 Multipole expansion of the disturbance flow

Up to now we discussed the force the fluid exerts on the particle. While we already considered the disturbance flow $\boldsymbol{u}'$ created by a particle, we have not introduced the exact form of $\boldsymbol{u}'$. Since the Stokes equation is a linear differential equation, the superposition principle applies, and we can use the method of Green's function [83]. To calculate the disturbance flow caused by a particle at the position $\boldsymbol{x}$ we consider a point force $\boldsymbol{f}(\boldsymbol{0}) = \boldsymbol{f}_0\delta(\boldsymbol{0})$ in Eq. (2.23) which acts on the fluid, where $\delta(\boldsymbol{0})$ is the delta function.

Such a point force creates a disturbance flow field $\boldsymbol{u}'$ given by [75]

$$\boldsymbol{u}'(\boldsymbol{x}) = \boldsymbol{G}(\boldsymbol{x})\boldsymbol{f}_0\,, \tag{2.44}$$

where $\boldsymbol{G}$ is the Oseen tensor

$$\boldsymbol{G}(\boldsymbol{x}) = \frac{1}{8\pi\eta|\boldsymbol{x}|}\left(\frac{\boldsymbol{x}\otimes\boldsymbol{x}}{|\boldsymbol{x}|^2} + \mathbb{1}\right)\,. \tag{2.45}$$

The disturbance flow field scales with $1/x$ and is called Stokeslet. This solution is exact for a point force. However, we are interested in particles with a finite radius. Therefore, we need to consider all forces acting on the surface and use the Green's formalism. Since we can write any force density as the sum of delta functions, the solution for an arbitrary surface force density $\boldsymbol{\zeta}\boldsymbol{n}$ acting on the particle is given by the superposition convolution

$$\boldsymbol{u}'(\boldsymbol{x}) = -\oint_{\text{particle}} \left(\zeta(\boldsymbol{x}')\boldsymbol{n}\cdot\boldsymbol{G}(\boldsymbol{x}-\boldsymbol{x}')\right)\mathrm{d}A'\,, \tag{2.46}$$

where $\boldsymbol{n}$ is the normal vector of the particle surface.

Similar to the multipole expansion in electrodynamics, this disturbance flow can be expressed by moments at sufficiently large distances from the particle ($|\boldsymbol{x}| \gg |\boldsymbol{x}'|$). Far enough away from the particle one can no longer distinguish between a point on the surface $\boldsymbol{x}'$ and the center of the particle. Thus, we have $\boldsymbol{G}(\boldsymbol{x} - \boldsymbol{x}') \approx \boldsymbol{G}(\boldsymbol{x})$. Formally, we expand the Oseen tensor in Eq. (2.46) in $\boldsymbol{x}'$ about $\boldsymbol{x}' = \boldsymbol{0}$,

$$u'_i(\boldsymbol{x}) = -G_{ij}(\boldsymbol{x})F_j + G_{ijk}(\boldsymbol{x})D_{jk} + \dots , \tag{2.47}$$

with

$$\boldsymbol{F} = \oint_{\text{particle}} \boldsymbol{\zeta}(\boldsymbol{x}')\boldsymbol{n}\,\mathrm{d}A' , \tag{2.48}$$

$$\boldsymbol{D} = \oint_{\text{particle}} \left(\boldsymbol{\zeta}(\boldsymbol{x}')\boldsymbol{n}\right) \otimes \boldsymbol{x}'\,\mathrm{d}A' , \tag{2.49}$$

$$G_{ijk}(\boldsymbol{x}) = \frac{1}{8\pi\eta|\boldsymbol{x}|^3} \left(-\delta_{ij}x_k + \delta_{jk}x_i + \delta_{ik}x_j - \frac{3x_ix_jx_k}{|\boldsymbol{x}|^2} \right) . \tag{2.50}$$

The leading term in Eq. (2.47) is a Stokeslet with the coefficient $\boldsymbol{F}$ equal to the force exerted by the fluid on the particle. This term is only present when a net force acts on the particle. In analogy to the electrostatics $\boldsymbol{F}$ is also called force monopole. The next higher order is a force dipole $\boldsymbol{D}$, which can be split in a symmetric and an anti-symmetric part, called stresslet $\boldsymbol{S}$ and rotlet $\boldsymbol{T}$ [75],

$$\boldsymbol{D} - \frac{1}{3}\text{tr}(\boldsymbol{D})\,\mathbb{1} = \boldsymbol{S} + \boldsymbol{T} , \tag{2.51}$$

with $\text{tr}(\boldsymbol{D})$ is the trace of $\boldsymbol{D}$ and

$$\boldsymbol{S} = \frac{1}{2} \oint_{\text{particle}} \left[(\boldsymbol{\zeta}\boldsymbol{n}) \otimes \boldsymbol{x}' + \boldsymbol{x}' \otimes (\boldsymbol{\zeta}\boldsymbol{n}) \right]\,\mathrm{d}A' - \frac{\mathbb{1}}{3} \oint_{\text{particle}} (\boldsymbol{\zeta}\boldsymbol{n}) \cdot \boldsymbol{x}'\,\mathrm{d}A' , \tag{2.52}$$

$$\boldsymbol{T} = \frac{1}{2} \oint_{\text{particle}} \left[(\boldsymbol{\zeta}\boldsymbol{n}) \otimes \boldsymbol{x}' - \boldsymbol{x}' \otimes (\boldsymbol{\zeta}\boldsymbol{n}) \right]\,\mathrm{d}A' . \tag{2.53}$$

In the following we need the disturbance field of a particle in a linear shear flow. Such a particle is force-free ($\boldsymbol{F} = 0$) and components for the rotlet $\boldsymbol{T}$ cancel out each other. Thus, the disturbance flow for this case is given by

$$u'_i = \frac{3}{8\pi\eta} \frac{S_{ij}}{|\boldsymbol{x}|^5} x_i x_j x_l . \tag{2.54}$$

2.5.4 No lift force at zero Reynolds number

So far we mostly considered non-inertial fluid-particle interactions. As already mentioned in Sec. 2.3, the Segré-Silberberg effect requires the inertia of the fluid. This was proven
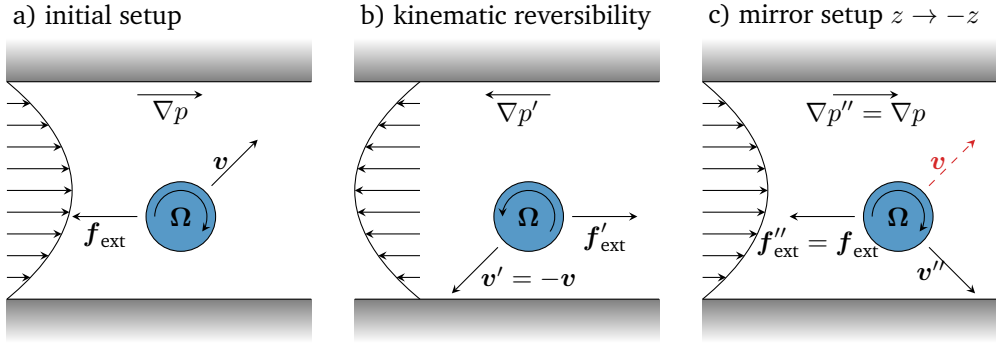
Figure 2.8: Graphical illustration of Bretherton's proof. **(a)** We consider a spherical particle immersed in a channel flow, which is driven by the pressure gradient ∇p. We allow for an external force $\boldsymbol{f}_{\text{ext}}$ to act on the particle. The particle moves with a velocity $\boldsymbol{v}$ which is a solution of the Stokes equation. For the sake of the argument we assume that this velocity has a nonzero lateral component. **(b)** The same system as (a) but with reversed pressure gradient $\nabla p'$ and external force $\boldsymbol{f}'_{\text{ext}}$. The kinematic reversibility then states that $\boldsymbol{v}' = -\boldsymbol{v}$. **(c)** The system is mirrored on the x-y-plane. This transforms the pressure gradient and the external force onto its original value. Thus, the system should be identical to the initial system (a). However, for the velocity only the component along the flow direction changes. This leads to a contradiction, which can only be solved if the lateral velocity component vanishes. Figure adapted from Ref. [84].

by Bretherton one year after the publication of the experiments. He based his arguments on the symmetry of the Stokes equations, showing that particles cannot move across streamlines at vanishing Reynolds numbers [85]. Here, we briefly discuss Bretherton's argument following his article Ref. [85].

Bretherton based his argument on the kinematic reversibility, a special property of the Stokes equation. It implies the following: Let $\boldsymbol{u}$ be a solution of the Stokes equations for a given pressure gradient ∇p and external force $\boldsymbol{f}_{\text{ext}}$ acting on the particle in flow direction. The kinematic reversibility implies that the solution of the Stokes equations with reversed pressure gradient $-\nabla p$ and reversed force $-\boldsymbol{f}_{\text{ext}}$ is given by $-\boldsymbol{u}$. An equivalent system with reversed force and pressure gradient can also be obtained by a reflection on the x-y-plane. As this system is driven by the same external force and pressure gradient, the resulting dynamics have to be identically given by $-\boldsymbol{u}$. This is only true for velocities perpendicular to the mirror plane, which rules out any cross-streamline migration.

In the following we will put these arguments on a mathematical foundation. We assume a flow through a straight channel with arbitrary cross section. The flow is driven by a pressure gradient ∇p which creates a flow profile $\boldsymbol{u} = u(x,y)\hat{e}_z$ in the z-direction [Fig. 2.8 (a)]. In this flow we place a rigid spherical particle which moves with velocity $\boldsymbol{v}$ and rotates with an angular velocity $\boldsymbol{\Omega}$. Furthermore, we allow an external force $\boldsymbol{f}_{\text{ext}}$ to act on the particle in the direction of the flow. We place the center of our coordinate system such that $z = 0$ coincides with the current particle position. Each vector can be split into a component along and perpendicular to the flow, which we call $\boldsymbol{v}_{\parallel}$ and $\boldsymbol{v}_{\perp}$ respectively.

For a given external field ∇p and $\boldsymbol{f}_{\text{ext}}$ the Stokes equation uniquely defines the velocities $\boldsymbol{u}$, $\boldsymbol{v}$ and $\boldsymbol{\Omega}$. First, we apply the kinematic reversibility on this system which corresponds to reversing the driving of the flow [Fig. 2.8 (b)]:

$$\nabla p' = -\nabla p \quad \text{and} \quad \boldsymbol{f}'_{\text{ext}} = -\boldsymbol{f}_{\text{ext}} \tag{2.55}$$

which results in the new velocities

$$\boldsymbol{u}'(\boldsymbol{x}) = -\boldsymbol{u}(\boldsymbol{x})\,, \tag{2.56a}$$
$$\boldsymbol{v}' = -\boldsymbol{v}\,, \tag{2.56b}$$
$$\boldsymbol{\Omega}' = -\boldsymbol{\Omega}. \tag{2.56c}$$

Next, we mirror the primed system along the x-y-plane. Thus, all components parallel to the flow direction reverse their sign while the perpendicular components remain unchanged [Fig. 2.8 (c)]

$$\boldsymbol{v}''_{\parallel} = -\boldsymbol{v}'_{\parallel}, \qquad \boldsymbol{v}''_{\perp} = \boldsymbol{v}'_{\perp}\,. \tag{2.57}$$

The angular velocity $\boldsymbol{\Omega}$ is a pseudo-vector, where the perpendicular component gains an additional sign change under reflection. Thereby, the cross product of $\boldsymbol{\Omega}$ with an arbitrary vector transforms as Eq. (2.57) [86],

$$\boldsymbol{\Omega}''_{\parallel} = \boldsymbol{\Omega}'_{\parallel}, \qquad \boldsymbol{\Omega}''_{\perp} = -\boldsymbol{\Omega}'_{\perp}\,. \tag{2.58}$$

The mirror operation also reverses the external driving into their original form

$$\nabla p'' = \nabla p \quad \text{and} \quad \boldsymbol{f}''_{\text{ext}} = \boldsymbol{f}_{\text{ext}}\,. \tag{2.59}$$

Thus, the initial setup and the transformed setup should behave exactly the same [Fig. 2.8 (a) and (c)]. However, we do not get the original values for the particle velocity $\boldsymbol{v}$

$$\boldsymbol{v}''_{\parallel} = \boldsymbol{v}_{\parallel}, \qquad \boldsymbol{v}''_{\perp} = -\boldsymbol{v}_{\perp} \tag{2.60}$$

nor the angular velocity

$$\boldsymbol{\Omega}''_{\parallel} = -\boldsymbol{\Omega}_{\parallel}, \qquad \boldsymbol{\Omega}''_{\perp} = \boldsymbol{\Omega}_{\perp}\,. \tag{2.61}$$

Since solutions of the Stokes equation are unique this implies

$$\boldsymbol{v}_{\perp} = 0, \qquad \boldsymbol{\Omega}_{\parallel} = 0 \tag{2.62}$$

and there cannot be a lateral migration within the Stokes flow. To explain the cross-streamline migration observed by Segré and Silberberg one needs to go beyond the description of the Stokes equation.

2.5.5 Theoretical understanding of inertial focusing

As we have seen, no cross-streamline migration is possible in the regime of vanishing Reynolds numbers. In the following section we discuss the four different effects that were
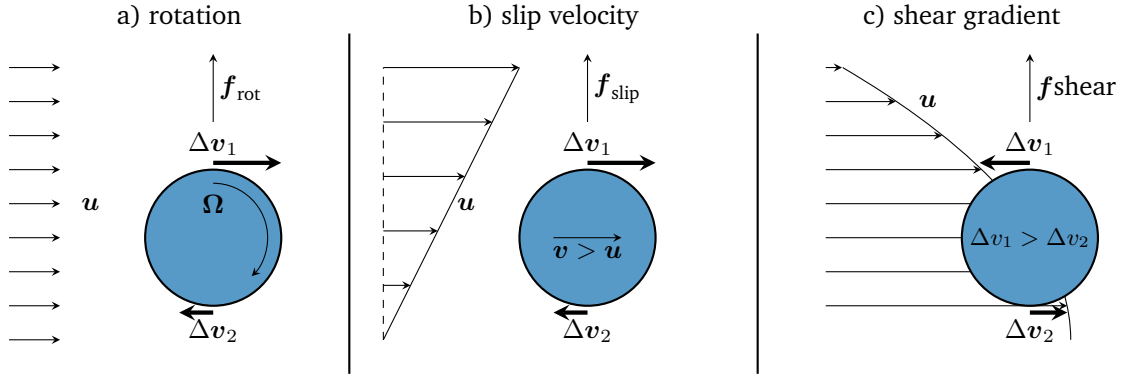
Figure 2.9: Illustration of different migration mechanisms in inertial microfluidics. Whether a rotating particle moves through a fluid **(a)**, is dragged through a linear shear flow **(b)** or moves in an inhomogeneous shear flow **(c)**, the particle always has a different velocity on its two sides perpendicular to the flow direction. Following Bernoulli's principle this lowers the pressure on the side where the velocity is higher and leads to an inertial lift force acting perpendicular to the flow direction.

proposed to explain the inertial focusing. All these migration effects require at least a small but finite Reynolds number.

The first two mechanisms could not explain the Segré-Silberberg effect. Nevertheless, we discuss them here, as they provide important insights for inertial microfluidics. The first effect becomes relevant in the next section, as it is used to explain the location of equilibrium points in rectangular channels. The second effect is the Saffman effect, which we will use in Sec. 6.5 to influence the equilibrium position of deformable capsules. Finally, we turn to the two effects that explain the formation of an annulus in the Segré-Silberberg experiment.

Rotation-induced migration – the Magnus effect   A first approach to explain the Segré-Silberberg effect was based on the idea of rotation-induced migration. Rubinow and Keller analyzed a rotating particle in a fluid with a homogeneous velocity field [5]. They considered the limit of small but non-zero Reynolds numbers using matched asymptotic calculations, which we explain in more detail in Sec. 2.5.7. Due to the rotation of the particle the relative velocity between the sphere and the fluid is larger on one side compared to the opposite side [Fig. 2.9 (a)]. Following Bernoulli's principle [*cf.* Eq. (2.16)], this leads to a lower dynamic pressure on the side where the velocity is higher. The resulting force is given by

$$\boldsymbol{f}_{\text{rot}} = \pi a^3 \rho \boldsymbol{\Omega} \times \boldsymbol{v}_r \,, \tag{2.63}$$

where a is the radius, $\boldsymbol{\Omega}$ is the angular velocity of the particle, and $\boldsymbol{v}_r$ is the relative velocity between the particle and the fluid [52].

To explain the Segré-Silberberg effect we need to consider channel flow. In this case the rotation-induced lift force points to the channel center [37]. Thus, this migration mechanism cannot explain the Segré-Silberberg effect. Furthermore, Saffman [6] later

calculated that the rotation-induced force is by an order of magnitude smaller than the lift force created by a shear gradient. Hence, this contribution is often neglected. However, as we will see in Sec. 2.5.6 Zhou and Papautsky proposed a model based on this force to explain the limited number of equilibrium positions in non-cylindrical channel geometries.

Slip-induced migration – the Saffman force   Saffman extended Rubinow's and Keller's calculation for a moving particle in an unbounded linear shear flow [6]. The important criterion for the slip-induced migration is that the particles moves relatively to the surrounding shear flow. If that is the case, it has a larger relative velocity on one side and a smaller one on the other side. As we have already seen with the rotation-induced migration the different relative velocities lead to a dynamic pressure difference and the particle moves into the direction of the larger velocity [Fig. 2.9 (b)]. This pressure difference results in a force

$$f_{\text{slip}} = \rho K a^2 \left(\dot{\gamma}\nu\right)^{-1/2} v_r \qquad (2.64)$$

where $K \sim 6.46$ is a numerical constant [6, 87], $\dot{\gamma}$ is the shear rate, ρ and ν are the density and kinematic viscosity of the fluid and v_r is the relative velocity between the particle and the fluid. In honor of Saffman this force is called Saffman force. In contrast to the results of Rubinow and Keller, this force is independent of the rotation of the particle. Although, the Saffman force is an order of magnitude larger than the rotation-induced lift force, it still cannot explain the Segré-Silberberg effect. The reason is that Saffman's calculations were based on a relative velocity between the fluid and the particle. This would require a force acting on the particle. However, the particles in the Segré-Silberberg effect are force-free. Still, the Saffman force can be used to influence the particles lateral position in the channel [H, 38, 88], which we demonstrate for deformable capsules in Sec. 6.5.

Wall-induced migration   Although the two effects we discussed so far are important for an understanding of inertial migration, they could not explain the Segré-Silberberg effect. To explain the formation of the annulus one needs a combination of the next two effects: the wall-induced migration and the shear-induced migration [7]. We begin by discussing the wall-induced migration. Ho and Leal found that a sphere in bound linear shear flow migrates toward the center between the two walls [7]. This demonstrates the repulsive character of the particle-wall interaction. Later, Zeng *et al.* did a deeper analysis of this repulsive particle-wall interaction and found that it is related to the vorticity generated on the surface of the particle [89]. This vorticity advects and diffuses downstream. The presence of the walls breaks the symmetry of the wake flow, which in turn creates secondary flows. This results in an effective lift force that pushes the particle away from the wall. In agreement with other simulations [32, 35] Zeng *et al.* observed an increase of the wall-induced lift force above Re ≈ 100, which then saturates for higher Reynolds numbers [89].

Shear-induced migration   The last missing ingredient is the inhomogeneous shear rate. Besides the linear shear flow, Ho and Leal calculated the force acting on a sphere in

a) circular
b) quadratic
c) rectangular
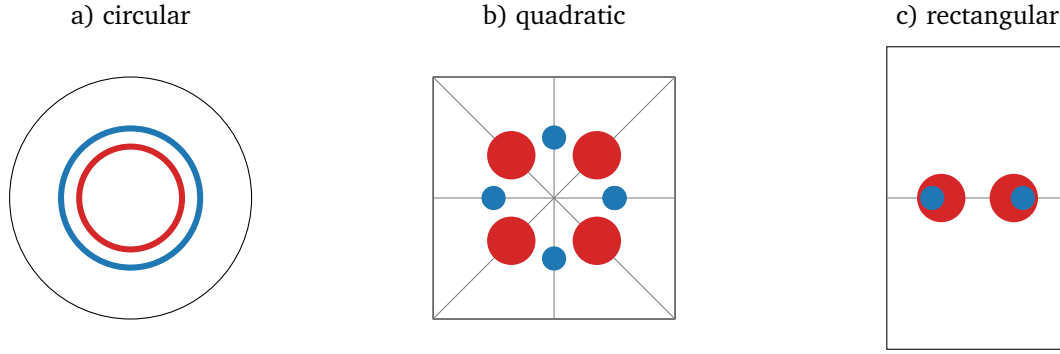
Figure 2.10: Equilibrium positions for different channel geometries and particle sizes. **(a)** In a cylindrical channel the particles are focused in an annulus. Larger particles (red ring) assemble closer toward the channel center than smaller particles (blue ring). **(b)** When a quadratic cross section is used only four equilibrium positions exists, which are either located on the main axis (smaller particles in blue) or on the diagonals (larger particles in red). The distance to the channel center is almost the same for large and small particles. However, the distance to the walls is larger for large particles. **(c)** For a rectangular cross section the number reduces even further to two. Similar to circular cross sections larger particle assemble closer to the center than smaller particles.

a Poiseuille flow [7]. They considered a particle of radius a which follows a pressure-driven flow between two infinite planes with the distance w. Due to the parabolic flow profile (*cf.* Sec. 2.4.7), any off-centered particle position leads to different relative velocities along the particle surface [Fig. 2.9 (c)]. This velocity difference creates a dynamic pressure which drives the particle toward the channel walls. Close to the walls this shear-induced migration is compensated by wall-induced migration and the particle settles in its equilibrium position around halfway between the channel center and the walls. In the limit of small shear particle Reynolds numbers $\mathrm{Re}_p \ll 1$ and small particles $a/w \ll 1$ Ho and Leal found

$$f_{\mathrm{shear}} \propto \rho u_m^2 a^4 / w^2 = \rho \nu^2 \mathrm{Re}^2 \left(\frac{a}{w} \right)^4 , \tag{2.65}$$

where u_{max} is the maximum fluid velocity in the channel center. They also found three equilibrium positions; an unstable fixed point in the channel center and two fixed points around halfway between the channel center and walls which is consistent to the Segré-Silberberg effect. It is important to note that the inertial lift force scales quadratically with the Reynolds number. In this work we use this scaling to distinguish between viscous effects $\propto \mathrm{Re}$ and inertial effects $\propto \mathrm{Re}^2$.

2.5.6 Equilibrium positions in channels with non-circular cross sections

Originally inertial focusing was observed in cylindrical channels where the shear-induced lift force and the particle-wall repulsion discussed in the previous section leads to the
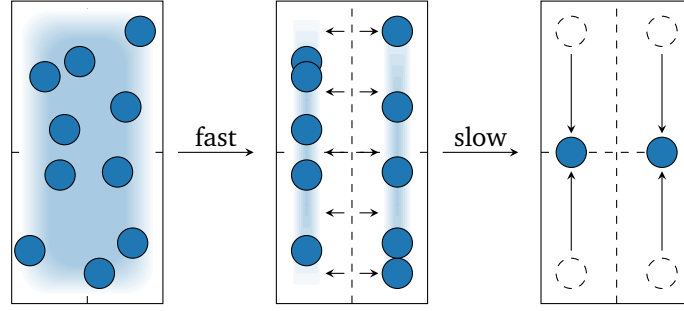
Figure 2.11: Illustration of the two-staged migration process in the channel cross section proposed by Ref. [37]. Initially the particles are uniformly distributed in the channel and move along the flow perpendicular to the paper plane (**left**). Due to the shear gradient the particles are first focused in two planes perpendicular to the short axis (**middle**). This process happens fast. In a second phase the particles move toward the short channel axis due to a rotation-induced migration (**right**). The smaller magnitude of the force results in a much slower process. The shaded areas illustrate the averaged particle distribution.

formation of an annulus (Fig. 2.10). If we change the channel to a quadratic cross section, the number of equilibrium positions reduces to four [15, 68]. If the two dimensions of the channel cross section, w and h, differ more than $w/h < 2/3$, the number of equilibrium points is reduced to two [38, 55].

Furthermore, experiments and simulations show that the equilibrium positions of larger particles are located further away from the channel wall [15, 40]. In the case of channels with quadratic cross section, simulations report that larger particles further increase the distance to the walls by moving toward the channel diagonals, while smaller particles assemble on the main axis. [34, 38, 84]. In experiments, however, all particles migrate toward the main axis, independent of their size [53]. One possible explanation why larger particle travel toward the diagonals only in simulation is that in experiment the channel walls bulge due to high pressure [13]. Typically, three walls of the channel are made of polymers while the fourth wall is made of glass, ensuring the best possible resolution for optical imaging. As the deformation depends on the material, the diagonal positions are no longer symmetric. Prohm showed numerically, that already for minimal deviations of the aspect ratio from $w/h = 1$ the equilibrium positions for larger particles ($a/w \geq 0.3$) move from the diagonals to the main axis [84].

Initially it is not obvious, why the number of equilibrium positions is reduced in non-circular geometries. Considering only the two forces used to explain the annulus in a cylindrical pipe one could also expect a band of particles in a channel with quadratic cross section. Indeed, such bands of particles parallel to the walls are reported in experiments during the initial phase of the inertial focusing [67]. To explain the reduced set of equilibrium positions Zhou and Papautsky proposed a *two-staged migration model* [37]. We discuss this model for the case of a rectangular cross section although it is also valid for quadratic cross sections.

In a rectangular channel the particles are first pushed toward the walls by shear-induced
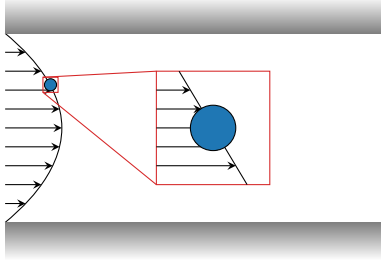
Figure 2.12: Illustration of the matched asymptotic analysis. The system is split into two subsystems: the inner and the outer region. In the inner region the flow around the particle is approximating the channel flow as a linear shear flow. In the outer region the channel walls and the far field perturbation induced by the particle are considered.

migration (Fig. 2.11). This process happens fast and the particles form a band parallel to the longer axis. Here the force due to the shear gradient and the walls compensate each other. Due to the parabolic flow profile, the shear rate in this region is relatively high. In such a case, Cherukat and McLaughlin have shown that rotation-induced migration [*cf.* Eq. (2.63)] becomes relevant [90]. This rotation-induced force induces a slow migration toward the final equilibrium position. Only at high Reynolds numbers Re > 200 shear-induced migration dominates over rotation-induced migration and also four equilibrium positions were found in rectangular channels located along the main axes [55, 91].

2.5.7 Basics of matched asymptotic expansion

As mentioned in Sec. 2.5.5 all analytical calculations for the inertial migration mechanisms were based on the matched asymptotics method. Here we want to briefly outline the idea of this method and follow the work of Schonberg and Hinch [8].

The general idea is to separate the problem into an inner and an outer region (see Fig. 2.12). The inner region around the particle is dominated by viscous stresses. Here, it is sufficient to use the Stokes equation. In the inner region the channel boundary is ignored and only a linear approximation of the flow profile of the channel flow is used. In the outer region the inertia is of similar order as the viscous stresses and the disturbance flow of the particle is described as a point disturbance. As the disturbance flow is weak, the Oseen equation in Eq. (2.5.2) can be used in the outer region. Finally, both solutions are matched asymptotically such that the inner solution converges to the outer solution as the channel walls are approached. At the same time the outer solution has to converge to the inner solution when approaching the particle.

We consider a small, rigid sphere with radius a, which flows in a channel filled with a Newtonian fluid. The particle is neutrally buoyant and is much smaller than the channel width $2w$. The ratio of particle diameter and channel width is our expansion parameter $\alpha = a/w \ll 1$. The center of the coordinate system is placed in the center of the sphere. We denote the undisturbed velocity flow field by $\boldsymbol{u}$ and the disturbance flow field by $\boldsymbol{u}'$.

For the inner solution we use the fact that the particle is small. This allows us to approximate the channel flow by a linear shear profile $u(x) = v + \gamma(x_p)(x - x_p)$, where x_p is the lateral position of the particle and γ is the local shear rate. Near the particle the flow is governed by viscous stresses and the Stokes equation is sufficient to describe the flow field.

Batchelor finds for the disturbance field $\boldsymbol{u}'_{\text{inner}}$ of a force and torque free particle [74],

$$\boldsymbol{u}'_{\text{inner}}(\boldsymbol{x}) = -\frac{5\gamma}{2|\boldsymbol{x}|^5}xz\boldsymbol{x} + \mathcal{O}(|\boldsymbol{x}|^{-4})\,, \qquad (2.66)$$

which is the disturbance flow created by the stresslet of a particle in linear shear flow. This flow decays rapidly with the distance from the particle and is thus consistent with the outer flow field.

For the outer region we only consider the far field disturbance created by the particle. As mentioned above, this disturbance flow is that of a stresslet. Saffman showed that such a disturbance flow can be expressed as a singular body force in the steady-state Oseen equation [6, 8]

$$(\boldsymbol{u}' \cdot \nabla)\boldsymbol{u}_0 = -\frac{\nabla p'}{\rho} + \nu\nabla^2\boldsymbol{u}' - \frac{10\pi a^3\nu\gamma}{3}\left(\hat{\boldsymbol{e}}_x\partial_z + \hat{\boldsymbol{e}}_z\partial_x\right)\delta(\boldsymbol{x})\,. \qquad (2.67)$$

This body force yields the correct far field for the inner solution. The equation cannot be solved analytically but requires some numerical treatment. The results agree well with the experiments by Segré and Silberberg up to relatively high Reynolds number around 100 [8]. Asmolov extended the calculations up to channel Reynolds numbers of 3000 while still considering only small particles and small particle Reynolds numbers [92]. Asmolov was able to determine that the lift force scales $f_{\text{lift}} \propto a^4$. In recent years Hood *et al.* used similar asymptotic calculations to study the inertial migration in a quadratic channel cross section even for cases where $\alpha = a/w = \mathcal{O}(1)$ and $\mathcal{O}(\alpha^2\text{Re}) \approx 10$ [93]. Using numerical methods to solve their equations Hood *et al.* were able to show that the scaling of the lift force changes to a^3 for particles $a/w > 0.06$. This result agrees with the experiments [15].

2.6 Soft capsules in flow

So far we have limited ourselves to solid, spherical particles. However, as we mentioned in the introduction, one of the main applications of lab-on-a-chip devices is the sorting of biological cells. These biological cells have properties very different from rigid spheres. Typically, they are deformable and filled with a complex fluid with a strong viscosity difference between the inner and outer fluid (viscosity contrast). This adds additional complexity to the problem and introduces new effects.

Most of the analysis on deformable particles was done in the regime of the Stokes equations, and we also restrict the following discussion to that case [49]. The deformability breaks the kinematic reversibility of the Stokes equations and allows for cross-streamline migration even in the case of vanishing Reynolds number. Typically, such deformable particles migrate toward the channel center [94], in contrast to rigid particle, where no cross-streamline migration is possible. The migration of deformable capsules is important for many biological processes. One prominent example is the decrease in the viscosity of blood when it flows through narrow blood vessels, the Fåhræus-Lindqvist effect [95]. Due

to the inwards directed migration a cell-free layer forms at the vessel walls which reduces the mean viscosity of the fluid.

In this section we shortly review the basic migration mechanisms of deformable particles in Stokes flow. We first discuss the different types of deformable particles. We continue by introducing our model for deformable capsules and the corresponding dimensionless numbers. Finally, we shortly review two analytical results for the capsules: the deformability-induced lift force and the deformation index. The effects of inertia on deformable capsules is discussed in Ch. 6. Before we discuss the analytical solutions, we first introduce the different types of deformable particles.

2.6.1 Types of deformable particles

Deformable particles are categorized in three classes: droplets, vesicles, and capsules. In this work we focus on capsules. However, we will briefly discuss the differences between the three types.

Droplets form when two immiscible fluids are combined in one flow. The behavior of droplets is determined by their surface tension. Due to their liquid interface they have no constraint on their area and can even break apart or join with other droplets. Still, the total volume of the droplets is conserved.

In contrast to droplets, vesicles are formed by lipid bilayers, which add a constraint on the area and the volume of each vesicle. Their form is governed by a strong bending rigidity [49, 96].

The third type of deformable particles are capsules, which are fluid-filled shells made of polymers [49]. They enclose a constant volume but can elastically dilate their surface area. The surface dynamics is dominated by shear and area dilation elasticity. Additionally, the membrane exhibits a small bending rigidity [97].

2.6.2 Modeling of soft capsules

In the following we introduce the physical model for deformable capsules. Capsules are dominated by the elastic properties of their membrane. We model the elasticity by an area dilation and a shear resistance. These two contribution are often described by one equation either by a (neo)-Hookean law or by the Skalak model. For this work, we use the Skalak model for the strain energy area density ϵ_S. The total strain energy E_S is given by the surface integral $E_S = \oint \epsilon_S \, dA$. In this section we introduce the idea behind the Skalak model, following Ref. [98].

We assume a homogeneous and isotropic membrane. Thus, the strain energy density depends only on the local dilation and deformation of the membrane characterized by the displacement gradient tensor $\boldsymbol{D}$. To understand the concept of the displacement gradient, it is helpful to consider a single flat triangle (see Fig. 2.13). In Fig. 2.13, an initially undeformed triangle with zero strain energy (a) is deformed (b). Based on our assumption

(a) (b) (c)
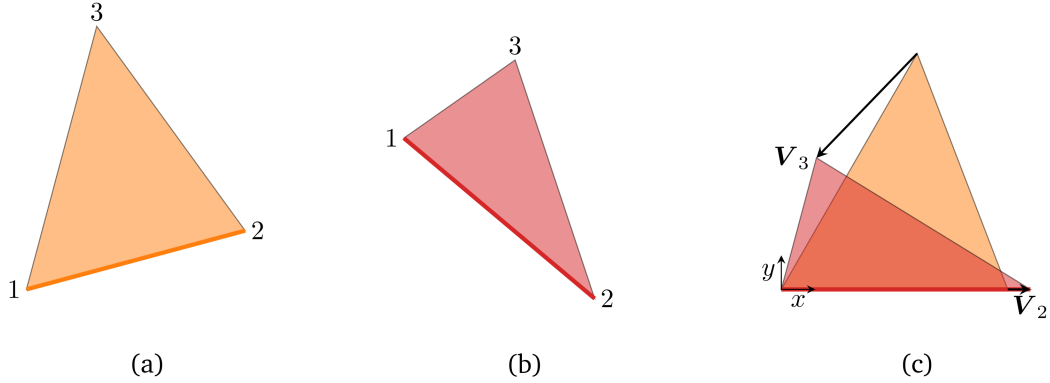
Figure 2.13: Deformation of a triangle. The triangle is made up by three vertices (1,2,3). The change of the undeformed triangle **(a)** to the deformed triangle **(b)** can be described via the displacement vectors $\boldsymbol{V}_i$ with $i = 1, 2, 3$. When we choose $\boldsymbol{V}_1 = 0$ and align the thick edges of both triangles, the deformation is uniquely defined by $\boldsymbol{V}_2$ and $\boldsymbol{V}_3$ **(c)**.

that the ϵ_S is independent of the position and rotation, we can align the two states as shown in (c). The deformation of (b) is now fully characterized by the two deformation vectors $\boldsymbol{V}_2$ and $\boldsymbol{V}_3$. We now assume that the displacement of every point in this triangle is described by the continuous displacement $\boldsymbol{V}$, which varies linearly over the triangle face. Furthermore, we approximate the membrane by an infinitesimally thin sheet. Hence, it is sufficient to describe the membrane in 2D. The displacement gradient tensor is given by

$$\boldsymbol{D} = \begin{pmatrix} D_{xx} & D_{xy} \\ D_{yx} & D_{yy} \end{pmatrix} = \begin{pmatrix} 1 & 0 \\ 0 & 1 \end{pmatrix} + \begin{pmatrix} \partial_x V_x & \partial_y V_x \\ \partial_x V_y & \partial_y V_y \end{pmatrix} \tag{2.68}$$

Since the strain energy density is independent of the rotation and translation it can only depend on the invariants of this tensor $\boldsymbol{D}$. These invariants are the eigenvalues λ_1 and λ_2. Alternatively one can use the so-called strain invariants $I_1 = \lambda_1^2 + \lambda_2^2 - 2$ and $I_2 = \lambda_1^2 \lambda_2^2 - 1$ which describe the strain and dilation state of the membrane, respectively [99].

The strain energy density $\epsilon_S(I_1, I_2)$ is given by a constitutive model. Such a constitutive model is not defined by the theory of elasticity, rather it is chosen to describe the stress-strain behavior of a given material as accurately as possible [98]. Here we use a model suggested by Skalak *et al.* which is often used to reproduce experimental data of red blood cell at small and large strain [48],

$$\epsilon_S = \frac{\kappa_s}{12} \left(I_1^2 I_1 - 2I_2 \right) + \frac{\kappa_a}{12} I_2^2 \,. \tag{2.69}$$

This formula has two contributions: κ_s penalizes deformations of the surface and κ_a controls the local area dilation.

Additionally, we use bending rigidity to prevent the formation of cusps in strong shear rates. The corresponding energy is given by the Canham-Helfrich functional [100, 101],

$$E_B = \kappa_b \int_A 2(H - H_0)^2 \, \mathrm{d}A + \kappa_k \int_A K \, \mathrm{d}A \,, \tag{2.70}$$

where κ_b is the bending modulus, H is the mean curvature, H_0 is the reference curvature, K is the Gaussian curvature and κ_k is the Gaussian modulus. The Gaussian curvature is constant as long as the topology of the object does not change [101, 102]. The change of the topology corresponds to the formation of holes in the membrane or its rapture. As we do not model such behavior in our simulations the second integral reduces to a constant and thus can be neglected in the force calculation [103].

The remaining integral, characterizing the bending rigidity, can be implemented in different ways [104]. For deformable capsules the bending does not significantly contribute to the dynamics and it is only used to prevent mesh degeneration. We use a direct discretization of the Canham-Helfrich functional Eq. (2.70) [102]

$$E_B \approx 2\sqrt{3}\kappa_b \sum_{ij}(1 - \cos\theta_{ij}) \tag{2.71}$$

where the sum runs over all connected vertices and θ_{ij} is the angle between the normal vectors of two neighboring faces of the discretized mesh.

Finally, we also consider an energy contribution for the volume conservation,

$$E_V = \frac{\kappa_v}{2}\frac{\left(V - V^{(0)}\right)^2}{V^{(0)}}\,, \tag{2.72}$$

where κ_v is the elastic bulk modulus, V the volume of the capsule, and $V^{(0)}$ the volume of the spherical initial state. This energy contribution ensures that the volume inside the capsules is conserved as our simulation method is not guaranteed to be divergence free as we will discuss in the next chapter.

No additional energy contribution is needed to ensure the local area conservation, as it is already incorporated in the Skalak model via the second term in Eq. (2.69).

To sum up, our model for the deformable capsules introduces four different κ: the shear modulus κ_s, the area dilation modulus κ_a, the bending modulus κ_b, and the compressibility κ_v. To reduce the dimension of our parameter space we follow Krüger *et al.* and fix the ratios of the area and the bending moduli to the shear modulus [36],

$$\kappa_a/\kappa_s = 2\,, \qquad \kappa_b/(\kappa_s a^2) = 2.87 \cdot 10^{-3}. \tag{2.73}$$

The ratio of bending to shear modulus is close to the experimental ratio of red blood cells[1] $\kappa_b/(\kappa_s a^2) = 3.5 \cdot 10^{-3}$ [10, 105]. However, the ratio of area to shear modulus in biological cells is much higher ($\kappa_a/\kappa_s = 100$) [9] compared to our parameters. Still, biological cells can deform due to their non-spherical shape. In this study we concentrate on spherical initial cell shapes, since we are interested in the general behavior of deformable capsules. Increasing one or both of the ratios in Eqs. (2.73), we expect that the capsule deforms less and behaves more like a rigid particle. Finally, we chose $\kappa_v = 300\,000\rho\nu^2/w^2$ such that the volume changes were less than 1%.

---

[1]The other parameters are $\kappa_b = 2 \cdot 10^{-19}\,\text{Nm}$, $\kappa_s = 5.3 \cdot 10^{-6}\,\text{Nm}^{-1}$ and $a_{\text{eff}} = 3.3\,\mu\text{m}$

2.6.3 Characteristic numbers for deformable capsules

In Sec. 2.4.1 and Sec. 2.4.5 we introduced the concept of non-dimensional numbers to describe the fluid. The most prominent number used in this work is the Reynolds number which quantifies the fluid inertia. The model of the deformable capsules introduces a couple of new parameters in the form of the moduli κ. These moduli influence the deformability of the capsules, which we want to quantify using non-dimensional parameters.

In the literature deformable particles are typically characterized by the capillary number Ca, which is the ratio of the shear stress $\rho \nu u_{\max}/w$ and the typical elastic stress κ_s/a

$$\mathsf{Ca} = \frac{\rho \nu u_{\max} a}{w \kappa_s} \,. \tag{2.74}$$

We note that the capillary number depends explicitly on the flow speed $u_{\max}$. This intrinsically couples the deformability of the particle (κ_s) with velocity effects (*e.g.* fluid inertia). To separate these two contributions we replace the capillary number by the Laplace number La. The Laplace number is connected to the particle Reynolds number $\mathsf{Re}_p = \mathsf{Re}(a/w)^2$ and the capillary number via

$$\mathsf{La} = \frac{\mathsf{Re}_p}{2\mathsf{Ca}} = \frac{\kappa_s a}{\rho \nu^2} \,. \tag{2.75}$$

The factor of 1/2 is due to our definition of the Reynolds number using the full channel width $\mathsf{Re} = 2u_{\max}w/\nu$ [*cf.* Eq. (2.20)]. The Laplace number is the ratio between typical elastic shear forces $\kappa_s a$ and the intrinsic viscous force scale $\rho \nu^2$ of the fluid. This number allows us to describe the deformability of the capsule independently of the flow velocity. Particle which are more rigid (larger κ_s) are modeled by larger Laplace numbers and smaller capillary numbers. In Ch. 6 we find that La is the proper quantity to describe the equilibrium distance of a deformable capsule from the channel center.

2.6.4 Migration of deformable capsules

As stated before, deformable capsules show cross-streamline migration even in the absence of fluid inertia. This does not contradict the calculations of Bretherton (*cf.* Sec. 2.5.4) as the deformable membrane breaks the kinematic reversibility of the Stokes equations. An analytic description of deformable capsules is in general quite difficult as their shape is hard to parameterize. However, in some cases analytical solutions can be found.

One of these cases is the deformability-induced lift force acting on a capsule. For small deformations (Ca $\ll$ 1) Helmy and Barthes-Biesel managed to determine the lift force on a deformable capsule in Poiseuille flow where they neglected interactions with the walls [106]

$$f_{\mathrm{lift}}(x) = 18\pi\eta u_{\max} x \mathsf{Ca} \left(\frac{a}{R_0}\right)^3 \frac{(5\mu - 17)}{2} \,, \tag{2.76}$$

where x is the distance from the center, u_{max} is the center velocity of the Poiseuille flow, R_0 is the radius of the pipe. Furthermore, μ is the Poisson ratio which is given for the Skalak model by $\mu = C/(1 + C) = 2/3$, where $C = \kappa_a/\kappa_s$ is the ratio between the area dilation and the shear modulus. We note that this form of the lift force differs by a factor of 3 from the result of Helmy and Barthes-Biesel due to a different definition of the capillary number. The force is directed toward the channel center, opposite to the lift force of the Segré-Silberberg effect.

2.6.5 Deformation index of capsules

As we stated before, the shape of deformable particles is hard to parameterize. However, using the Taylor deformation index D one can still determine the deformation of a particle without an exact parametrization of its surface. The Taylor deformation index is defined as

$$D = \frac{r_{\mathrm{max}} - r_{\mathrm{min}}}{r_{\mathrm{max}} + r_{\mathrm{min}}} \, . \tag{2.77}$$

The dimensions r_{max} and r_{min} are obtained by fitting an ellipsoid to the moment of inertia tensor of the capsule [107, 108]. For a spherical particle the deformation index is zero, while an infinitely stretched particle has a deformation index of 1.

In case of small capillary numbers, one can derive the deformation index of an elastic particle in a linear shear flow [109]

$$D = \frac{15}{4} \left(\frac{2 + \mu}{1 + \mu} \right) \mathsf{Ca} = 6\mathsf{Ca} = 3\frac{\mathsf{Re}}{\mathsf{La}} \frac{a^2}{w^2} \, , \tag{2.78}$$

where we used again that $\mu = 2/3$ for the Skalak model with $\kappa_a/\kappa_s = 2$.

In this chapter we introduced the relevant equations to understand the physics behind the Segré-Silberberg effect and the cross-streamline migration of deformable capsules. The next chapter is dedicated to the lattice-Boltzmann method which is used to solve these physical equations.

3

Simulation of fluid dynamics

The following chapter is dedicated to the mathematical and conceptual foundation of the simulation method. First we briefly introduce the kinetic Boltzmann equation and motivate the physical principles relevant for the simulation method. From there we discretize the velocity set and write down the lattice-Boltzmann equation. We show why the lattice-Boltzmann method is indeed suitable for simulating the Navier-Stokes equations and shortly review how fixed and moving boundaries can be implemented. Finally, we outline some numerical details, explain how we calculate forces, and introduce our unit system. This chapter follows in large parts Ref. [69].

3.1 Overview of computational fluid dynamics

The hydrodynamic equations introduced in Ch. 2 can be solved analytically for only a few systems. However, in systems with finite Reynolds numbers and moving, possibly deforming boundaries, solutions can only be obtained by simulations.

Typically, two different approaches are used in the field of computational fluid dynamics (CFD). The conventional solvers use a top-down method which directly discretizes and solves the macroscopic equations based on a fixed grid or mesh. Most common are the finite-volume method and the finite-element method. The implementation of these methods is generally straight-forward, yet, the non-linear and non-local characteristics of fluid dynamics require a careful choice of the numerical schemes. The solution of the hydrodynamic equations is typically obtained by solving a matrix inversion. This non-local problem is hard to parallelize.

Alternatively, particle-based simulation methods use a bottom-up approach and are based on microscopic or mesoscopic fluid descriptions. Some examples are the multi-particle collision dynamics (MPCD), dissipative particle dynamics (DPD) or the lattice-Boltzmann method (LBM). Typically, the fluid description in particle-based methods is simplified using virtual fluid particles with specific interaction rules. Most particle-based methods include thermal fluctuations at the level of particle dynamics, which makes them particularly

suitable for colloidal and active matter systems. In typical inertial microfluidic channels, however, the thermal fluctuations do not play a major role as the size of the particles is typically on the order of $10\,\mu$m. For these systems thermal fluctuations mostly lead to unwanted noise which increases the simulation time unnecessarily [84]. The lattice-Boltzmann method removes thermal fluctuations by utilizing the distribution function, rather than individual fluid particles. This athermal mesoscopic description of the fluid leads to a faster convergence of the simulations.

The particle-based methods do not directly implement the macroscopic fluid equations. Thus, it is not obvious that these methods solve the equations introduced in Ch. 2 and how the individual parameters of the methods relate to macroscopic transport variables, such as the viscosity. In case of the LBM the missing link is established by the Chapman-Enskop-expansion which we discuss in Sec. 3.3.4. First, we introduce the Boltzmann equation which is the conceptual foundation of the lattice-Boltzmann method.

3.2 The kinetic Boltzmann equation

In this section we briefly discuss the kinetic Boltzmann equation to introduce many of the concepts we will need for the lattice-Boltzmann method. Originally, the Boltzmann equation was derived for a kinetic gas which relaxes toward its equilibrium state via pair collisions. The key assumption of this description is that the time spend on collisions is short compared to the time between collisions ($t_{\mathrm{c}} \ll t_{\mathrm{mfp}}$, *cf.* Sec. 2.4.1). Additionally, the kinetic Boltzmann equation neglects three or more particle interactions and only considers elastic pair collisions. The typical length scale of this description is much smaller than the length scale of the continuum description but larger than the atomic length scale. This classifies the method as mesoscale. In the following, we derive the Boltzmann equation for a simple mono-atomic gas.

3.2.1 The distribution function and its moments

Before we write down the Boltzmann equation itself, we first characterize the particle distribution function. This distribution function is the fundamental variable of the kinetic theory. It represents the density of all particles with a velocity $\boldsymbol{\xi}$ at position $\boldsymbol{x}$ and time t.

The density ρ, the momentum density $\rho\boldsymbol{u}$, and the energy density E are given by the zeroth, first, and second moment of the distribution function:

$$\rho(\boldsymbol{x},t) = \int f(\boldsymbol{x},\boldsymbol{\xi},t)\,\mathrm{d}^3\xi\,, \tag{3.1a}$$

$$\rho(\boldsymbol{x},t)\boldsymbol{u}(\boldsymbol{x},t) = \int \boldsymbol{\xi} f(\boldsymbol{x},\boldsymbol{\xi},t)\,\mathrm{d}^3\xi\,, \tag{3.1b}$$

$$\rho(\boldsymbol{x},t)E(\boldsymbol{x},t) = \frac{1}{2}\int |\boldsymbol{\xi}|^2 f(\boldsymbol{x},\boldsymbol{\xi},t)\,\mathrm{d}^3\xi\,. \tag{3.1c}$$
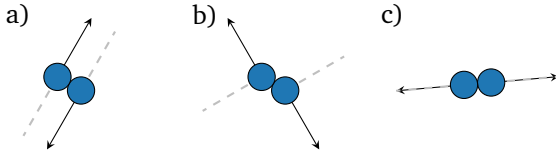
Figure 3.1: Basic collisions between hard spheres. Sliding collisions **(a)**, angled collisions **(b)**, and head-on collisions **(c)**. Incoming paths are dashed, outgoing paths are solid. Figure based on Ref. [69].

The energy density $E(\boldsymbol{x}, t)$ contains contributions of the internal energy $e(\boldsymbol{x}, t)$ due to thermal motion and kinetic energy $\frac{1}{2}\rho|\boldsymbol{u}|^2$ of the bulk motion. The internal energy density is given by

$$\rho(\boldsymbol{x}, t)e(\boldsymbol{x}, t) = \frac{1}{2}\int|\boldsymbol{v}|^2 f(\boldsymbol{x}, \boldsymbol{\xi}, t)\, \mathrm{d}^3\xi\,. \tag{3.2}$$

Here we use the relative velocity $\boldsymbol{v}(\boldsymbol{x}, t) = \xi(\boldsymbol{x}, t) - \boldsymbol{u}(\boldsymbol{x}, t)$ where we subtract the bulk motion $\boldsymbol{u}$ of the fluid. To connect the internal energy to the macroscopic temperature T or the pressure p we use the equipartition theorem of classical statistical mechanics. Each degree of freedom adds an energy contribution of $RT/2$ to the total internal energy [110], where R is the gas constant. A mono-atomic gas can only move along the three dimensions which leads to the internal energy density

$$\rho e = \frac{3}{2}\rho RT = \frac{3}{2}p\,, \tag{3.3}$$

where we use $\rho RT = p$ for an ideal gas.

Rearranging the equation we can relate the pressure to the relative velocity:

$$p(\boldsymbol{x}, t) = \frac{2}{3}\rho(\boldsymbol{x}, t)e(\boldsymbol{x}, t) = \frac{1}{3}\int|\boldsymbol{v}|^2 f(\boldsymbol{x}, \boldsymbol{\xi}, t)\, \mathrm{d}^3\xi\,. \tag{3.4}$$

This relates the pressure of an ideal gas with its internal kinetic energy.

3.2.2 The equilibrium distribution function

Next, we derive the equilibrium distribution. It is the last ingredient needed before we turn to the evolution of the distribution function, the Boltzmann equation. The kinetic theory assumes that the simple gas relaxes toward equilibrium via collisions. As collisions of particles strongly depend on the initial condition (Fig. 3.1), any angular dependency is removed over time. The resulting equilibrium distribution function should therefore be isotropic around the bulk velocity $\boldsymbol{u}$. Hence, the equilibrium distribution can be written as a function of the absolute value of the thermal velocity $|\boldsymbol{v}|$

$$f^{\mathrm{eq}}(\boldsymbol{x}, \boldsymbol{\xi}, t) = f^{\mathrm{eq}}(\boldsymbol{x}, |\boldsymbol{v}|, t)\,. \tag{3.5}$$

We further assume that the solution can be written as

$$f^{\mathrm{eq}}(|\boldsymbol{v}|^2) = f^{\mathrm{eq}}(v_x^2 + v_y^2 + v_z^2) = f_{\mathrm{1D}}^{\mathrm{eq}}(v_x^2)f_{\mathrm{1D}}^{\mathrm{eq}}(v_y^2)f_{\mathrm{1D}}^{\mathrm{eq}}(v_z^2)\,. \tag{3.6}$$

After some calculations, one finds the Maxwell-Boltzmann distribution [111]

$$f^{\mathrm{eq}}(\boldsymbol{x}, |\boldsymbol{v}|, t) = \rho\left(\frac{1}{2\pi RT}\right)^{3/2}\exp\left(-|\boldsymbol{v}|^2/(2RT)\right)\,. \tag{3.7}$$

3.2.3 The Boltzmann equation and the BGK-collision operator

We now know the equilibrium state and how we can determine macroscopic quantities from the particle distribution function. The remaining question is how the distribution function develops in time. Since f is a function of the position x, particle velocity ξ, and time t its total derivative is given by

$$\frac{\mathrm{d}f}{\mathrm{d}t} = \left(\frac{\partial f}{\partial t}\right) \frac{\mathrm{d}t}{\mathrm{d}t} + \left(\frac{\partial f}{\partial x_\alpha}\right) \frac{\mathrm{d}x_\alpha}{\mathrm{d}t} + \left(\frac{\partial f}{\partial \xi_\alpha}\right) \frac{\mathrm{d}\xi_\alpha}{\mathrm{d}t}, \tag{3.8}$$

where $\mathrm{d}_t x_\alpha = \xi_\alpha$ is the particle velocity and $\mathrm{d}_t \xi_\alpha = F_\alpha/\rho$ is the specific body force due to Newton's second law. We assume that the redistribution of the particle distribution function is due to collisions, which we represent by the collision operator $\Omega(f)$. The resulting equation is called the Boltzmann equation

$$\frac{\partial f}{\partial t} + \xi_\alpha \frac{\partial f}{\partial x_\alpha} + \frac{F_\alpha}{\rho} \frac{\partial f}{\partial \xi_\alpha} = \Omega(f). \tag{3.9}$$

The Boltzmann equation can be seen as an advection equation which transports the distribution function with the velocity ξ. The third term on the left-hand side captures the influence of forces on the velocity.

The original collision operator introduced by Boltzmann considered all possible outcomes of two-particle collisions in the form of a double integral over the velocity space. However, the resulting complicated collision operator can be approximated to simplify the analysis of the Boltzmann equation. A common approximation is the BGK collision operator named after its inventors Bhatnagar, Gross and Krook [112]. The BGK operator assumes that the distribution relaxes toward equilibrium with some relaxation time τ

$$\Omega(f) = -\frac{1}{\tau} \left(f - f^{\mathrm{eq}}\right). \tag{3.10}$$

Using a Chapman-Enskog expansion, which we introduce later in Sec. 3.3.4, one can connect the Boltzmann equation with the macroscopic description of the Navier-Stokes equations Eq. (2.15). Comparing the two differential equations, we find that the non-linear $(u \cdot \nabla)u$ term in the Navier-Stokes equations is not present in the Boltzmann equation. Even without the non-linear term, the Boltzmann equation is difficult to solve due to its increased parameter space. Solutions of the Boltzmann equation depend on x, ξ, and t resulting in a 7-dimensional parameter space in 3D. From a numerical point of view the situation is different. While the non-linear term in the Navier-Stokes equations is difficult to handle, the Boltzmann equation is an advection equation, which is easier to solve numerically. We discuss the numerical details of the lattice-Boltzmann method in the next section.

3.3 The lattice-Boltzmann method

The lattice-Boltzmann method originated from the lattice-gas simulation method, although it can also be derived via a discretization of the continuous Boltzmann equation. In the
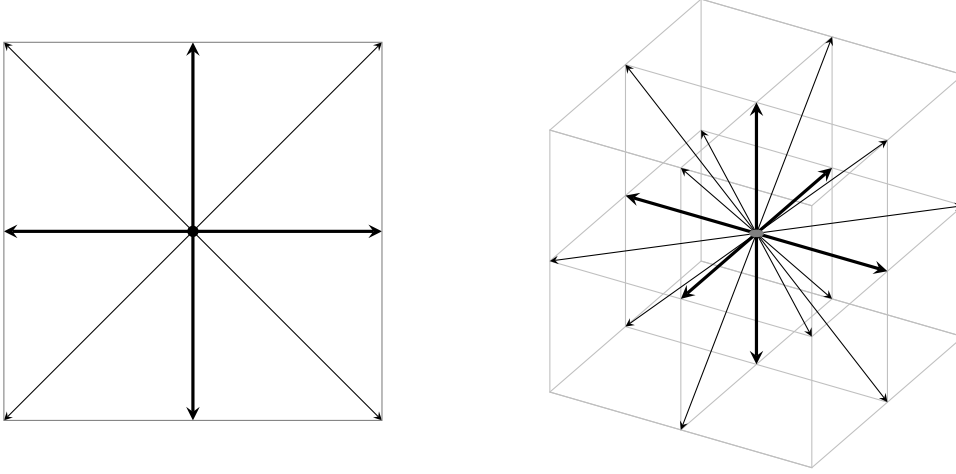
Figure 3.2: Set of velocity vectors for the D2Q9 (left) and the D3Q19 (right) implementation of the LBM. In 2D there is one velocity vector pointing to all surrounding lattice nodes and a zero velocity. In 3D 6 vectors point to the center of the faces, 12 to the center of the edges, and one velocity is the zero velocity. For clarity, we increase the thickness of the velocity vectors pointing to the next neighbors.

following we discuss some details of the lattice-Boltzmann method and show via the Chapman-Enskog expansion that it solves the Navier-Stokes equations.

3.3.1 Velocity discretization

The special feature of LBM is the cubic lattice structure and the discretization of velocities. Typically, only velocity vectors are allowed that point from one lattice node to one of the surrounding nodes, where the lattice spacing is usually set to $\Delta x = 1$. This discritized set of velocities is denoted by DdQq, where d is the number of spacial dimensions and q is the number of velocity vectors. Common velocity sets are D2Q9 in two dimensions or D3Q19 in three dimensions (Fig. 3.2).

To minimize the memory consumption and number of computations we want to use as few velocities as possible to determine the macroscopic moments: the density, the velocity, and the symmetric momentum flux tensor $\boldsymbol{\Pi}$. The momentum flux tensor is defined via $\Pi_{\alpha\beta} = \rho u_\alpha u_\beta - \sigma_{\alpha\beta}$, where $\boldsymbol{\sigma}$ is the sum of the viscous stress tensor and the isotropic pressure [*cf.* Eq. (2.10)]. To fully determine all macroscopic moments in 3D at least 10 velocities are required: one for density, three for velocity and six independent coefficients for the momentum flux tensor. In 2D at least 6 velocities are required.

The velocity sets can be derived via different ways. The mathematically rigorous way uses Hermite polynomials to prove that the macroscopic moments are exactly solved with a limited set of velocities [69]. This proof provides a strong mathematical basis for the lattice-Boltzmann method. However, the detailed derivation goes beyond the scope of this work, and we refer the interested reader to Ref. [113]. A more intuitive approach is to use the rotational isotropy of the lattice which has to be fulfilled by the velocity set [114].

Table 3.1: Velocities and weights for the D1Q3, D2Q9 and D3Q19 sets.

Notation	Velocities $\boldsymbol{c}_i$	Number	Weight w_i
D1Q3	(0)	1	2/3
	(± 1)	2	1/6
D2Q9	$(0,0)$	1	4/9
	$(\pm 1, 0), (0, \pm 1)$	4	1/9
	$(\pm 1, \pm 1)$	4	1/36
D3Q19	$(0,0,0)$	1	1/3
	$(\pm 1, 0, 0), (0, \pm 1, 0), (0, 0, \pm 1)$	6	1/18
	$(\pm 1, \pm 1, 0), (\pm 1, 0, \pm 1), (0, \pm 1, \pm 1)$	12	1/36

Each set of velocities $\boldsymbol{c}_i$ has a corresponding set of weights w_i. To reproduce the isotropic Navier-Stokes equations the velocity vectors of the cubic lattice need to be isotropic up to the fifth order [115, 116]. This leads to the following conditions

$$\sum_i w_i = 1\,, \tag{3.11a}$$

$$\sum_i w_i c_{i\alpha} = 0\,, \tag{3.11b}$$

$$\sum_i w_i c_{i\alpha} c_{i\beta} = c_s^2 \delta_{\alpha\beta}\,, \tag{3.11c}$$

$$\sum_i w_i c_{i\alpha} c_{i\beta} c_{i\gamma} = 0\,, \tag{3.11d}$$

$$\sum_i w_i c_{i\alpha} c_{i\beta} c_{i\gamma} c_{i\mu} = c_s^4 \left(\delta_{\alpha\beta}\delta_{\gamma\mu} + \delta_{\alpha\gamma}\delta_{\beta\mu} + \delta_{\alpha\mu}\delta_{\beta\gamma} \right)\,, \tag{3.11e}$$

$$\sum_i w_i c_{i\alpha} c_{i\beta} c_{i\gamma} c_{i\mu} c_{i\nu} = 0\,, \tag{3.11f}$$

where c_s is the speed of sound, which is given by $c_s = 1/\sqrt{3}(\Delta x/\Delta t)$ for most velocity sets (including the ones mentioned here) [117]. Additionally, all weights w_i have to be positive. The velocities and the corresponding weights for the D1Q3, D2Q9 and the D3Q19 sets are listed in Tab. 3.1 and illustrated in Fig. 3.2.

3.3.2 The lattice-Boltzmann equation and the BGK-collision operator

Using the previously derived discrete velocities of Tab. 3.1 the moment integrals Eq. (3.1) reduce to simple sums:

$$\rho(\boldsymbol{x}, t) = \sum_i f_i(\boldsymbol{x}, t), \qquad \rho\boldsymbol{u}(\boldsymbol{x}, t) = \sum_i \boldsymbol{c}_i f_i(\boldsymbol{x}, t). \tag{3.12}$$
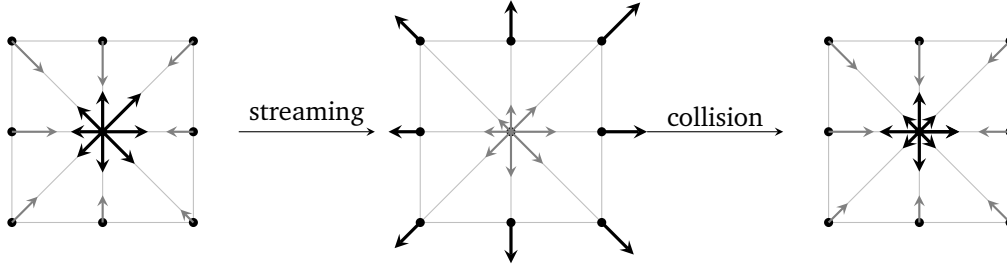
Figure 3.3: Steaming and collision in the lattice-Boltzmann method in a D2Q9 grid. The length of each vector quantifies the population f_i. The populations are transported along the individual velocity vectors (streaming). In the collision step the macroscopic variables are calculated individually for each lattice node and the populations are relaxed toward the corresponding equilibrium distribution (shown for $\tau = \Delta t$).

Importantly, for each lattice point $\boldsymbol{x}_i$ and every independent velocity vector $\boldsymbol{c}_i$ a corresponding distribution $f_i(\boldsymbol{x}, t)$ exists, typically called population. The evolution of these discrete distribution functions is given by the lattice-Boltzmann equation

$$f_i(\boldsymbol{x} + \boldsymbol{c}_i \Delta t, t + \Delta t) = f_i(\boldsymbol{x}, t) + \Omega_i(\boldsymbol{x}, t). \tag{3.13}$$

This equation describes the flow of "particles" from one lattice node at position $\boldsymbol{x}$ to a neighboring lattice node at $\boldsymbol{x} + \boldsymbol{c}_i \Delta t$ with velocity $\boldsymbol{c}_i$. At the same time particles are influenced by the collision operator Ω_i, which models the redistribution of populations at each site. The simplest implementation of Ω is a discritized BGK collision operator [*cf.* Eq. (3.10)]

$$\Omega_i(\boldsymbol{x}, t) = -\frac{f_i(\boldsymbol{x}, t) - f_i^{\text{eq}}(\boldsymbol{x}, t)}{\tau} \Delta t, \tag{3.14}$$

which relaxes the distribution function toward equilibrium with a single relaxation time τ. Other collision operators exist, such as the multi-relaxation time (MRT) [118, 119] collision operator or entropic models [120]. However, in this work we exclusively use the BGK collision.

The BGK collision operator relaxes the particle distribution function toward the equilibrium distribution. For the continuous Boltzmann equation f^{eq} is given by the Maxwell-Boltzmann distribution [Eq. (3.7)]. This exponential form is problematic for numerical simulations as its evaluation is computationally expensive. However, as mentioned earlier the framework of the Hermite polynomials proves that it is sufficient to expand the exponential function up to second order to fulfill the conservation laws [69]:

$$f_i^{\text{eq}}(\rho, \boldsymbol{u}) = w_i \rho \left(1 + \frac{\boldsymbol{u} \cdot \boldsymbol{c}_i}{c_s^2} + \frac{(\boldsymbol{u} \cdot \boldsymbol{c}_i)^2}{2 c_s^4} - \frac{\boldsymbol{u} \cdot \boldsymbol{u}}{2 c_s^2} \right), \tag{3.15}$$

where w_i are the weights of the specific velocity set and c_s is the speed of sound. The density ρ and the velocity $\boldsymbol{u}$ are calculated via Eq. (3.12). The equilibrium distribution is

defined such that its moments are the same as those of f_i, *i.e.*

$$\sum_i f_i^{\text{eq}} = \sum_i f_i = \rho, \tag{3.16a}$$

$$\sum_i \boldsymbol{c}_i f_i^{\text{eq}} = \sum_i \boldsymbol{c}_i f_i = \rho \boldsymbol{u}. \tag{3.16b}$$

This implies a conservation of mass and momentum during collisions. The implementation of the lattice-Boltzmann equation with BGK collision is typically done by performing two alternating steps: the collision and streaming step (Fig. 3.3)

$$\text{the collision step: } f_i^*(\boldsymbol{x}, t) = f_i(\boldsymbol{x}, t) - \frac{\Delta t}{\tau} \left(f_i(\boldsymbol{x}, t) - f_i^{\text{eq}}(\boldsymbol{x}, t) \right) \tag{3.17a}$$

$$\text{the streaming step: } f_i(\boldsymbol{x} + \boldsymbol{c}_i \Delta t, t + \Delta t) = f_i^*(\boldsymbol{x}, t). \tag{3.17b}$$

Here f_i^* represents the distribution function after the collision and the equilibrium distribution $f_i^{\text{eq}}(\boldsymbol{x}, t)$ is calculated from the pre-collision states of the distribution function. For details about the implementation and optimization we refer the interested reader to Ref. [69].

3.3.3 Body forces in the lattice-Boltzmann method

The lattice-Boltzmann equation Eq. (3.13) describes a system without external forces. However, we use a body force to drive the Poiseuille flow and also need to handle body forces $\boldsymbol{F}$ due to the immersed boundary method which we discuss in Sec. 3.4.

Including a body force in the LBM requires some refinement of the algorithms as otherwise the method loses its second-order accuracy and numerical artifacts corrupt the solution [121]. There are several methods to include a body force in the LBM which maintain second-order accuracy [69]. In this work we use the method introduced by Guo *et al.* [121]. The body force influences both the collision step in the lattice-Boltzmann equation and the calculation of the equilibrium distribution.

In the equilibrium distribution Eq. (3.15), we shift the momentum density by an amount equal to half the body force

$$\rho \tilde{\boldsymbol{u}}(\boldsymbol{x}, t) = \sum_i \boldsymbol{c}_i f_i(\boldsymbol{x}, t) + \frac{\Delta t}{2} \boldsymbol{F}. \tag{3.18}$$

Additionally, we extend the collision step by an extra source term S_i

$$f_i^*(\boldsymbol{x}, t) = f_i(\boldsymbol{x}, t) + (\Omega_i + S_i) \Delta t, \tag{3.19}$$

where the extra source term is given by

$$S_i = \left(1 - \frac{\Delta t}{\tau} \right) w_i \left(\frac{\boldsymbol{c}_i - \tilde{\boldsymbol{u}}}{c_s^2} + \frac{(\boldsymbol{c}_i \cdot \tilde{\boldsymbol{u}}) \cdot \boldsymbol{c}_i}{c_s^4} \right) \cdot \boldsymbol{F}. \tag{3.20}$$

Both modifications, Eq. (3.18) and Eq. (3.20), remove undesired derivatives in the macroscopic continuity and momentum equation caused by time discretization artifacts [69, 121].

3.3.4 Chapman-Enskog analysis

In 1917 Sydney Chapman and David Enskog independently developed a method to derive the macroscopic hydrodynamic equations from the Boltzmann equation. Later Chapman combined the two approaches into the Chapman-Enskog analysis [122]. Their method allows us to connect the mesoscopic details of the kinetic theory to macroscopic quantities such as the viscosity. In this section we discuss the Chapman-Enskog analysis for the lattice-Boltzmann equation following Ref. [69].

The Chapman-Enskog analysis is based on a perturbation expansion of the distribution function f_i around its equilibrium distribution f_i^{eq} in orders of the Knudsen number Kn. Instead of the Knudsen number one typically uses an expansion parameter $\epsilon \sim$ Kn. To get a consistent notation we will write the equilibrium distribution f_i^{eq} as $f_i^{(0)}$ in the following. The expansion of the distribution function gives

$$f_i = f_i^{(0)} + \epsilon f_i^{(1)} + \epsilon^2 f_i^{(2)} + \dots . \tag{3.21}$$

The expansion parameter ϵ allows us to group the terms according to their relative order in the Knudsen number, forming a set of semi-independent equations. In the following we use the BGK collision operator, Eq. (3.14), but a similar analysis can be done for other collision operators such as MRT [123]. In Eq. (3.16) we define the equilibrium distribution $f_i^{(0)}$ such that it yields the correct macroscopic quantities. Hence, the remaining non-equilibrium contribution $f_i^{\text{neq}} = f_i - f_i^{(0)}$ does not contribute to the density or momentum density. We assume that this condition has to hold in each order of the Knudsen number Kn

$$\sum_i f_i^{(n)} = 0 \quad \text{and} \quad \sum_i \boldsymbol{c}_i f_i^{(n)} = \boldsymbol{0} \quad \text{for all } n \geq 1 . \tag{3.22}$$

Next we expand the lattice-Boltzmann equation Eq. (3.13) up to second order

$$\Delta t \left(\partial_t + c_{i\alpha} \partial_\alpha \right) f_i + \frac{\Delta t^2}{2} \left(\partial_t + c_{i\alpha} \partial_\alpha \right)^2 f_i + \mathcal{O}(\Delta t^3) = -\frac{\Delta t}{\tau} f_i^{\text{neq}} . \tag{3.23}$$

From now on, we neglect third-order and higher derivatives as these terms are small and do not significantly affect the macroscopic behavior.

Before we consider the different orders in f_i, we expand the time derivative in terms of Kn

$$\partial_t f_i = \epsilon \partial_t^{(1)} f_i + \epsilon^2 \partial_t^{(2)} f_i + \dots , \qquad c_{i\alpha} \partial_\alpha f_i = \epsilon c_{i\alpha} \partial_\alpha^{(1)} f_i . \tag{3.24}$$

It is important to note that the different orders of the time derivative should not be considered as time derivatives themselves, as often claimed in the literature. Only the sum of all these terms is the time derivative. This expansion method is called multiple-scale

expansion and is also used in general perturbation theory. The different orders allow the treatment of unbounded terms by canceling them by the next higher order term [124]. This becomes clear in an analysis of the Poiseuille flow which yields that in steady state not each component vanishes individually. Rather, the individual components cancel each other [122]. Thus, the often used picture that the different orders in Kn correspond to different timescales can lead to false conclusions.

Now we combine the expanded forms of Eqs. (3.22), (3.23), and (3.24) and collect the terms of same order in Kn

$$\mathcal{O}(\text{Kn}): \qquad \left(\partial_t^{(1)} + c_{i\alpha}\partial_\alpha^{(1)}\right) f_i^{(0)} = -\frac{f_i^{(1)}}{\tau}\,, \qquad (3.25a)$$

$$\mathcal{O}(\text{Kn}^2): \qquad \partial_t^{(2)} f_i^{(0)} + \left(\partial_t^{(1)} + c_{i\alpha}\partial_\alpha^{(1)}\right)\left(1 - \frac{\Delta t}{2\tau}\right) f_i^{(1)} = -\frac{f_i^{(2)}}{\tau}\,. \qquad (3.25b)$$

The zeroth, first and second moments in $\mathcal{O}(\text{Kn})$ are obtained by multiplying Eq. (3.25a) with 1, $c_{i\alpha}$ and $c_{i\alpha}c_{i\beta}$ respectively and then summing over all states i:

$$\partial_t^{(1)}\rho + \partial_\gamma^{(1)}(\rho u_\gamma) = 0\,, \qquad (3.26a)$$

$$\partial_t^{(1)}(\rho u_\alpha) + \partial_\beta^{(1)}\left(\rho u_\alpha u_\beta + \rho c_s^2\delta_{\alpha\beta}\right) = 0\,, \qquad (3.26b)$$

$$\partial_t^{(1)}\left(\rho u_\alpha u_\beta + \rho c_s^2\delta_{\alpha\beta}\right) + \partial_\gamma^{(1)}\left(\rho c_s^2(u_\alpha\delta_{\beta\gamma} + u_\beta\delta_{\alpha\gamma} + u_\gamma\delta_{\alpha\beta})\right) = -\frac{1}{\tau}\Pi_{\alpha\beta}^{(1)}\,, \qquad (3.26c)$$

where

$$\Pi_{\alpha\beta}^{(1)} = \sum_i c_{i\alpha}c_{i\beta}f_i^{(1)}\,. \qquad (3.27)$$

This moment is undetermined but of first order and links the expanded equation of first and second order in Kn.

We now reverse the derivative expansion Eq. (3.24) and assume that only the first order of ϵ is relevant. This already yields the continuity and the Euler equations with $p = \rho c_s^2$. However, the viscous interaction, which distinguishes a fluid from a gas, is still missing.

If we furthermore take the zeroth and first moment of Eq. (3.25b) into account we find

$$\partial_t^{(2)}\rho = 0\,, \qquad (3.28a)$$

$$\partial_t^{(2)}(\rho u_\alpha) + \partial_\beta^{(1)}\left(1 - \frac{\Delta t}{2\tau}\right)\Pi_{\alpha\beta}^{(1)} = 0\,. \qquad (3.28b)$$

These two equations are second-order corrections to the first order Eqs. (3.26) above. Combining the moment equations and reversing the derivative expansion, this time with first and second order in Kn, we find

$$\partial_t\rho + \partial_\gamma(\rho u_\gamma) = 0\,, \qquad (3.29a)$$

$$\partial_t(\rho u_\alpha) + \partial_\beta\left(\rho u_\alpha u_\beta + \rho c_s^2\delta_{\alpha\beta}\right) = -\epsilon\partial_\beta\left(1 - \frac{\Delta t}{2\tau}\right)\Pi_{\alpha\beta}^{(1)}\,. \qquad (3.29b)$$

These two equations are the conservation equations for mass and momentum with an unknown viscous stress tensor

$$\sigma'_{\alpha\beta} = -\epsilon \left(1 - \frac{\Delta t}{2\tau}\right) \Pi^{(1)}_{\alpha\beta}. \tag{3.30}$$

The last piece is to determine this viscous stress tensor which can be done via Eq. (3.26c) but requires some algebraic reordering. For an isothemal equation of state and an equilibrium distribution expanded only to second order this yields [69]

$$\Pi^{(1)}_{\alpha\beta} = -\rho c_s^2 \tau \left(\partial^{(1)}_\beta u_\alpha + \partial^{(1)}_\alpha u_\beta\right) + \tau \partial^{(1)}_\gamma \left(\rho u_\alpha u_\beta u_\gamma\right). \tag{3.31}$$

The first term on the right-hand side corresponds to the viscous stress tensor in the Navier-Stokes equations. The second term is an error due to the second-order approximation of the equilibrium distribution. By comparing the magnitude of the first and second terms we find that the error is negligible if $u^2 \ll c_s^2$. This corresponds to the limit of small Mach numbers $\mathrm{Ma}^2 = (u/c_s)^2 \ll 1$ (*cf.* Sec. 2.4.1) and explains why the lattice-Boltzmann method is only valid for weakly compressible hydrodynamic problems [125].

Neglecting the $\mathcal{O}(u^3)$ error term and comparing Eqs. (3.29), (3.30), and (3.31) with the equations derived in Sec. 2.4 we find

$$p = \rho c_s^2 \quad \text{and} \quad \nu = c_s^2 \left(\tau - \frac{\Delta t}{2}\right). \tag{3.32}$$

These two equations relate the pressure p and viscosity ν to mesoscopic quantities of the LBM, the speed of sound c_s and the relaxation time τ.

3.3.5 Boundary conditions

Although boundary conditions only act on a small part of the volume they have a profound influence on the physical behavior of the fluid and the numerical quality of simulations. In the following we will briefly discuss the implementation of a no-slip boundary condition for a straight wall in the lattice-Boltzmann method. We assume that the boundary is aligned with the fluid lattice. Moving and more complex shaped boundaries needed for the particles are considered in the next section (Sec. 3.4).

The no-slip boundary condition mathematically belongs to the class of Dirichlet conditions where the value of the field is fixed on the boundary. The two other classes of boundary conditions are the Neumann condition which sets the derivative of the field on the boundary and the Robin condition which relates the value and the derivative of the field on the boundary.

The boundary conditions in LBM act on the boundary nodes. These boundary nodes are connected to at least one solid node and one fluid node. Solid nodes are located in the boundary and are neglected in the calculation of the populations f_i. The evolution of the
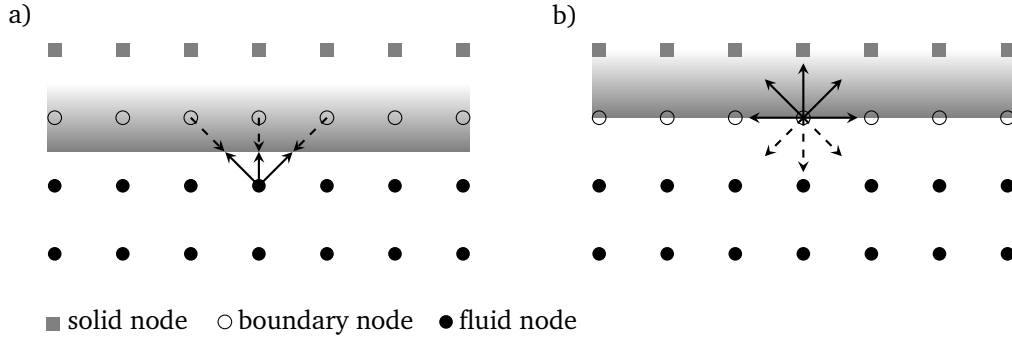
a)   b)

■ solid node   ○ boundary node   ● fluid node

Figure 3.4: Illustration of *link-wise* **(a)** and *wet-node* boundary **(b)** conditions in a lattice-Boltzmann D2Q9 grid. **(a)** For link-wise boundary conditions the solid-liquid interface is located between the last row of the fluid nodes and the boundary nodes. Here the no-slip boundary condition is ensured by reflecting the populations in the original direction (dashed vectors). **(b)** In case of wet boundary conditions the interface is located directly on the boundary nodes. On the boundary only some populations are known for the collision steps (solid lines). The unknown populations (dashed lines) need to be calculated.

boundary nodes follows the standard rules of LBM given by Eq. (3.17). However, the calculation of the populations originating from solid nodes need special consideration as they cannot be obtained by a streaming step. In LBM the boundary conditions are directly applied onto the populations instead of applying them on the macroscopic variables such as density or velocity. Thus, the populations are not uniquely defined by the boundary conditions. This results in a large variety of different schemes implementing the boundary conditions. In general LBM has two classes of boundary conditions: *link-wise* and *wet-node* boundary conditions (Fig. 3.4). The main difference is the position of the boundary. While for the *link-wise* boundary condition the boundary is located between the nodes, it is located on the nodes in case of *wet-node* conditions.

A prominent example of a *link-wise* scheme is the bounce-back condition which is popular due to its simplicity. Here the normal and tangential component of the incoming populations are inverted and streamed back in the original direction. While this method is easy to implement and numerically stable this boundary condition has the disadvantage that the exact location of the no-slip boundary condition is viscosity-dependent [69]. A Chapman-Enskog expansion for the boundary shows that in order to get a second-order accurate simulation method two terms need to compensate each other. To ensure that the two terms are equal, either the position of the interface must be shifted or a slip velocity must be introduced at the interface. This problem only exists in the BGK model and can be solved by using a more complex collision operator such as MRT.

In this work we use the regularized boundary condition proposed by Latt *et al.* [125, 126] which belongs to the class of *wet-node* boundary conditions. These *wet-node* conditions face the problem that only the populations of the fluid and boundary nodes are known (solid lines in Fig. 3.4). The unknown populations (dashed lines) need to be calculated while ensuring the boundary conditions and the conservation of mass and momentum.

This is possible at a straight wall, where enough populations are known to calculate the density, the momentum density and the momentum stress tensor.

The regularized boundary condition modifies all particle populations on a boundary node, not only the unknown, while keeping ρ and $\boldsymbol{u}$ unchanged. This leads to a more efficient implementation and increases the stability which allows the simulation of higher Reynolds numbers.

As a first step for the boundary condition we determine the macroscopic quantities from the known populations. The density can be calculated by the sum of the three components

$$\rho = \rho_- + \rho_+ + \rho_0 \tag{3.33}$$

where ρ_- is the sum of unknown particle populations, ρ_+ sums all populations opposite of the unknown ones and ρ_0 contains all populations tangential to the boundary. The velocity projected on the outwards pointing normal vector is given by

$$\rho u_\perp = \rho_+ - \rho_- \, . \tag{3.34}$$

Combining these two equations yields

$$\rho = \frac{1}{1 + u_\perp}(2\rho_+ + \rho_0) \tag{3.35}$$

which allows us to calculate the density independently of the unknown quantity ρ_-. When the velocity is prescribed on the boundary we can calculate the equilibrium population for the boundary nodes. A tempting approach would be to just use the equilibrium population to fill the unknown values at the boundary nodes. However, the Chapman-Enskog analysis showed that the non-equilibrium terms are important in order to obtain the correct stresses. Indeed, if one only uses the equilibrium populations the result fails to give the correct gradients at the boundary [125].

Instead, Latt *et al.* proposed to use a bounce-back rule on the non-equilibrium contribution $f_i^{(1)} = f_i - f_i^{\text{eq}}$ as a temporary value to calculate the macroscopic stress at the boundary $\boldsymbol{\Pi}^{(1)}$. This stress tensor then allows the calculation of all populations on the boundary node via [125]

$$f_i = f_i^{\text{eq}}(\rho, \boldsymbol{u}) + \frac{w_i}{2c_s^4}\boldsymbol{Q}_i : \boldsymbol{\Pi}^{(1)} \tag{3.36}$$

where $\boldsymbol{Q} = \boldsymbol{c}_i\boldsymbol{c}_i - c_s^2\mathbb{1}$. The recalculation is needed as the bounced-back non-equilibrium distribution may violate the velocity boundary condition. By using the recalculation ρ, $\boldsymbol{u}$ and $\boldsymbol{\Pi}^{(1)}$ are recovered correctly on the boundary.

3.4 Immersed boundary method

Implementing moving boundaries in simulation methods which rely on fixed cubic lattice structures, such as the Lattice-Boltzmann method, needs clever approaches. One solution is to approximate the moving boundary with cubes of the size of the lattice structure

and use a bounce-back-like boundary condition [127, 128]. However, this method can only handle rigid particles. Another solution uses an independent second mesh for the particle, which moves through the fluid mesh. This method is called immersed boundary method (IBM) and was originally proposed by Peskin in 1972 who used it to simulate flow patterns around heart valves using traditional CFD methods [129]. Feng and Michaelides first adapted the method to LBM [130]. While this method is less accurate than the bounce-back method, it allows the simulation of deformable particles.

The immersed boundary method uses the force density $\boldsymbol{F}(\boldsymbol{x}, t)$ in the Navier-Stokes equations to ensure the correct fluid properties on the boundary of the particle. This typically requires velocity interpolations of the fluid on the moving mesh and force spreading from the mesh onto the fluid. Moreover, using the force density instead of the lattice-Boltzmann populations allows combining the IBM with any fluid solver which incorporates a forcing of the fluid [131]. The advantage of the IBM is that it is easy to implement and it has a relatively small computational overhead, when implemented correctly. This allows the simulation of complex shapes and structures such as deformable cells or porous media [132, 133]. Furthermore, it solves the problem of recalculating the fluid mesh for a moving particle, which is by itself numerically expensive. However, a drawback of the method is that the moving boundary always encloses fluid nodes. The contained fluid can influence the exterior fluid if the immersed boundary is rotating [134]. This is especially relevant for the calculation of torques, while hydrodynamic forces are not effected. In order to compensate for the internal fluid, we apply Feng's rigid body approximation [135] and add an additional force acting on the particle so that it moves as a solid particle would move (see Sec. 3.4.3).

In this section we further introduce two different implementations of the immersed boundary method, one for rigid particles and one for deformable capsules, which are both relevant for this work. We will first discuss the common features and then describe the different algorithms in more detail.

3.4.1 Interpolation kernel

The important aspect of the immersed boundary method is the interpolation of the forces and the fluid velocity between the Eulerian and Lagrangian grids. The interpolation is implemented via an interpolation kernel. In the following we discuss its properties. We denote the coordinates and velocities of the fixed Eulerian grid by $\boldsymbol{x}$ and $\boldsymbol{u}(t)$ respectively while we denote the coordinates and velocities of the moving Lagrangian vertices by $\boldsymbol{r}(t)$ and $\boldsymbol{v}(t)$.

If we assume a moving boundary of an infinitesimal thickness the overlap between the fluid and moving mesh would be minimal or even non-existent. Peskin solved this problem by introducing a finite interpolation kernel $\phi(\boldsymbol{r}(t) - \boldsymbol{x}_i)$ which depends on the distance between the vertex and the lattice nodes [129]. This kernel function should be short-ranged and normalized. Furthermore, the kernel should consider only an envelope of two to four lattice nodes around each vertex to be numerically efficient (see different colors in Fig. 3.5). This envelope is large enough to reduce lattice artifacts. However, it also
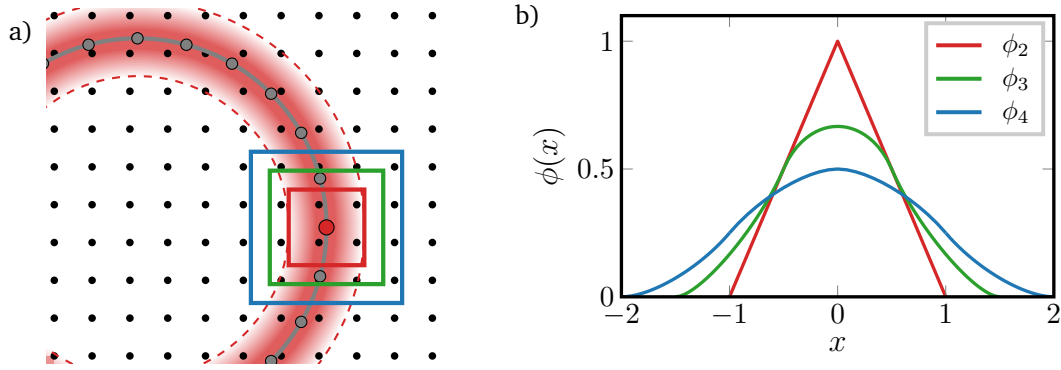
Figure 3.5: **(a)** Lagrangian boundary (gray) moving between the fixed Eulerian grid (black). Around each vertex of the Lagrangian mesh only lattice-points within the envelope width Δx are considered (red: $\Delta x = 2$, green: $\Delta x = 3$, blue: $\Delta x = 4$). The envelope gives the immersed boundary a certain thickness (red shaded area for envelop of $2\,\Delta x$). This increases the effective size of the particle from the gray line toward the red dashed line. **(b)** Interpolation kernel for the corresponding envelope functions.

introduces a certain width of the boundary which increases the hydrodynamic radius of the moving boundary [indicated by the outer red dashed line in Fig. 3.5 (a)] [135]. In his work Peskin proposed three different kernel functions ϕ, which consider all lattice nodes in a square of edge width $\Delta x =$ 2, 3 and 4 (red, green and blue squares in Fig. 3.5),

$$\phi_2(x) = \begin{cases} 1 - |x| & 0 \le |x| \le 1\,, \\ 0 & 1 \le |x|\,, \end{cases} \tag{3.37}$$

$$\phi_3(x) = \begin{cases} \frac{1}{3}\left(1 + \sqrt{1 - 3x^2}\right) & 0 \le |x| \le \frac{1}{2}\,, \\ \frac{1}{6}\left(5 - 3|x| - \sqrt{-2 + 6|x| - 3x^2}\right) & \frac{1}{2} \le |x| \le \frac{3}{2}\,, \\ 0 & \frac{3}{2} \le |x|\,, \end{cases} \tag{3.38}$$

$$\phi_4(x) = \begin{cases} \frac{1}{8}\left(3 - 2|x| + \sqrt{1 + 4|x| - 4x^2}\right) & 0 \le |x| \le 1\,, \\ \frac{1}{8}\left(5 - 2|x| - \sqrt{-7 + 12|x| - 4x^2}\right) & 1 \le |x| \le 2\,, \\ 0 & 2 \le |x|\,. \end{cases} \tag{3.39}$$

These forms are commonly used, however, other forms for the interpolation kernel were proposed as well [136]. In 3D the interpolation kernel can be expressed by $\Delta(\boldsymbol{x}) = \phi(x)\phi(y)\phi(z)$. In this work we use an envelope width of $\Delta x = 4$ [Eq. (3.39)] as this yields the best stability in our simulations.

3.4.2 Velocity interpolation and force spreading

Using the interpolation kernel we interpolate the fluid velocity of the Eulerian grid at position of the i-th mesh vertex via

$$\boldsymbol{v}_i(t) = \sum_{\boldsymbol{x}} \boldsymbol{u}(\boldsymbol{x}, t) \Delta(\boldsymbol{r}_i - \boldsymbol{x}) \,. \tag{3.40}$$

This interpolated velocity is used to determine a penalty force for a no-slip boundary condition and to directly integrate the vertex position. The forces $\boldsymbol{f}_i$ which are calculated on the moving boundary at position of the i-th vertex point are then spread back to fluid via

$$\boldsymbol{F}(\boldsymbol{x}, t) = \sum_{j} \boldsymbol{f}_j \Delta(\boldsymbol{r}_j - \boldsymbol{x}) \,. \tag{3.41}$$

We note that $\boldsymbol{f}_j$ is the total force acting on vertex j not to be confused with the force density $\boldsymbol{F}$.

The velocity interpolation in Eq. (3.40) can break the incompressibility of the enclosed volume. While the velocity field itself should be divergence-free, the interpolated velocities do no longer fulfill the divergence-free criterion. However, the LBM cannot even guaranty incompressibility of the fluid. To compensate for possible volume changes within the particle we apply a volume conservation directly to our deformable capsules (*cf.* Sec. 2.6.2).

For this work we use two different implementations of the IBM which we will discuss in the following. For rigid particles we follow Inamuro who proposed a penalty force to ensure the no-slip boundary condition, using an iterative procedure [137]. The deformable capsules adopt an algorithm introduced by Krüger *et al.* [132]. Here the forces of the constitutive model (*e.g.* area dilatation, bending, volume conservation) are calculated on the membrane and then spread onto the fluid nodes. The no-slip boundary condition is ensured by advecting the vertex points with the interpolated velocity.

3.4.3 Immersed boundary method for rigid particles

We first discuss the immersed boundary method for rigid particles. Multiple schemes exists to implement immersed boundaries (IB). Ref. [69] gives a broad overview of the different methods and their advantages and disadvantages. In summary, there are three different classes: implicit IB, multi direct-forcing IB and explicit IB. The implicit IB class is numerically very expensive and the explicit IB scheme lacks accuracy. Thus, we use a multi direct-forcing IB scheme, proposed by Inamuro, which offers a good trait-off between accuracy and speed [137]. The method ensures the no-slip boundary condition on the particle surface via an iterative process [137]:

Step 0 The uncorrected fluid velocity is interpolated on every vertex i. To ensure a no-slip boundary condition we introduce a penalty force which is given by

$$\boldsymbol{f}_i^{(0)} = \boldsymbol{V}_i - \boldsymbol{v}_i \tag{3.42}$$

where $\boldsymbol{V}_i = \boldsymbol{v}_{\text{particle}} + \boldsymbol{\Omega}_{\text{particle}} \times \boldsymbol{r}_i$ is the velocity of the vertex point and $\boldsymbol{v}_i$ is the interpolated velocity given by Eq. (3.40).

Step 1 The penalty force is spread back on the fluid using Eq. (3.41).

Step 2 The fluid velocity is calculated via Eq. (3.18), now including the penalty force.

Step 3 The velocities are interpolated on the boundary nodes.

Step 4 The penalty force is reevaluated

$$\boldsymbol{f}_i^{(l+1)} = \boldsymbol{f}_i^{(l)} + \boldsymbol{V}_i - \boldsymbol{v}_i \,, \tag{3.43}$$

where l is the iteration index.

Step 5 Repeat step 1–4 until $l = l_{\max}$.

Each time step we run this algorithm to compute the forces on the particles and the fluid. Then we iterate the fluid and the particles individually and proceed to the next time step. We follow Suzuki and Inamuro and use $l_{\max} = 5$ which is a good compromise between accuracy and efficiency [134].

The penalty force acts on the fluid via Eq. (3.19) and Eq. (3.20). The force on a rigid particle is given by the sum of all penalty forces over its

$$\boldsymbol{f}_{\text{fluid}} = -\sum_{\text{boundary}} \boldsymbol{f}_i^{l_{\max}} \,. \tag{3.44}$$

Likewise, the torque $\boldsymbol{T}_{\text{fluid}}$ is given by

$$\boldsymbol{T}_{\text{fluid}} = -\sum_{\text{boundary}} (\boldsymbol{r}_i - \boldsymbol{r}_c) \times \boldsymbol{f}_i^{l_{\max}} \tag{3.45}$$

with r_c the center of mass of the boundary.

One problem of this scheme is that the penalty force also considers contributions from the fluid inside the particles. To correct for the internal fluid, we implement the rigid body approximation proposed by Feng and Michaelides [135]. This correction introduces an additional force

$$\boldsymbol{f}_{\text{Feng}} = \frac{M}{\Delta t} \left[\boldsymbol{v}(t) - \boldsymbol{v}(t - \Delta t) \right] \,, \tag{3.46}$$

and torque

$$\boldsymbol{T}_{\text{Feng}} = \frac{I}{\Delta t} \left[\boldsymbol{\Omega}(t) - \boldsymbol{\Omega}(t - \Delta t) \right] \,. \tag{3.47}$$

For the time integration of the particle's trajectory we use the Verlet scheme [138]:

$$\boldsymbol{r}(t + \Delta t) = \boldsymbol{r}(t) + \boldsymbol{v}(t)\Delta t + \frac{1}{2} M^{-1} \left(\boldsymbol{f}_{\text{fluid}} + \boldsymbol{f}_{\text{Feng}} \right) \Delta t^2 \,, \tag{3.48}$$

$$\boldsymbol{v}(t + \Delta t) = \boldsymbol{v}(t) + M^{-1} \left(\boldsymbol{f}_{\text{fluid}} + \boldsymbol{f}_{\text{Feng}} \right) \Delta t \,, \tag{3.49}$$

$$\boldsymbol{\Omega}(t + \Delta t) = \boldsymbol{\Omega}(t) + I^{-1} \left(\boldsymbol{T}_{\text{fluid}} + \boldsymbol{T}_{\text{Feng}} \right) \Delta t \,. \tag{3.50}$$

In the case of pair trajectories shown later in Sec. 4.2 the two particles can touch each other. To avoid overlap of the particles, we use an event-based algorithm to integrate the trajectories of the particles. When the particles are so close that they would overlap in the next time step, we break the time step in two parts. In the first part, the step is reduced to $\Delta \tilde{t}$ so that the particles just touch, perform the collision between the particles, and finish the remaining time step with length $\Delta t - \Delta \tilde{t}$, using the updated values for the particle velocity and angular momentum. To realize the collision, we follow Ref. [138] and consider two rough hard spheres so that during collision also angular momentum is exchanged [138].

3.4.4 Immersed boundary method for deformable particles

The IBM proposed by Inamuro is well suited for rigid particles. For deformable particles we need a different algorithm that also considers the constitutive equations for the membrane model [132]:

Step 1 The forces acting on the vertex nodes are calculated, taking into account the deviation of the deformed state from a defined reference state.

Step 2 The forces are spread to the LBM grid via Eq. (3.41).

Step 3 The fluid is propagated to the next time step and the new fluid density $\rho(\boldsymbol{x}, t + \Delta t)$ and velocity $\boldsymbol{u}(\boldsymbol{x}, t + \Delta t)$ are calculated.

Step 4 The new fluid velocities are interpolated back onto the Lagrangian mesh via Eq. (3.40).

Step 5 The vertices are integrated using an Euler step method

$$\boldsymbol{r}_i(t + \Delta t) = \boldsymbol{r}_i(t) + \boldsymbol{v}_i(t)\Delta t \,. \tag{3.51}$$

Go back to **Step 1** and recompute for the next time step.

This algorithm does not enforce a strict no-slip boundary condition on the surface via a penalty force, rather the vertices move with the surrounding fluid velocity. The resulting deformation leads to forces which act on the fluid.

In our case, the forces are due to area dilatation, shear, bending and volume conservation, which are derived as an energy contribution E (*cf.* Sec. 2.6.2). The resulting force on vertex i is given by the principle of virtual work

$$\boldsymbol{f}_i = \frac{\partial E(\boldsymbol{r})}{\partial \boldsymbol{r}_i} \,. \tag{3.52}$$

The derivation of the individual forces is quite technical and goes beyond the scope of this thesis. For details on the implementation of the Skalak and volume forces we refer the reader to Ref. [98].

3.4.5 Particle mesh and parameters

In our simulation setups the particle surfaces are described as triangulated spheres, which we obtain by subdividing the faces of an isocahedron and projecting the vertices on a sphere. We choose a resolution which ensures that the spacing between the vertex nodes is smaller than the lattice spacing Δx.

Simulations of deformable capsules with immersed boundaries show the best accuracy for LBM relaxation times $\tau \leq 1$ or viscosities $\nu \leq 1/6$ [132]. Although this was only shown for deformable particles, we assume a similar behavior for the Inamuro scheme and apply the same rule for the rigid particles. Due to this restriction we tune the Reynolds number by adjusting the Mach number while keeping the viscosity fixed at $\nu = 1/6$. Depending on the resolution this procedure leads to a Mach number $\mathrm{Ma} > 0.1$ which can lead to compressibility effects (*cf.* Sec. 2.4.1). In this case we fix $\mathrm{Ma} = 0.1$ and increase the Reynolds number by reducing the viscosity ν.

3.5 Measurement of the lift force

The movement of particles in a microchannel is determined by the lift force profiles. In Ch. 4 and Ch. 6 we calculate the lift force profiles for a pair of rigid particles and a single deformable capsule. In the following we shortly describe how we measure the lift force. The lift force acts perpendicular to the flow direction, hence, to measure it we fix the lateral position of the particle and determine the resulting force. Similar to the IBM we use different mechanisms to fix the lateral position of rigid and deformable particles.

Rigid particles   As shown in Sec. 2.5.4, there can be no lift in the regime of the Stokes equation. Hence, the measured force is purely an inertial effect. For a single rigid particle we simply set the lateral movement to zero. This is equivalent to applying a force on the particle which exactly compensates the lift force. The lift force is given by the lateral component of Eq. (3.44).

We use the same method to determine the force acting on a pair of rigid particles. To ensure that the axial distance is fixed, we adjust the particle integrator so that both particles move with their combined center-of-mass velocity. However, this method introduces a small error. When the particles have a different distance from the channel center, we slow down the particle closer to the center while we accelerate the other particle relative to their free streaming velocity. This results in a slip velocity and thus a small force according to the Saffman effect (*cf.* Sec. 2.5.5). We did not find a way to correct for this. However, we expect the Saffman force to be small compared to the lift force.

Deformable particles   For a deformable capsule we can not just fix the lateral position as the membrane itself deforms such that it is force free. Here we need an adjustable

feedback force f_{fb} which compensates the inertial lift force and fixes the particles lateral position. When the particle does not move laterally,

$$\dot{\boldsymbol{x}}_{\mathrm{com}}^{\mathrm{lateral}} = \left(\boldsymbol{f}_{\mathrm{lift}} + \boldsymbol{f}_{\mathrm{fb}}\right) \Delta t = 0 \,, \tag{3.53}$$

the feedback force $f_{\mathrm{fb}} = -f_{\mathrm{lift}}$ compensates the lift force.

The feedback force is evenly distributed over all vertex nodes and given by a proportional-integral (PI) feedback controller [139]. Its strength has two contributions: The first contribution is *proportional* to the current offset, while the sum of all previous offsets is given by the *integral*

$$\boldsymbol{f}_{\mathrm{fb}}(t) = \gamma_p \left(\boldsymbol{x}_0 - \boldsymbol{x}_{\mathrm{com}}(t)\right) + \int\limits_0^t \gamma_i \left(\boldsymbol{x}_0 - \boldsymbol{x}_{\mathrm{com}}(t')\right) \mathrm{d}t' \,, \tag{3.54}$$

where γ_p and γ_i are the proportionality constants of the current and past time steps, respectively, and $\boldsymbol{x}_0$ is the targeted lateral position. It is important to note that deformable capsules also migrate in Stokes flow. So here the lateral force is a combination of inertial and deformability-induced lift.

3.6 Viscosity units

Internally, the computations are performed in lattice units ($\Delta x = 1$, $\Delta t = 1$ and $\rho = 1$). However, this parametrization depends rather on the numerical details of the employed lattice than on the physical properties of the system. To fix this, we express all quantities with physical properties such as the viscosity ν, density ρ and the channel width w. We call this scaling *viscosity units*. Our simulation results are easily compared to experiments with these units. The scaling of the different quantities is the following:

$$
\begin{aligned}
\text{length: } & l' = l/(2w) \,, & \text{position: } & \boldsymbol{x}' = \frac{1}{2w}(\boldsymbol{x} - \boldsymbol{x}_c) \,, \\
\text{time: } & t' = \frac{t\nu}{w^2} \,, & \text{velocity: } & u' = \frac{2uw}{\nu} \,, \\
\text{force: } & f' = \frac{f}{\rho\nu^2} \,, & \text{mass: } & m' = \frac{m}{\rho w^3} \,.
\end{aligned}
\tag{3.55}
$$

Here a primed variable X' denotes the rescaled quantity in viscosity units, whereas X denotes the unscaled quantity, either in simulation units or in physical units. Hence, length is expressed in units of half the channel width and time is expressed in units of the momentum diffusion timescale.

3.7 Simulation code

For the simulation of the lattice-Boltzmann method we extended the open source Palabos code [140]. The Palabos code is written in C++ and has a special emphasis on extendability

and parallelization. The code provides the framework for the fluid and the boundary conditions, including the Inamuro immersed boundary method (*cf.* Sec. 3.4.3). We supplement the Palabos code with custom modules for the mesh and the algorithm for the deformable capsules. Furthermore, we added periodic boundary conditions for the immersed boundary method and implemented the Euler integrator for the colloidal equations of motion. The code is based on the work by Christopher Prohm [84].

4

Dynamics of a pair of rigid particles

The dynamics of multiple particles is dominated by the pair interactions due to the strong confinement and the low particle density in inertial microfluidic devices. In this chapter we study the trajectories and the two-particle lift forces of a pair of rigid particles. First we analyze the different types of possible trajectories as a function of the initial lateral positions. We find three unbound types of trajectories, which we name moving-apart, passing and swapping, and one type of bound trajectory, where the particles perform damped oscillations. Furthermore, we analyze the two-particle lift force profile and perform a parameter study based on the lateral position, axial spacing, and Reynolds number. Finally, we connect the two-particle lift force profile with the damped oscillations. The chapter is based on the publication of Ref. [B], where these results are presented.

In the inertial regime a single particle performs cross-streamline migration in microchannels due to the inertial lift force (*cf.* Sec. 2.3). When the particle density increases the particles start to interact with each other and form multi-particle structures with a distinct axial spacing either as staggered or as linear trains (*cf.* Fig. 1.1). In staggered trains the particles have a typical axial spacing of around 4 particle radii, while in linear trains the spacing is about twice this distance. Before we study the stability of multi-particle structures in the next chapter, we first focus on the possible trajectories and the lift force profiles of a pair of rigid particles. We distinguish between cross-streamline and same-streamline pairs where the particles are located either on different sides of the channel or the same side.

At vanishing Reynolds numbers pair trajectories of rigid particles in Poiseuille flow show bound or unbound trajectories depending on their initial condition [141]. These trajectories can qualitatively be described by assuming that one particle follows the streamlines created by the flow distortion of the other particle [142]. For inertial microfluidics additional effects need to be considered. In particular, the flow field around a single particle changes noticeably for inertial microfluidics by losing the fore-aft symmetry [143, 144]. Furthermore, particle pairs move on damped oscillation trajectories toward their final configuration [47]. Similar to the explanation of pair trajectories at vanishing Reynolds numbers, Humphry *et al.* explained the oscillations and stability of the cross-streamline pairs in the inertial regime by inward spiraling eddies in the flow field around a single
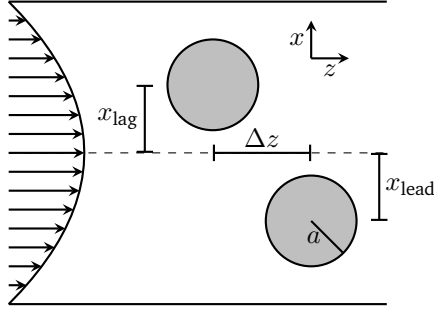
Figure 4.1: Pair of rigid particles in a Poiseuille flow in the x-z-plane where the flow is directed along the z-axis. The particle configuration is described by the axial distance Δz and lateral coordinates x_{lag}, x_{lead} (measured from the center line) for particles leading and lagging in flow, respectively.

particle [41]. This picture has been recently confirmed by analytical calculations [46]. The oscillations are attributed to viscous flow distortions, while damping is a result of the acting inertial force that pushes the particle toward its equilibrium position. For same-streamline pairs, thorough experimental and numerical analysis have been performed recently [42]. Usually, their particle distance is twice the distance of cross-streamline pairs. However, at higher particle Reynolds numbers the particle pair is reported to relax toward the same spacing as cross-streamline pairs [42]. Some experiments also observed an increase of the axial spacing over time [47]. Finally, it has been argued that the stability of such same-streamline pairs is a result of minimization of the kinetic energy of the fluid [46]. Furthermore, the authors showed by analytical calculations that the axial spacing of the particles is independent of the Reynolds number in the limit of small Re.

We discuss the stability of trains in more details in the next chapter. In this chapter we focus on the different trajectories of particle pairs and on the two particle lift force profiles.

4.1 Microfluidic setup

We study a pair of two rigid particles of same radius a, which we initialize in the x-z-plane at $y = 0$. For the setup we use the rectangular channel of length L as described in Fig. 2.6 (width $2w$, height $2h$, and aspect ratio $w/h = 0.5$). This aspect ratio reduces the number of equilibrium positions to two, located on the short axis (*cf.* Sec. 2.5.6). We employ periodic boundary conditions along the flow direction. To ensure that the particles do not interact with their mirror images, we use a channel length of $L = 30a + \Delta z_0$, where Δz_0 is the initial axial spacing. In this chapter we concentrate on particles with a radius $a/w = 0.4$. We call the particle ahead in the flow *leading* particle which is followed by the *lagging* particle. The initial configuration is given by the lateral position of both particles $x_{\text{lead/lag},0}$ and the axial distance Δz_0.

4.2 Two particle trajectories

We begin our analysis by categorizing the different trajectories possible for this system. The types of trajectories depend on the initial lateral positions and the axial distance. Thus, we categorize them in a phase diagram for the starting lateral positions $x_{\text{lag},0}$ and $x_{\text{lead},0}$,
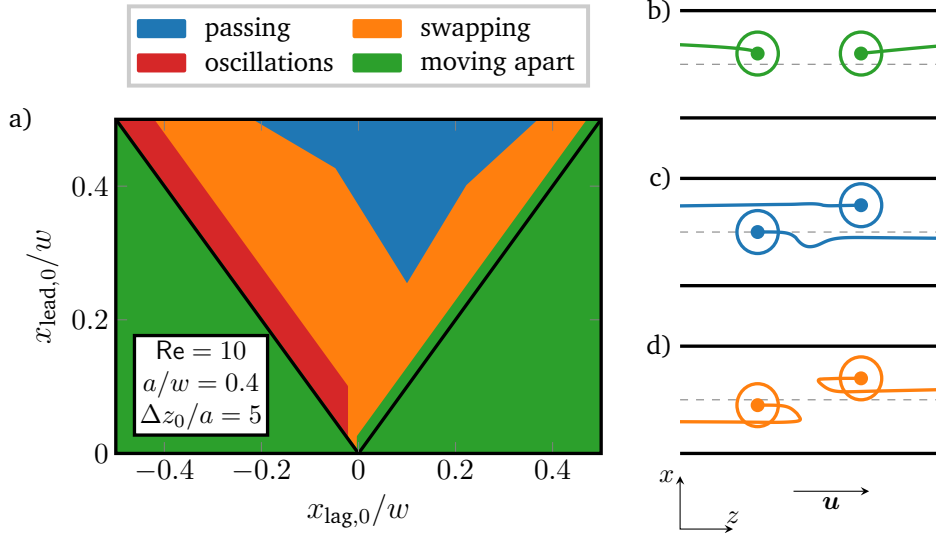
Figure 4.2: **(a)** Types of particle trajectories indicated in parameter space of starting lateral positions $x_{\text{lag},0}$ and $x_{\text{lead},0}$ for a pair of solid particles at Re = 10. The starting axial distance is $\Delta z_0/a = 5$ and particle radii are $a/w = 0.4$. The black lines indicate $|x_{\text{lag},0}| = |x_{\text{lead},0}|$. **(b-d)** Three exemplary trajectories for unbound moving-apart **(b)**, passing **(c)**, and swapping **(d)** states drawn in the center-of-mass frame. The dots indicate the initial conditions. The flow is directed along the z axis from left to right and the dashed line indicates the center of the channel.

while keeping the starting axial distance fixed at $\Delta z/a = 5$ [Fig. 4.2 (a)]. We identified four different kinds of coupled particle movements, which we term *moving apart*, *passing*, *swapping* and *damped oscillations* [Fig. 4.2 (b-d)].

We name the first three types of trajectories unbound as the particles drift apart and reach their equilibrium lateral positions at large axial distances, where they hardly influence each other anymore. In the next chapter, we find that particles which end up on different sides of the channel move together eventually. However, this contraction does not depend on different lateral positions and happens on timescales much larger compared to the trajectories discussed here. We also observe bound trajectories, where the two particles perform damped oscillations about their equilibrium lateral positions (Fig. 4.3). These trajectories occur in the narrow red region in Fig. 4.2 (left), where the particles occupy opposing channel sides and the lagging particle is initially slightly faster than the leading particle. We now analyze these trajectories in more detail and start by describing the unbound trajectories.

4.2.1 Unbound trajectories

For the unbound trajectories no stable pair configurations exists [green, blue, and orange patches in Fig. 4.2 (a), example trajectories are shown in Fig. 4.2 (b-d)]. In the *moving apart* trajectories (green patch with $|x_{\text{lead},0}| \geq |x_{\text{lag},0}|$), the leading particle is faster than

the lagging one. The distance between both simply increases, and they independently migrate toward their equilibrium positions due to inertial focusing, as given by the single-particle lift force profile. Even when the particles start from the same initial lateral position in the same half of the channel, they do not keep their distance fixed but follow a moving-apart trajectory [green line in Fig. 4.2 (b)]. The reason for this is an asymmetry in the lift force profile, which pushes the leading particle closer to the center and the lagging particle closer to the walls. We discuss the lift forces in more detail in Sec. 4.3. The different lateral movement of the two particles causes a non-zero relative velocity and the particles move apart. Finally, in the narrow green stripe with $x_{\text{lead},0} > x_{\text{lag},0} > 0$ [see Fig. 4.2 (a)], the particles initially approach each other. However, the lagging particle also drifts toward the wall so that it becomes slower than the leading particle, and they both just move apart. The fact that the particle move apart even when they start on the same lateral position contradicts the current opinion of the stability of same-streamline pairs [42, 46, 145]. We discuss this in detail in Sec. 4.3.1 and 5.3.1.

Passing trajectories occur when the lagging particle is closer to the channel center and therefore much faster than the leading particle. This allows the initially lagging particle to pass the leading one, and both particles change their order in the axial direction [blue line in Fig. 4.2 (c)]. During this overtaking, the displacement of the two particles is asymmetric. The particle closer to the channel center is displaced strongly while the trajectory of the leading particle is hardly affected. Furthermore, the passing particle does not return toward its initial condition as it is the case in the Stokes regime [141]. After the passing the axial distance increases and the particles assume their single-particle positions due to inertial focusing. We note that the particles do touch during the overtaking as we did not implement any lubrication approximation. However, due to our event-based integration method, they do not overlap (*cf.* Sec. 3.4.3).

When moving on swapping trajectories [orange line in Fig. 4.2 (d)], the lagging particle, though moving faster, does not succeed in overtaking the leading particle. Instead, the particles come close to each other and then swap lateral position, which makes the leading particle the faster particle. During this process they keep their axial order. When the particles move apart, they have interchanged their distances to the channel center. For example, for the orange trajectories in Fig. 4.2 (d), one finds $|x_{\text{lead}}^{\text{after}}| \approx |x_{\text{lag}}^{\text{before}}|$ and *vice versa*. Similar trajectories in linear shear flow are called reversing trajectories [146].

In general, we see similar types of trajectories also at low Reynolds numbers [141], indicating that the trajectories are governed by the viscous particle coupling and the Poiseuille flow profile. The fluid inertia results in an additional lift force which focuses the particles onto their lateral equilibrium positions. Although the two-particle trajectories studied in this chapter are often unbound we find that they are relevant for the understanding of particle trains as we discuss in the next chapter (*cf.* Ch. 5).

4.2.2 Damped oscillations

Besides the three unbound trajectories we find one type of bound trajectories. Figure 4.3 (a) illustrates such a damped oscillation in the center-of-mass frame of the particles. After
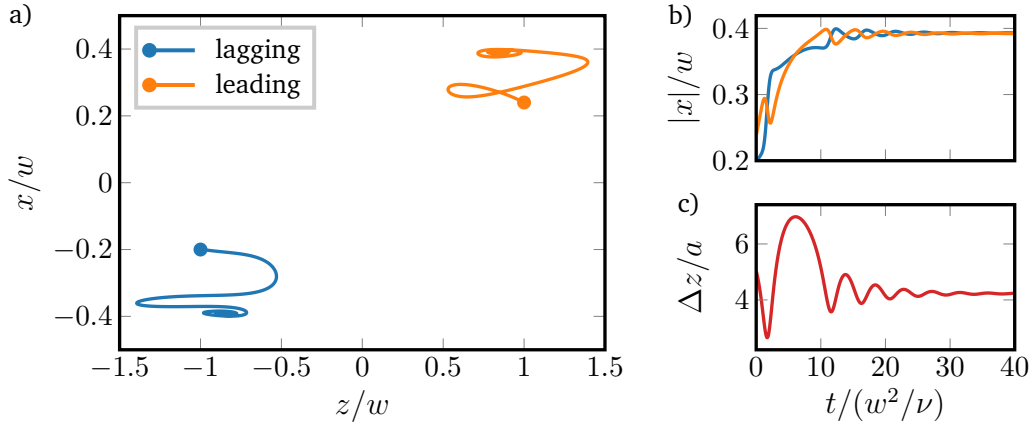
Figure 4.3: **(a)** Trajectories of both particles in the x-z-plane drawn in the center-of-mass frame. The initial position is indicated by a dot. **(b)** Distance $|x|$ of each particle to the channel center plotted as a function of time. **(c)** Axial distance $\Delta z/a$ of the particles versus time. The particles start with initial conditions $x_{\text{lag},0}/w = -0.2$, $x_{\text{lead}}/w = 0.24$, and $\Delta z_0/a = 5$ and the Reynolds number is Re $= 10$.

a short transient regime at the beginning, both particles migrate toward their stationary lateral positions ($|x_{\text{eq}}|/w \approx 0.4$), while performing damped oscillations (Fig. 4.3). This was also observed in experiments by Lee *et al.* [47]. The damping is the result of the inertial lift force which constantly focuses the particles onto their lateral equilibrium positions. This is supported by the observation of undamped oscillatory trajectories in pure Stokes flow [141]. A damped motion is not possible in Stokes flow as it would violate the kinetic reversibility of the Stokes equations (*cf.* Sec. 2.5.4).

Ultimately, the particles reach a cross-streamline equilibrium configuration. Their lateral positions agree with the positions of single particles. For the axial distance we find that all bound particle pairs performing damped oscillations assemble at an axial distance of $\Delta z/a \approx 4.1$ independent of their initial conditions (see Fig. 4.4). This value for the axial distance is in good agreement with experimental and theoretical results [40–42, 46].

In the following, we analyze how oscillation frequency Ω and damping rate γ behave as a function of the Reynolds number (Fig. 4.5). We determined $\Omega = 2\pi/\Delta T$ by measuring the time ΔT between maximal displacements (*cf.* Fig. 4.4) and γ by an exponential fit for the amplitudes decaying in time. For the oscillation frequency Ω [Fig. 4.5 (a)], we find a linear scaling with the Reynolds number, which indicates that the oscillations are due to the viscous coupling between the particles. In contrast, the damping rate scales quadratically with the Reynolds number [Fig. 4.5 (b)]. This can be easily understood as the damping is a consequence of the inertial lift force which shows the same scaling. Note that our findings on the damped oscillations are in full agreement with Hood and Roper [46].

The oscillation and the resulting formation of stable cross-streamline pairs was already explained by Humphry *et al.* [41]. The authors argue that a single rigid particle creates a viscous disturbance flow, which contains eddies or vortices on the opposite side of the channel. We also see these eddies in our simulated flow field, as indicated by the
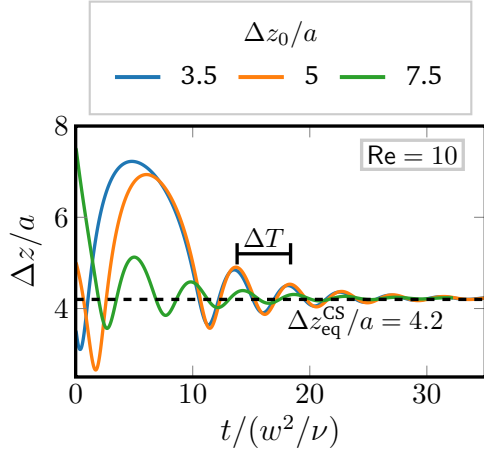
Figure 4.4: Oscillating pairs relax to the same axial distance independent of the initial axial spacing Δz_0 and lateral positions. We measure the time between the maximal displacements ΔT to calculate the frequency of the oscillation.

streamlines in the co-moving frame (Fig. 4.6). The second particle then occupies the center of an eddy, where it does not move relative to the first particle. Since the viscous disturbance flow is independent of Re, the position of the eddy does not change with Re.

While we fully agree with this explanation, we follow a different approach and describe at the formation of these stable configurations via the picture of lift force profiles presented in the following section (Sec. 4.3). The advantage of the lift force profiles is that they unambiguously show whether equilibrium positions are stable fixed points and at the same time determine the full dynamics of a particle pair.

We explain the formation of stable particle pairs by a stable fixed point, where the lift forces acting on the particles become zero and where both particles have the same distance from the channel center so that they drift with the same velocity. We will now determine the two-particle lift force profiles and later relate them to the damped oscillations.
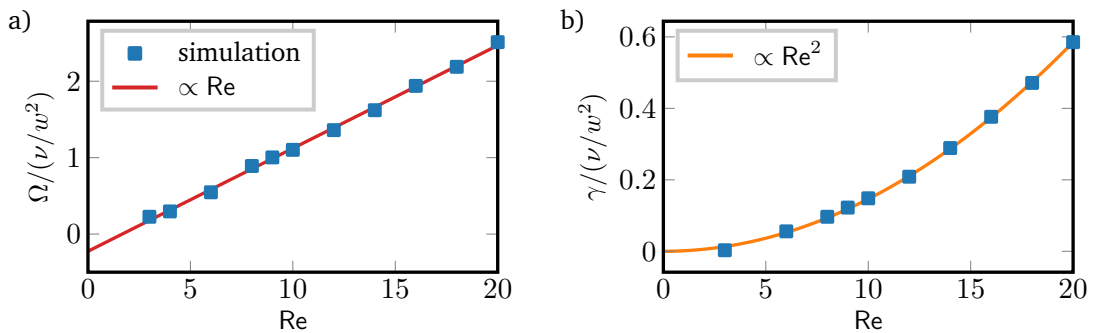

Figure 4.5: Oscillation frequency Ω **(a)** and damping rate γ **(b)** of the particle–particle distance plotted versus Re. The initial conditions are $x_{\text{lag},0}/w = -0.2$, $x_{\text{lead},0}/w = 0.24$, and $\Delta z_0/a = 5$. Linear and quadratic fits in Re are indicated, respectively.
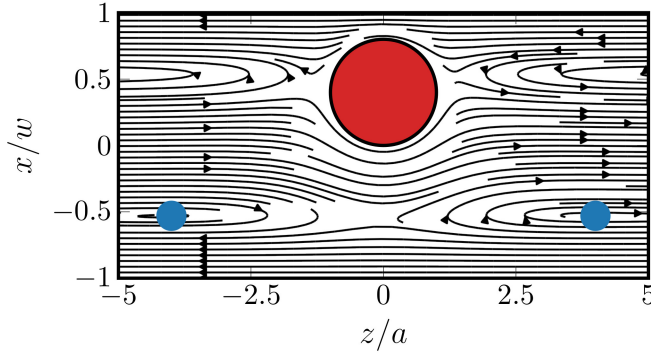
Figure 4.6: Streamline in the co-moving frame for a single particle (red) at Re $= 20$. An eddy forms on the opposite side of the channel (blue). The base flow is directed to the right.

4.3 Lift force profiles

The two-particle lift force profiles quantify the forces that each particle experiences in the presence of the other particle either leading or lagging in flow. Zero forces correspond to fixed points or equilibrium positions in the channel cross section and the magnitude of the force indicates how fast the particles are focused on their equilibrium positions. When both particles are mirrored at the channel axis, the lift force reverses sign. More importantly, when the flow direction is reversed the leading particle becomes the lagging particle. Due to the secondary flow in the inertial regime, the leading and lagging particles experience different flow fields which results in an asymmetry in the lift force profile. We have already observed this asymmetry in the discussion of the *moving apart* trajectory with the same initial lateral spacing (Sec. 4.2.1). There the leading particle was pushed inwards and the lagging particle moved outwards resulting in an increase of Δz.

In the following we determine how the two-particle lift force profiles change as a function of the axial particle distance Δz (measured along the flow direction), the lateral coordinates x_{lead} and x_{lag}, and the channel Reynolds number Re. In order to compare these profiles with the one of a single rigid particle, we recall the following two characteristics (see Fig. 4.7): For a single rigid particle one finds an unstable fixed point in the channel
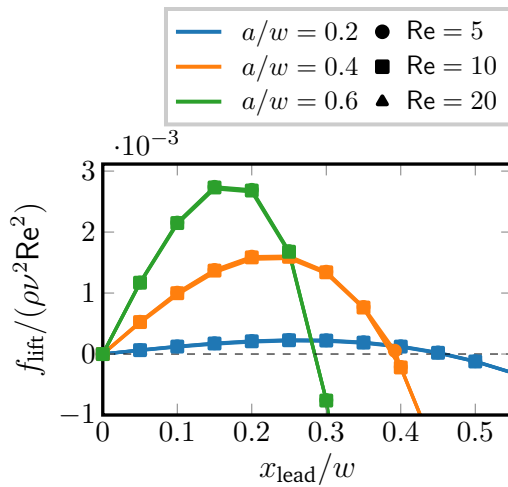

Figure 4.7: The lift force profile for a single particle depends on its radius a and the channel Reynolds number Re. Scaled with Re^2 the profiles for the same radius a (the symbols represent data points) fall on top of each other and are hardly distinguishable.
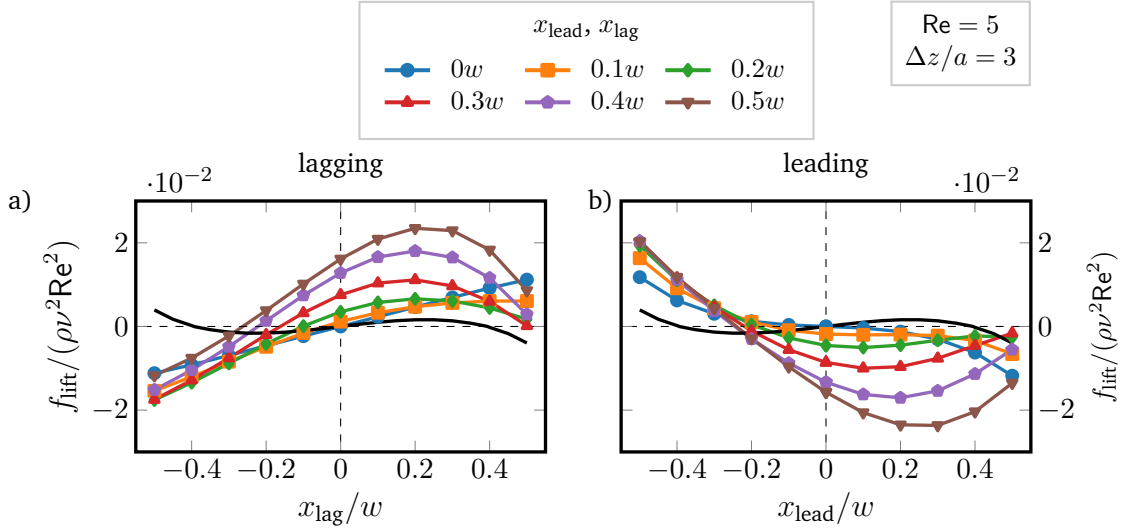
Figure 4.8: Lateral lift force profiles along the short axis for the lagging **(a)** and leading **(b)** particles for Re $= 5$, axial distance $\Delta z/a = 3$, and particle radius $a/w = 0.4$. The curve parameters are the positions of the leading **(a)** or lagging **(b)** particle, respectively. The black line corresponds to the single-particle force profile.

center, as well as stable off-centered fixed points along symmetry axes in the channel cross section. Furthermore, it is important to note that the force scales quadratically with the Reynolds number, which is also demonstrated in Fig. 4.7.

4.3.1 Parameter study

To determine the lift forces in our simulations, we fix the particles' lateral positions and measure the forces, which the fluid exerts on them. The lift forces are crucially influenced by the presence of the second particle, and we will illustrate how they depend on the axial particle distance Δz. The particles flow with different velocity along the channel axis depending on their positions in the channel cross section. So, when we measure the lift force profiles, we let the particles move with their center-of-mass velocity and keep Δz constant. This means that we effectively act with an axial force along the flow direction on each particle, resulting in small changes of the lift forces according to the Saffman effect [6] (*cf.* Sec. 3.5).

In Fig. 4.8, we demonstrate how the presence of another particle influences the lift force profiles and the equilibrium positions. We keep the axial distance of the particle pair fixed at $\Delta z = 3a$ and plot force profiles of the lagging particle for different lateral positions x_{lead} of the leading particle [Fig. 4.8 (a)] and *vice versa* [Fig. 4.8 (b)]. Overall, one recognizes that the profile is drastically influenced by an adjacent particle and lift forces generally are larger compared to the single-particle case. Thus, inertial focusing is enhanced.

For the leading particle [Fig. 4.8 (b)], we find only stable fixed points in the channel side
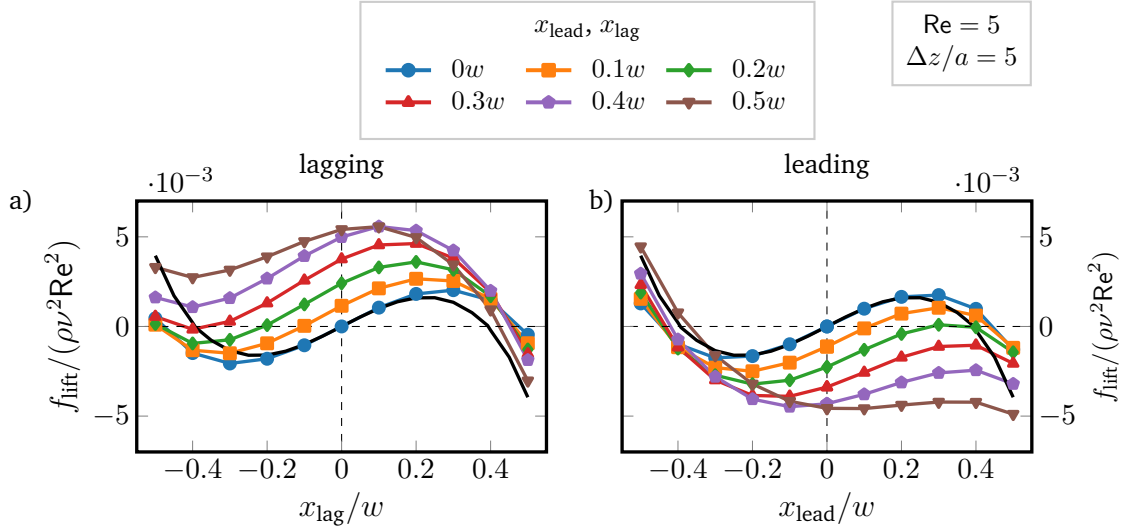
Figure 4.9: Lateral lift force profiles along the short axis for the lagging **(a)** and leading **(b)** particles for Re = 5, particle radius $a/w = 0.4$, and at the larger axial distance $\Delta z/a = 5$ compared to Fig. 4.8. The curve parameters are the positions of the leading **(a)** or lagging **(b)** particle, respectively. The black line corresponds to the single-particle force profile.

opposite to the location of the lagging particle, the other fixed points have disappeared. However, the new equilibrium positions are closer to the channel center compared to the single-particle case (black line) and, ultimately, for $x_{\text{lag}} = 0$, the stable fixed point is in the channel center. In contrast, when the leading particle resides in the upper half of the channel, the fixed point of the lagging particle in the other channel side [Fig. 4.8 (a)] becomes unstable and stable equilibrium points only exist close to the upper channel wall for sufficiently large x_{lead}. Interestingly, the configuration with $x_{\text{lead}} = x_{\text{lag}} = 0$ is not stable. Finally, note that the lift force profiles of the leading and lagging particles differ from each other due to secondary flow as stated in the beginning.

When we increase the distance Δz of the two particles along the flow direction, the lift force profiles are more similar in shape to the profile of a single particle, however the individual lines are shifted upwards (lagging particle) or downwards (leading particle) (Fig. 4.9). In particular, for the cases where the other particle is close to the channel center ($x/w < 0.3$), two stable equilibrium positions in the two respective sides of the channel are still present. In addition, when the second particle is in the channel center ($x/w = 0$), the force profile agrees with the single-particle case close to the channel center (blue lines in Fig. 4.9) but the stable equilibrium positions are located closer to the channel walls. Finally, by increasing the axial distance between the particle pair, the strength of the lift forces decreases compared to Fig. 4.8.

The existence of stable fixed points in the lateral force profiles of both particles does not necessarily define a stable particle configuration, since particles closer to the channel center move faster than particles near the channel walls. For a stable pair configuration,
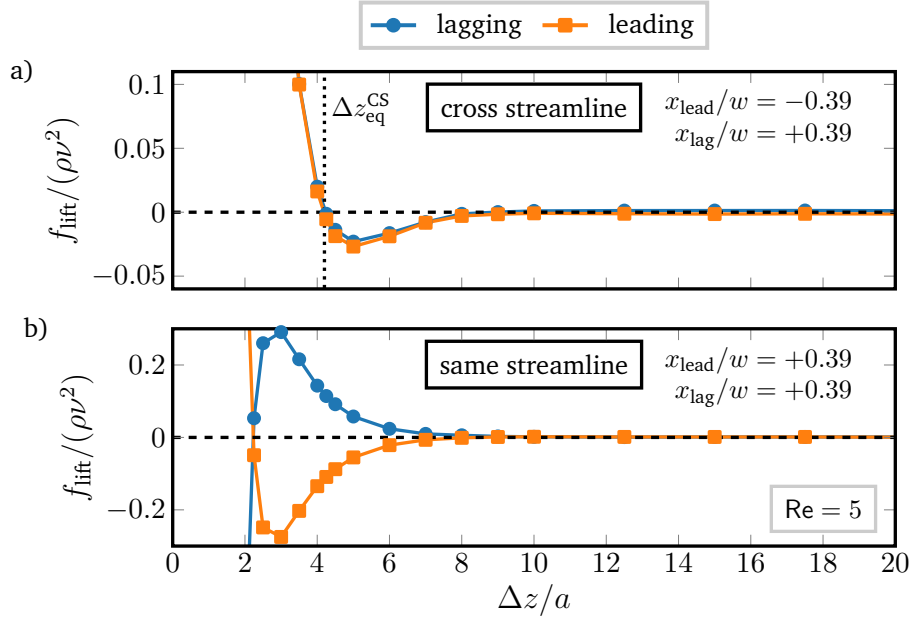
Figure 4.10: Lateral forces for a particle pair as a function of the axial distance Δz with both particles sitting at the single-particle equilibrium positions: **(a)** cross-streamline configuration with the leading and lagging particles at $x_{\text{lead}}/w = -0.39$ and $x_{\text{lag}}/w = 0.39$, respectively; **(b)** same-streamline configuration with $x_{\text{lead}}/w = x_{\text{lag}}/w = 0.39$.

the fixed points of both particles have to be at the same distance from the channel center. Strictly speaking, this does not have to be the case, as in the inertial regime, there is an asymmetry between the leading and lagging particles. However, we only find configurations where both particles assembled very close to the single-particle equilibrium position. From Fig. 4.9, we observe that an equilibrium position might be possible for $x_{\text{lag}}/w = -x_{\text{lead}}/w$ around 0.4, which is close to the final state of the damped oscillations discussed in Sec. 4.2.2. In contrast, when the particles are close together, for example at $\Delta z/a = 3$ as in Fig. 4.9, such a stable pair configuration is not possible.

In Fig. 4.10, we fix the lateral positions of both particles at the single-particle equilibrium position $|x_{\text{lead/lag}}|/w = 0.39$ and vary their axial distance. For stable configurations, the lift forces acting on both particles have to vanish. We analyze both pair configurations observed in experiments: same-streamline pairs and cross-streamline configuration. For the cross streamline configuration [Fig. 4.10 (a)], the lift forces indeed vanish at $\Delta z_{\text{eq}}^{\text{CS}}$. This fixed point is also stable since along the channel axis, it implies an effective repulsion for $\Delta z < \Delta z_{\text{eq}}^{\text{CS}}$ and an effective attraction for $\Delta z > \Delta z_{\text{eq}}^{\text{CS}}$, as the following argumentation shows. When the particles move closer together, the lift forces acting on both particles are positive. They push the leading particle with negative x_{lead} to the center, which thus moves faster, and the lagging particle with positive x_{lag} toward the walls, which thus slows down. As a result, the particle distance increases again. The same argumentation holds when the particles are moved apart. This demonstrates that the cross-streamline configurations are stable against small perturbations. The axial distance of $\Delta z/a \approx 4.2$ corresponds well

to the equilibrium distance for the damped oscillation discussed in Sec. 4.2.2 and with experimental values [41, 47].

However, we do not find stable configurations for the same-streamline case [Fig. 4.10 (b)]. Here, both particles are on the same side of the channels and their lift forces have opposite signs. A fixed point at a close distance $\Delta z/a = 0.225$ exists, but the same argumentation as before reveals that it is unstable against perturbations. This appears to be a contradiction to what is found in experiments, where same-streamline particle trains and pairs where observed [41, 42]. Typically, experiments report that same-streamline pairs assemble at a spacing about twice the equilibrium spacing of cross-streamline pairs [41, 42, 145]. Indeed, we expect to see same-streamline pairs with a similar distance in our simulations when we initialize them at an axial spacing $\Delta z/a < 8$ (*cf.* Sec. 5.3.1). However, our results indicate that same-streamline pairs are only one-sided stable. When the particles are squeezed together, they relax again to $\Delta z/a \approx 10$ but when they are pushed apart, the particles do not contract again. Such an increase of the axial distance was also observed by Lee *et al.*, when a particle train passes through an expansion-contraction channel geometry [47]. In the next chapter we show that our simulations almost exactly reproduce the statistics for the axial pair spacing in Ref. [47].

Recently, the results of an oscillatory flow field in an inertial microfluidic device have been published [145]. In this channel the flow velocity was periodically reversed in order to create a virtually infinite channel for Reynolds numbers Re $= 1 - 5$. The authors report a weakly attractive regime for same-streamline pairs in the range of $7.4 < \Delta z/a < 14$ where the particle slowly approach each other. However, the authors measure a relative velocity close to zero with error-bars covering both attractive and repulsive regimes. At the same axial distance we observe that the lift forces almost vanish for $\Delta z/a > 10$, and the particles move independently of each other [Fig. 4.10 (b)]. Finally, some studies observe that the axial distance depends on the particle Reynolds number [42, 43]. In particular, Kahkeshani *et al.* report, that the same-streamline axial distance decreases to about half the spacing at larger particle Reynolds numbers (Re > 50) [42]. We carefully checked different channel aspect ratios and mesh resolutions but the particle always assembled at an axial spacing round $8 - 10a$. A possible source of error might be the immersed boundary method, which we use to implement the flowing particle. However, the results in Ref. [147], for example, show that this method captures the principal behavior of solid particles in laminar flow. Furthermore, the otherwise good agreement with the experimental findings makes us confident that the results presented here capture the dominant effects.

4.3.2 Scaling of the lift force with Reynolds number

We continue by analyzing the influence of the Reynolds number on the two-particle force profiles. Again, we plot the force profiles at an axial distance $\Delta z/a = 3$ as in Fig. 4.8 but now for Re $= 20$ instead of Re $= 5$ (see Fig. 4.11). We immediately recognize that in contrast to Fig. 4.8, the force profiles are similar in shape to the one-particle profile but shifted upwards (lagging particle) or downwards (leading particle) with increasing lateral distance. We saw a similar behavior in Fig. 4.9 for Re $= 5$ at the larger axial
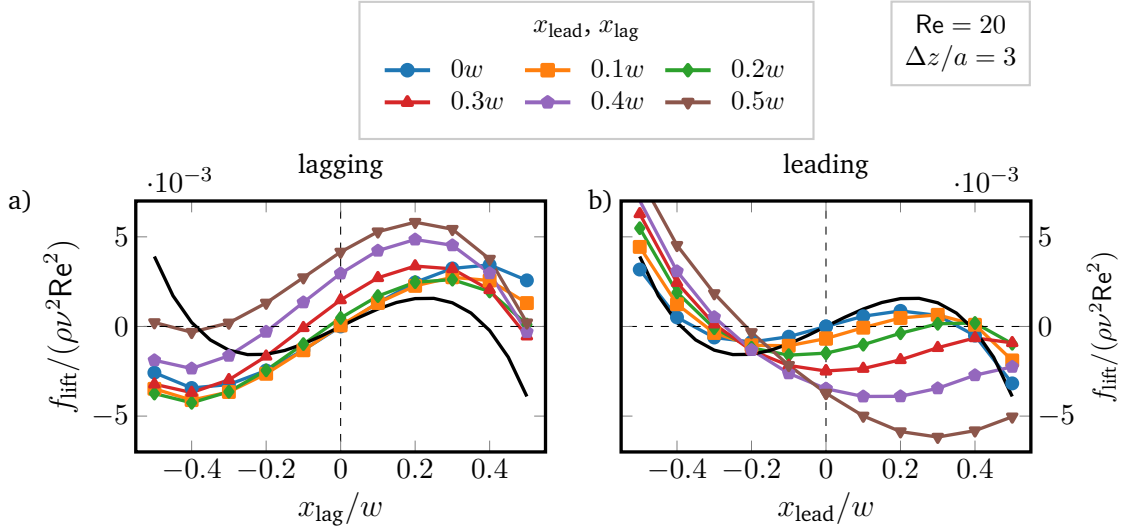
Figure 4.11: Lateral lift force profiles along the short axis for the lagging **(a)** and leading **(b)** particles for Re = 20, $\Delta z/a = 3$, and $a/w = 0.4$. The curve parameters are the positions of the leading **(a)** or lagging **(b)** particle, respectively. The black lines correspond to the single-particle force profile.

distance $\Delta z/a = 5$. In both cases, the strength of the lift forces is similar to that of the single-particle forces, while in Fig. 4.8, the two-particle induced forces are considerably larger than the inertial forces on a single particle. In addition, the lift forces in Fig. 4.11 rescaled by $\rho \nu^2 \mathrm{Re}^2$ are smaller than in Fig. 4.8, which suggests that the usual scaling with Re^2 does not apply. We study this in more detail in the next paragraph.

We now take a closer look at how the lift force scales with the Reynolds number Re. We already realized that for small particle distances, the two-particle lift forces no longer scale with Re^2 as in the single-particle case. However, it is also clear that for large distances, this scaling has to be recovered since the influence of the two particles on each other strongly decreases. To analyze this aspect in more detail, we fix the leading particle at $x_{\mathrm{lead}}/w = 0.3$ and vary x_{lag}. We determine the maximum value of the magnitude of the lift force profile for the lagging particle and plot it versus Reynolds number for several particle distances.[1] Figure 4.12 (a) shows the results in double-logarithmic scale. One clearly recognizes a power-law scaling with exponent α: $f_{\mathrm{lift}}^{\mathrm{max}} \propto Re^{\alpha}$. When we plot α versus Δz for both the leading and lagging particles, we find $\alpha = 2$ for $\Delta z/a > 7$ [Fig. 4.12 (b)]. When the particles approach each other, the scaling exponent decreases to almost $\alpha = 1$ for $\Delta z = 3a$. This scaling helps to further understand the character of the lift force, in particular, when two particles interact. A particle disturbs the fluid flow, which then influences the motion of nearby particles through a viscous coupling. This is the dominant contribution to the lift force at small distances, as indicated by the linear scaling of the lift force with Re. The inertial contribution takes over at large distances,

---

[1]In concreto, we consider the maximum value of $|f_{\mathrm{lift}}|$ within $|x|/w < 0.4$ to ignore wall effects.
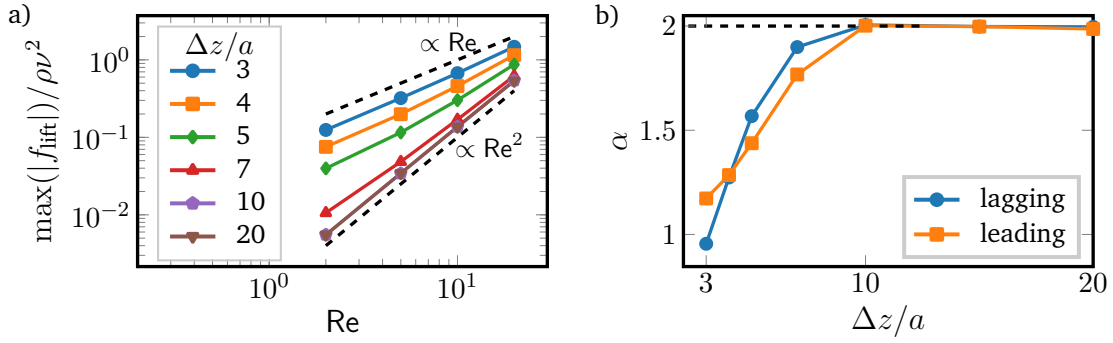
Figure 4.12: **(a)** Maximum value of the lift force of the lagging particle plotted versus Re for different axial distance Δz. The leading particle is fixed at $x_{\text{lead}}/w = 0.3$ while x_{lag} is varied. The particle radius is $a/w = 0.4$. The dashed lines indicate scaling laws: $\propto$ Re and $\propto$ Re^2. **(b)** Scaling exponent α from $f_{\text{lift}}^{\text{max}} \propto Re^\alpha$ plotted versus Δz for both particles. For both graphs the leading particle is fixed at $x_{\text{lead}}/w = 0.3$, while the position of the lagging particle is varied.

where the disturbance flow from the neighboring particle is weak, and one recovers the typical scaling for the inertial lift force, $f_{\text{lift}} \propto$ Re^2. So, our analysis confirms the picture of Ref. [47], which explicitly speaks about viscous disturbance flow. To sum up, both Fig. 4.10 and 4.12 indicate that beyond the distance $\Delta z/a \approx 7$, the particles do hardly interact. In Ref. [148], it is argued that hydrodynamic interactions in a microchannel are screened for distances larger than the width of the channel cross section. In our case, taking a particle radius of $a = 0.4w$, a distance of $7a$ corresponds to $2.8w$, which is close to the channel width of $2w$. This explains the rapidly decreasing influence of the second particle on the lift force.

4.3.3 Contour plots

In Sec. 4.2 we analyzed possible trajectories for a pair of solid particles moving under the influence of the lateral lift forces. To understand these trajectories, it is instructive to use a two-dimensional representation of the respective lift force profiles of the leading and lagging particle [see Fig. 4.13 (c-e)]. In this representation the asymmetry between the force profiles of the leading and lagging particle becomes obvious. The white lines indicate zero crossings of the lift force, which represent stable and unstable equilibrium points. The dynamics of the oscillating particle pair, which we discussed in Sec. 4.2.2, can be nicely illustrated using lift force contour plots.

These contour plots are obtained similarly to the force profiles which we discussed previously while for the trajectory the particles move without constraints. We start with the initial conditions

$$x_{\text{lag},0}/w = -0.2, \ x_{\text{lead},0}/w = 0.24, \ \text{and} \ \Delta z_0/a = 5 \,.$$

In the following we analyze how the lift force profile changes along the trajectory (Fig. 4.13). To facilitate direct comparison of the force profiles with the trajectories we plot
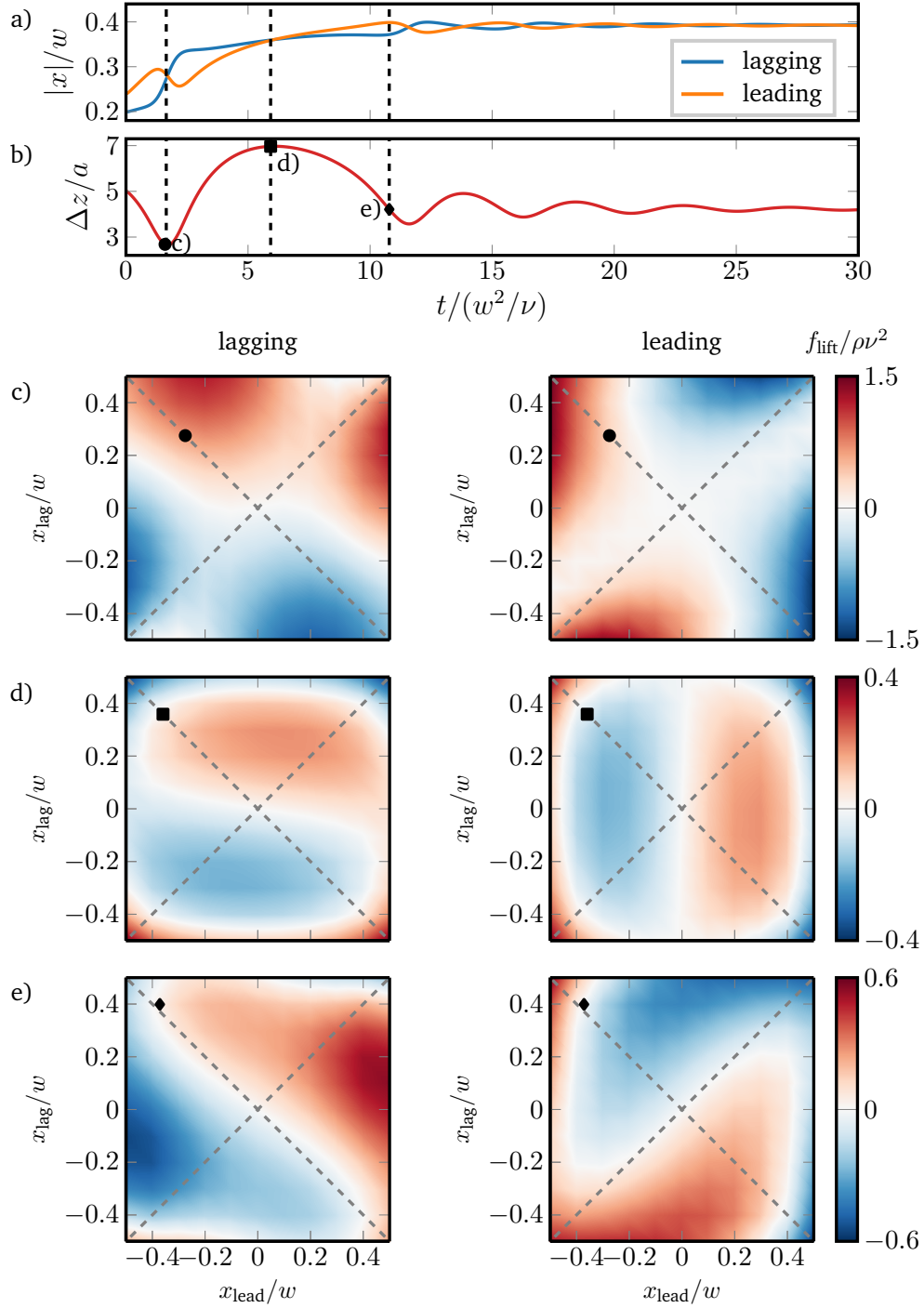
Figure 4.13: **Top:** Lateral **(a)** and axial distance **(b)** of an oscillating pair of particles as a function of time. **(c-e):** Snapshots of the lift force contour plot at different times during the oscillation. The left column shows the lift force acting on the lagging particle and the right column shows the force for the leading particle. The black marks indicate the lateral positions of the two particles. The gray dashed lines indicate line of same lateral distances ($|x_{\text{lead}}| = |x_{\text{lag}}|$).

again the lateral position (a) and the axial distance (b) already shown in Fig. 4.3. In the following we consider the force profile at three points in the trajectory: the minimum (c), the maximum (d) and the equilibrium axial distance (e). Overall, we observe that both particles migrate toward the walls until they reach their equilibrium position. However, this migration is not monotonously. As the lift force is non-symmetric and strongly depends on the axial distance, both particle experience forces of different strengths which also vary in time. This results in two alternating configurations where either the leading or the lagging particle moves faster compared to the other one, driving the oscillations of Δz.

Initially, the lagging particle is closer to the center of the channel and thus moves faster. Thus, the axial distance decreases significantly. This results in a strong lift force pushing the lagging particle toward the channel wall, while the leading particle is pushed toward the center for a short time (c). Now the leading particle is faster and the distance increases again. The resulting lift force is acting more strongly on the leading particle, while the lagging particle almost keeps its lateral spacing. At point (d) the leading particle is pushed further outside than the lagging particle and their distance decreases. During the oscillation the particles cross the equilibrium distance, *e.g.* at point (e). However, since at this point in time the lateral positions of the particles are still different, the oscillation does not end there. Finally, after a few oscillations, the particles reach their stable equilibrium positions, where the lift forces are zero.

4.4 Conclusions

Understanding pair interactions of two particles in inertial microfluidics is an important step for understanding collective dynamics such as the formation of particle trains. In this chapter we studied the trajectories and the lift force profiles of a pair of two rigid particles in an inertial channel flow.

We identified four types of particle trajectories depending on the initial lateral position of the leading and lagging particles. Three of them are unbound, where the particle distance increases after the initial approach until both particles reach their single-particle equilibrium positions independently. In the moving-apart trajectories the leading particle is faster than the lagging particle and the pair drifts apart. If the lagging particle is much faster, it overtakes and thereby changes axial order with the leading particle in what we called passing trajectories. On a swapping trajectory the lagging particle is only slightly faster. It approaches the leading particle, but then they exchange their lateral positions and move apart again.

Finally, bound trajectories occur for $x_{\text{lag}} \approx -x_{\text{lead}}$, where axial distance and lateral positions of the particles perform damped oscillations while reaching their equilibrium values. As such a damping can not occur in Stokes flow, it is clearly an inertial effect. Consequently, the damping rate scales with the Reynolds number squared, while the oscillation frequency is a linear function of Re. All bound trajectories approach the same axial distance of $\Delta z/a \approx 4.1$ independent of the initial conditions.

The two-particle lift force profiles of both particles are strongly influenced by their neighbors and depend on the particle distance along the channel axis. They clearly differ between the leading and lagging particles and the lift forces are stronger compared to a single particle. The increased lift force enhances particle focusing by driving them faster toward their equilibrium positions. At close distance the lift force profiles differ strongly from the profile of a single particle and do not allow for stable pair configurations. However, when increasing the axial distance or the channel Reynolds number, the profiles appear similar in shape but are shifted by constant forces. Interestingly, at small axial distances below $\Delta z/a = 4$ the strength of the lift forces scales with Re indicating that hydrodynamic interactions between the particles are dominated by viscous forces, while for distances $\Delta z/a = 10$ and larger scaling is quadratic in Re showing the importance of inertial forces. In between, the scaling follows Re^{α} with the exponent varying smoothly from 1 to 2 while increasing Δz. Finally, we presented the lift force profiles of leading and lagging particles in a two-dimensional representation as a function of both lateral particle positions. These two-dimensional plots determine the coupled dynamics and the trajectories of two floating particles.

We already mentioned the disagreement regarding the stability of the same-streamline pairs in our simulation results and other publications. To explain the observed typical distance of same-streamline pairs, the literature assumes an attractive interaction between the particles. Our results indicate, that there is only a repulsive interaction which almost vanishes at the observed distance and thus does not separate the particle further. In the next chapter we concentrate on the issue of stability of pairs. Additionally, we analyze the stability of larger particle trains and study how perturbations move through the train.

<div align="right">**5**</div>

Stability of pairs and trains

In this chapter we study the stability of multiple-particle structures of rigid spheres. In contrast to the previous chapter we focus more on the stability and initialize the particles already at their lateral equilibrium position but with a non-equilibrium axial spacing. First, we focus on a pair of flowing particles where we confirm the stability of cross-streamline pairs. In contrast, same-streamline pairs quickly expand to a characteristic separation but even at long times slowly drift apart. Adding more particles, we show that a staggered particle train contracts non-uniformly due to a collective drag reduction. For linear trains the drifting apart is slowed down compared to a same-streamline pair. Furthermore, it is non-uniform as the leading particles separate from the rest of the train. Finally, we present how a damped displacement pulse travels through a staggered train and how a defect strongly damps the propagation of the pulse. The chapter is based on the publication of Ref. [C], where these results are presented.

At higher densities particles do not only move to an equilibrium position in the channel cross section but also form regular trains along the channel axis [42, 47, 149]. This feature of inertial microfluidics is particularly useful for counting [24, 150, 151], sorting [27, 31, 33, 152], or manipulating cells [28, 30].

The particle trains were discussed in many works both in simulation [153, 154] and experiments [42, 43, 47]. However, literature is sometimes inconclusive in their explanations and observations. Thus, we dedicate the first section of this chapter a more detailed overview of the different observations.

Toward the end of the chapter we will also analyze how perturbations of the regular structure move through a staggered particle train. An initial particle displacement triggers a displacement pulse which travels through the staggered train while being damped. Due to the resemblance with acoustic phonons, such excitations are called microfluidic phonons [155]. So far, these phonons were only analyzed for flowing droplets squeezed between two parallel plates at vanishing Reynolds numbers [156, 157]. They provide an interesting model system with non-linear and non-equilibrium behavior [158]. In this quasi-two-dimensional geometry the interactions between the droplets are determined by dipolar interactions [155]. Studies on such phonons in inertial microfluidics do not
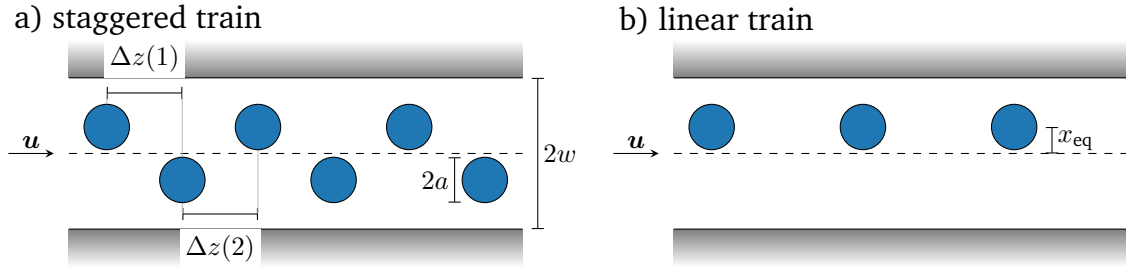
a) staggered train

b) linear train

Figure 5.1: Multi-particle trains in cross-streamline configuration **(a)** and same-streamline config-
uration **(b)**. x_{eq} gives the equilibrium distance from the channel centerline, Δz the
distance between two neighboring particles, and u indicates the flow direction.

exist. Due to the strong inertial damping such microfluidic phonons have to be triggered
from outside. Staggered particle trains are desired for applications since their regular and
dense order enhances particle throughput and at the same time facilitates particle sorting.
Understanding how staggered trains react on perturbations might open efficient ways to
crystallize them.

This chapter is strongly connected to the previous one where we focused on the lift force
profiles and the different types of possible trajectories of a pair of rigid particles. In the
following we study to what extent we can transfer the results of a pair to multi-particle
trains. Furthermore, we focus on their stability and the related particle dynamics. We
analyze the cross- and same-streamline pairs and extend the results to multi-particle
trains. In contrast to the previous chapter we initialize the particles already close to their
lateral single particle equilibrium position and focus on the dynamics of the axial spacing.
In the last part of this chapter we analyze how perturbations move through an inertial
microfluidic train. Due to the fluid inertia the dynamics of these inertial microfluidic
phonons behave differently than the microfluidic phonons observed in quasi-2D Stokes
flow. We will analyze how the phonons depend on the Reynolds number and on the
properties of the microfluidic train.

5.1 Summary of literature

The first experiments for particles in inertial microfluidics used cylindrical tubes, where
particles focus onto an annulus. In Ref. [40] Matas *et al.* studied particles with a low
confinement ratio (ratio of particle to cylinder radius between 0.03 and 0.05) and observed
particle trains above Re ≈ 100. With increasing Reynolds number more and more particles
assembled into trains. For channels with quadratic or rectangular cross sections, the
particles focus on one of the four or two possible equilibrium positions depending on the
aspect ratio of the cross section [37, 38, 54]. For such channels, typically, a mixture of
staggered and linear particle trains occurs [159]. In staggered trains the particle locations
alternate between both channel halves, whereas in linear trains all particles are located on
one side (see Fig. 5.1). For both structures experiments and simulations report a distinct

axial spacing, where the spacing for linear trains is about twice the spacing of staggered trains [42, 43, 47, 154].

Lee *et al.* explained the formation of particle trains by the combination of two effects: (i) inertial lift forces focus the particles onto their single-particle equilibrium positions and (ii) the viscous disturbance flow together with the imposed channel flow determine their axial separation [47]. In Ref. [41] the well-defined axial spacing of two particles in a cross-streamline pair is explained by the flow field around a single particle viewed in its center-of-mass frame. In their simulations two inward spiraling vortices on the opposite side of the channel form, located around 4 particle radii ahead and behind the particle. The second particle then follows the streamlines created by the first particle and spirals in damped oscillations toward its equilibrium position (*cf.* Sec. 4.2.2). This idea is also confirmed by analytical calculations [46]. From the perspective of the two particle lift force profiles the final configuration corresponds to stable fixed points where both particles move with the same velocity (*cf.* Sec. 4.3.1). Finally, two-dimensional simulations in Ref. [160] indicate that above Re $= 80$ particles in a staggered train perform stable oscillations about these equilibrium positions.

The stability of linear trains is less clear. Lattice-Boltzmann simulations performed by Kahkeshani *et al.* indicate that same-streamline pairs are stable [42], for which Ref. [46] provided an explanation based on the minimization of the kinetic energy of the fluid. However, early experiments [47] and most recent 2D simulations [154] report an increase of particle spacing over time in agreement with our own findings (*cf.* Ch. 4). Some experiments report that for increasing Reynolds number the axial spacing between the particles decreases [43, 153] even to the value of cross-streamline pairs [42]. However, other experiments report an increase of the spacing in linear trains with increasing Re [44]. In the range of Re ≈ 1 to 4 recent experiments observe that the spacing is independent of the flow velocity and that the smallest channel dimension determines the axial spacing between pairs [145]. Finally, simulations using a force coupling method report that trains are only stable up to lengths of 2 to 4 particles depending on the confinement ratio and the particle Reynolds number [153].

A comparison of the different experimental results is hampered since they use very different parameters, such as the confinement ratio a/w and channel Reynolds number. While experiments with smaller particles can go to higher channel Reynolds numbers with Re > 100 [40, 43], experiments with larger particles typically operate at channel Reynolds numbers between 1 and 20 [41, 47, 145]. As the particle Reynolds number is $\mathrm{Re}_p = (a/w)^2\mathrm{Re}$, both experiments and simulations can operate at the same particle Reynolds number although the other parameters are very different. This is especially relevant for Re ≈ 100, where the secondary flow around a single larger particle ($a/w = 0.4$) becomes so strong that it influences the particle-wall interactions [44]. A detailed review of the effect of particle size suggests that for a small confinement ratio $a/w \lesssim 0.1$ the particles move closer together with increasing Reynolds number [40, 43, 153] while for larger particles the separation seems to increase [44, 47].

Experiments are often limited by the channel length. Typical length-to-width ratios are $L/2w \approx 1000$. To overcome the limitation of the channel length, Dietsche *et al.* used an

oscillatory flow device which switched the direction of the flow such that the particles stayed in the channel and were not affected by the switching [145]. They confirmed the stability of cross-streamline pairs. For the same-streamline pair they identified a range of separations, $7.4 < \Delta z/a < 14$, where the particles moved together at low speed. However, the error bars were much larger than the measured speed values.

5.2 Microfluidic setup

Similar to the previous chapter we focus on particles with a radius $a/w = 0.4$ and rectangular channels with an aspect ratio $w/h = 0.5$ (*cf.* Fig. 4.1). We place N neutrally buoyant particle with radius a on the x-z-plane in the channel flow. The particles are initialized either in a staggered or a linear particle train (Fig. 5.1). If not stated otherwise, the particles are initialized on the equilibrium position of single particles on the x axis. The initial axial spacing Δz_0 of two neighboring particles in a staggered configuration differs from the equilibrium value Δz_{eq}^{CS} observed in the previous chapter. Same-streamline configurations are initialized with an axial spacing smaller than the limiting distance, we observe at long times. To analyze the stability of particle pairs and trains, the channel length is always chosen sufficiently long [at least $L \approx (N + 1) \cdot 10\,a$] to ensure that hydrodynamic interactions with images from the periodic boundary conditions along the channel were not relevant (*cf.* Fig. 4.10). When analyzing the microfluidic phonons, the channel length always was $L = N \cdot \Delta z$, so that we simulated an infinitely long particle train using periodic boundary conditions. In Sects. 5.3.1 and 5.3.2 we restrict ourselves to the Reynolds number Re = 20. In Sec. 5.4 we vary the Reynolds number between 5 and 100.

We now present our results starting with the stability of cross-streamline and same-streamline pairs, which we then extend to the same types of particle trains. Finally, we address microfluidic phonons concentrating on the damped propagation of a displacement pulse.

5.3 Stability of particle trains

5.3.1 Stability of cross- and same-streamline particle pairs

Before we consider multi-particle trains, we first analyze the long-time behavior and stability of a pair of rigid particles where both particles are initialized at their lateral single-particle equilibrium positions. We focus on the axial distance and look for stable axial configurations. We already analyzed the dynamics of a pair of particles. In the following, we focus on the case where both particles already occupy their equilibrium lateral positions. Thus, they stream with the same velocity.
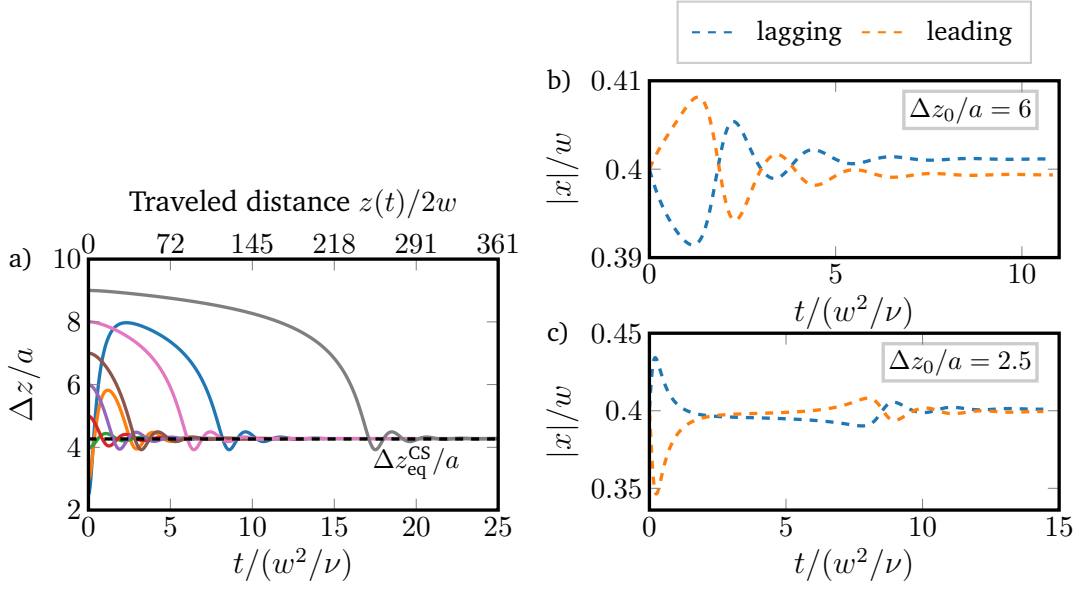
Figure 5.2: **(a)** Axial distance $\Delta z / a$ and **(b,c)** distance from the channel centerline $|x|/w$ as a function of time for particles in a cross-streamline configuration. Both particles are initialized at single-particle equilibrium positions, $x = \pm x_{\text{eq}}^{\text{single}}$, and different initial axial distances Δz_0 are chosen. In (a) the dashed line indicates the equilibrium axial distance $\Delta z_{\text{eq}}^{\text{CS}} / a \approx 4.2$ and the upper axis labels indicate the traveled distance of the center-of-mass of the pair along the channel for $\Delta z_0 / a = 8$. (b) Initial distance $\Delta z_0 = 6a > \Delta z_{\text{eq}}^{\text{CS}}$ and (c) $\Delta z_0 = 2.5a < \Delta z_{\text{eq}}^{\text{CS}}$.

5.3.1.1 Cross-streamline particle pairs

In Sec. 4.2.2 we found that particles in all analyzed bound trajectories reach the same cross-streamline configuration with an axial distance, $\Delta z_{\text{eq}}^{\text{CS}} = 4.2 \, a$, independent of the initial positions. In order to observe the damped oscillation, leading and lagging particles in flow were initialized with a similar lateral position $x_{\text{lag}} \approx -x_{\text{lead}}$. Here, we analyze the situation where both particles are initialized on the single-particle equilibrium positions at $\pm x_{\text{eq}} / w \approx \pm 0.4$ but with a distance $\Delta z_0 \neq \Delta z_{\text{eq}}^{\text{CS}}$. In Fig. 5.2 (a) we vary the initial distance Δz_0 from $2.5 \, a$ to $9 \, a$ and plot the respective time course of the axial distance. In all cases the particles reach $\Delta z_{\text{eq}}^{\text{CS}} \approx 4.2$, even when the initial axial distance is as large as $9 \, a$. In the graph the top axis indicates the traveled distance of the particle pair for $\Delta z_0 / a = 8$. This shows that the particle pair relaxes to its equilibrium configuration on distances much shorter than typical channel lengths of the order of $L/2w \approx 1000$ [43, 47].

In Fig. 5.2 (b,c) we show the time course of the lateral coordinates of the leading and lagging particles. When the initial axial distance Δz_0 is larger than the equilibrium value [Fig. 5.2 (b)], the lateral positions hardly change. However, the resulting relative axial velocity is sufficient to let them approach each other. Only when the particles are initialized closer to each other [Fig. 5.2 (c)], the lateral position change noticeably by *ca.* 10 %. This then initiates a rapid increase of the axial spacing due to the different flow velocities [blue line in Fig. 5.2 (a) with $\Delta z_0 / a = 2.5$] followed by a slow relaxation back to the equilibrium
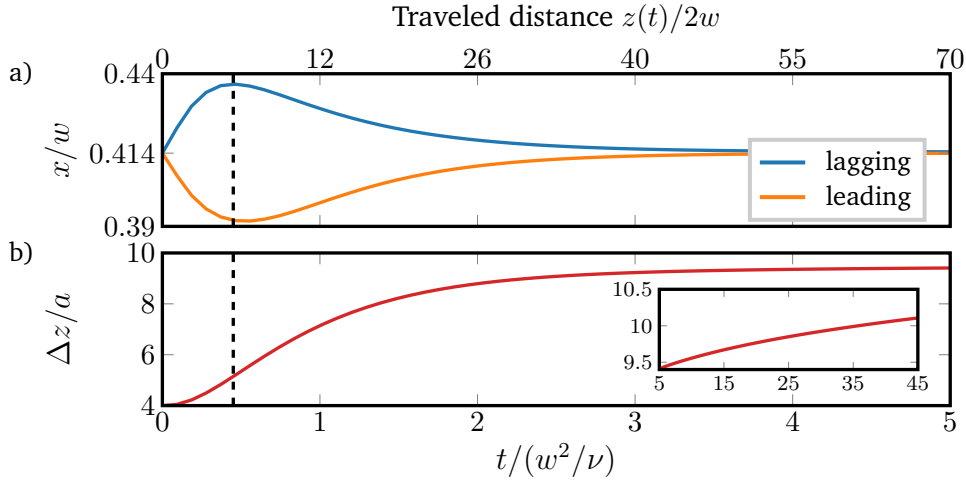
Figure 5.3: **(a)** Lateral positions and **(b)** axial distance as a function of time for a same-streamline particle pair. The dashed line localizes the maximum lateral displacement. Inset: At larger times still a slow but steady increase of Δz is observable. The upper axis indicates the traveled distance of the center-of-mass of the pair along the channel. At $t = 45w^2/\nu$ the particles have moved a distance of $z/2w = 650$.

value. We note that in the final configuration the leading particle is located slightly closer toward the channel center than the lagging particle but moves with the same velocity. The difference is smaller than a lattice unit. Our study shows that particle pairs relax toward their preferred distance even when starting at their lateral equilibrium positions.

5.3.1.2 Same-streamline particle pairs

In Sec. 4.2.1 we already observed that particles initialized on the same streamline with an initial distance of $\Delta z_0/a = 5$ slowly drift apart, even when positioned on the single-particle equilibrium position. We explained this behavior with an asymmetry in the two corresponding lift force profiles: the leading particle is pushed toward the channel center while the lagging particle is pushed toward the walls such that they move apart. This behavior does not change for larger Δz_0. Hence, our previous simulations indicate that same-streamline pairs are not stable.

We now analyze this behavior in more detail in Fig. 5.3. Again, we initialize the particles at the lateral equilibrium position and with an axial spacing equal to the axial distance $\Delta z_{\mathrm{eq}}^{\mathrm{CS}}$ of the cross-streamline pairs. The leading particle is noticeably and rapidly pushed toward the channel center while the lagging particle moves outwards [Fig. 5.3 (a)]. This drives the particles apart, which is visible by the rapid increase of the axial distance in Fig. 5.3 (b). Beyond $\Delta z/a \approx 5$, the particles slowly relax toward their equilibrium lateral position. However, even at large times, where both particles should move with the same speed, we still observe a slow but steady increase of the particle spacing [Fig. 5.3 (inset)]. In experiments such a drift might be difficult to measure. According to our simulations, beyond $t = 5w^2/\nu$ the distance Δz increases by only 6% while the particle pair travels a
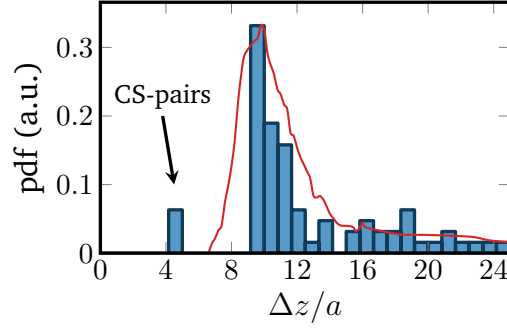
Figure 5.4: Histogram of particles distances for randomly initialized pairs after the center-of-mass has traveled a distance of $z/2w = 1000$. The small peak at $\Delta z/a = 4$ corresponds to cross-streamline pairs, which formed despite the fact that all particles were initialized on the same channel side. The red line shows data from experiments for pairs of particles with the same confinement ratio ($a/w = 0.4$) and the same traveled distance (2.5 cm) [47]. We rescaled the experimental data by a factor of 0.4 to match the height of the peak.

distance of $600 \times 2w$. This is of the order of channel lengths used in experiments. Taking typical values of $L = 5$ cm and $2w = 50\,\mu$m, we obtain $L/(2w) \approx 1000$ [43].

Experiments typically report a distance of about twice the equilibrium spacing of cross-streamline pairs [42], which would be $\Delta z/a \approx 8.4$ in our case. Our simulations indicate that the particles go to a larger spacing. In experiments the starting conditions are not as well-defined as in our case. To reproduce the experimental statistics for particle distances observed in Ref. [47], we initialize 76 different pair configurations, where both particles are randomly placed in the upper channel half with an initial distance $5a < \Delta z_0 < L/2$. In Fig. 5.4 we plot the distribution of particle distances after the particles have traveled a distance of $1000 \times 2w$, which is a typical value in experiments as mentioned above. The simulated distribution matches well with experiments for the same particle size with a peak at $\Delta z/a = 9.8$ [47]. The authors do not specify the channel Reynolds number explicitly, but the particle Reynolds number $\mathrm{Re}_p = \mathrm{Re}(a/w)^2 = 2.4$ is similar to the value of 3.2 used for this work.

To summarize, while we obtain good agreement with early experiments [47], we could neither identify an additional stable equilibrium distance for higher Reynolds numbers [42] nor reproduce an attractive interaction of particles in same-streamline pairs [145].

5.3.2 Stability of particle trains

Based on the insights we gathered from the behavior of particle pairs, we continue by analyzing multi-particle trains and begin with staggered particle trains.
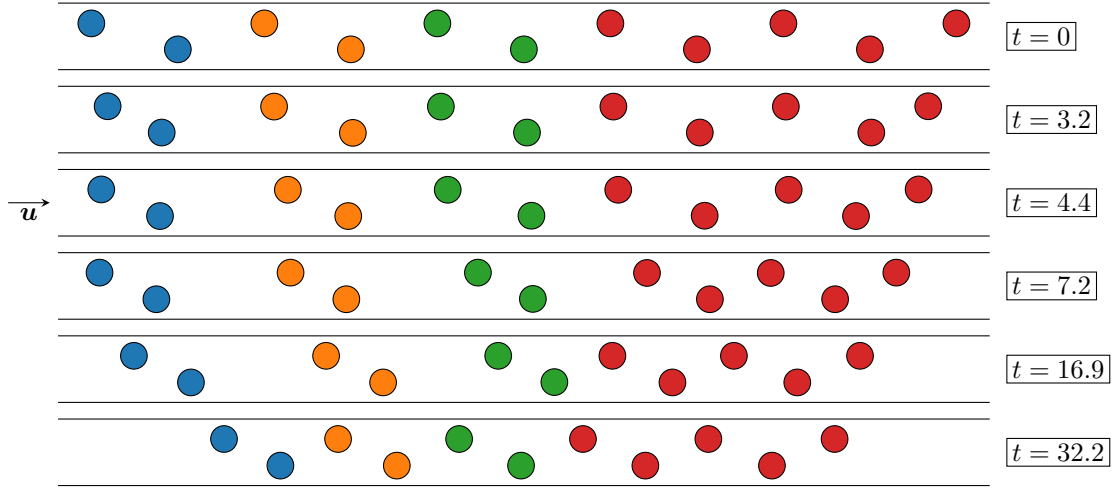
Figure 5.5: Snapshots of the contraction process of a staggered particle train at different times given in units of w^2/ν. At $t = 0$ all particles are initialized with a nearest-neighbor distance $\Delta z_0 = 6.5a = 1.5\Delta z_{\text{eq}}^{\text{CS}}$. The color of the trailing pairs corresponds to the lines in Fig. 5.6 (b).

5.3.2.1 Staggered particle trains

Concentration on the ideal case, we analyze how an expanded staggered particle train contracts toward its equilibrium configuration. For this we consider 11 particles, which we initialize on their single-particle position at $\pm x_{\text{eq}}$ with an axial distance of $\Delta z_0 = 6.5\,a \approx 1.5\Delta z_{\text{eq}}^{\text{CS}}$.

As expected from the analysis of the cross-streamline pairs, the axial distances between the particles decrease in time. However, as Figs. 5.5 and 5.6 (a) demonstrate, the contraction does not occur uniformly but rather through the formation of particle pairs. The contraction starts in the front and back of the train. We observe that initially only the leading and trailing pairs contract, whereby mainly the leading particle of the pair moves backwards toward the lagging particle [Fig. 5.5 ($t = 3.2$)]. While the pairs contract, they slow down. The leading pair stays connected to the staggered train but the last pair separates from the rest of the train due to its reduced velocity (see below). This triggers the contraction of the next pair and then a third pair so that at $t = 7.2$ three individual pairs in the back of the train exist. The contraction of these pairs always occurs in the same manner. In Fig. 5.6 (b) we plot their particle distances versus time and have shifted the curves by the time the previous pair needed to contract and separate. Then, all three curves fall onto each other.

The particle pair in the front of the staggered train also slows down. The next particle in line catches up so that a three-particle cluster exists at $t = 4.4$. This cluster slows down further and the next two particles can catch up. Ultimately, at $t = 7.2$ a contracted five-particle cluster exists followed by the 3 trailing pairs. The larger cluster slows down (see below) so that the three pairs can catch up one by one ($t = 16.9$) and, finally, at $t = 32.2$ the staggered train has reached its equilibrium configuration.
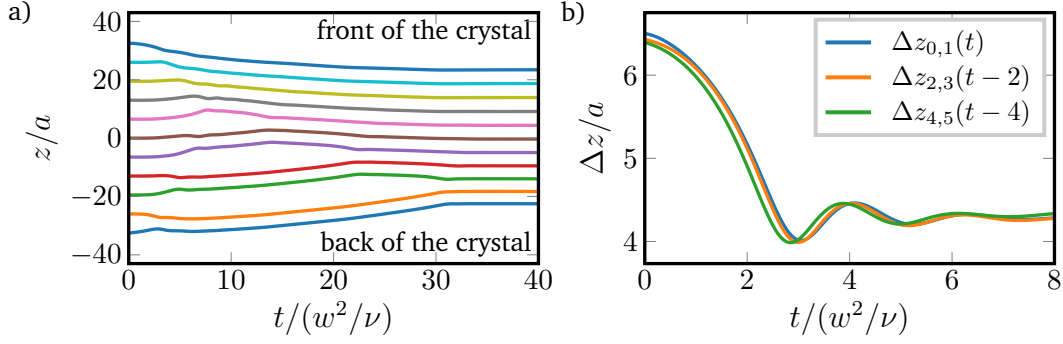
Figure 5.6: **(a)** Axial positions of all the particles in a staggered particle train as a function of time. The positions are given in the center-of-mass frame of the train. **(b)** Axial particle distances of the trailing particle pairs (*cf.* Fig. 5.5) as a function of time. The curves of the second and third pair are shifted such that they fall onto each other. The initial axial distance is $\Delta z_0 = 6.5 \approx 1.5 \Delta z_{eq}^{CS}$.

For the contraction of the particle train, two mechanisms are relevant. They are related to viscous drag reduction of clusters of particles compared to a single particle and when the clusters are more compact [158, 161, 162]. In our case, this means the resistance to an imposed Poiseuille flow is reduced and therefore the clusters slow down relative to the flow. Thus, a pair of particles slows down when the axial distance decreases and the center-of-mass velocity also decreases for larger staggered trains. We discuss this in detail in Fig. 5.7. In graph (a) we plot the center-of-mass velocity of a cross-streamline pair as a function of the axial particle distance. Although the decrease of the velocity with Δz is very small, it quantitatively agrees with the reported results of simulations for a pair of rigid particles ($a/w = 0.8$) moving on the centerline of a confined flow at Re $\ll 1$ [162]. In plot (b) we observe for staggered particle trains that the center-of-mass velocity monotonically decreases with increasing number of particles. For $N > 5$ this decrease is linear. The difference in velocities of a cluster consisting of 20 particles and a single particle is about 5 %. A similar dependency on the particle number was reported for simulations of a chain of particles driven by an applied force along a ring in a bulk fluid [161]. However, in this situation the variation of the velocity is more pronounced (around 50 %). The same type of collective drag reduction was also reported by Beatus *et al.* [155] for a linear chain of droplet disks in a quasi-2D flow. The authors named this observation the *peloton effect*, in analogy to the reduced drag of a group of closely riding cyclists.

We finish with a final observation. Figure 5.8 shows that the axial spacing of neighboring particles in a staggered train is non-uniform and increases toward the front of the train. For trains with more than nine particles the axial distance saturates at a value of $\Delta z/a = 4.8$, which is about 15 % larger than the distance of a single pair ($\Delta z_{eq}^{CS}/a = 4.2$). Finally, we observe that the distance of the leading pair is slightly reduced for trains consisting of seven particles or more.
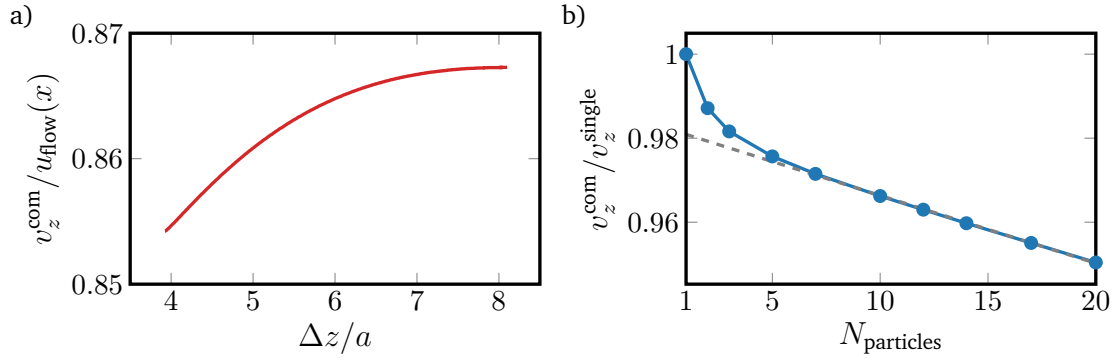
a)

b)

Figure 5.7: **(a)** Axial center-of-mass velocity for a cross-streamline pair as a function of the particle distance. The velocity is plotted in units of the fluid flow velocity at the lateral position of the particle pair. The data were extracted from the gray curve Fig. 5.2 (a), which starts at $\Delta z_0 = 9a$. **(b)** Axial center-of-mass velocity for a staggered particle train as function of the number of particles in the train. The velocity is plotted in units of the single-particle velocity. The gray dashed line is a linear fit for range with $N > 5$.

5.3.2.2 Linear particle trains

In the following we analyze the stability of linear particle trains and check if multi-particle interactions can stabilize the trains. For the individual same-streamline pairs we found that the axial distance of a same-streamline particle pair steadily increases in time (*cf.* Sec. 5.3.1). However, linear particle trains have been observed both in experiments [42, 43] and simulations [153] where they typically align with an axial particle spacing about twice the distance measured for staggered trains.

We initialize the particles in a linear train at the lateral equilibrium positions of single particles and choose an initial axial distance of $\Delta z_0/a = 4$ between neighboring particles. Figure 5.9 shows that the mean axial distance for linear trains of different sizes increases monotonically in time. However, while for $N = 2$ the axial distance hardly changes after reaching a distance of $\Delta z/a \approx 10$, the mean distance of trains with $N > 2$ increases visibly and the increase is slower for longer trains. The reason is that the expansion of the linear train is non-uniform. In Fig. 5.10 we show snapshots of a train with five particles at different times and plot the axial distance of neighboring particles. After an initial
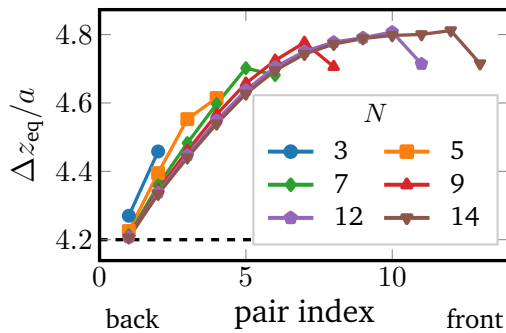

Figure 5.8: Axial equilibrium distance of neighboring particles in a staggered train as a function of the pair index, which increases from the back to the front of the train. The dashed line indicates the particle distance of a single pair, $\Delta z_{eq}^{CS}/a = 4.2$.
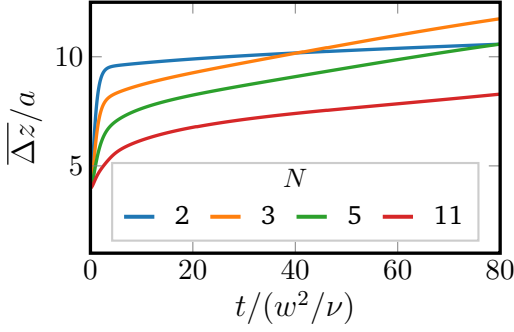
Figure 5.9: Mean axial particle distance as a function of time for linear trains with different numbers of particles.

fast expansion to $\Delta z/a \approx 8$, which is about twice the distance of a cross-streamline pair, always the leading particle is carried away by the imposed flow while the particle train behind it moves more slowly. This creates a particle train where the particle distance at one instant in time increases from the back (pair index 1) to the front (index 4). In our simulations all particles have traveled a distance of more than $1000w$ as the upper axis of the plot shows. Thus, the steady increase of Δz is very slow and it might not be possible to observe this in a typical experiment. However, our data show that the final configuration in the simulations is not a stable configuration.

The separation of the leading particle from the rest of the train was also reported in simulations by Gupta *et al.* [153]. They also mention stable trains up to a certain cluster size, an effect the authors name *conditional stability*. Their critical cluster size depends on the confinement ratio a/w and the particle Reynolds number. In their analysis the authors focused on confinement ratios $a/w = 0.08 - 0.14$, which is much smaller than in our work. However, their results indicate that for larger particles the critical cluster size reduces to $N = 2$.
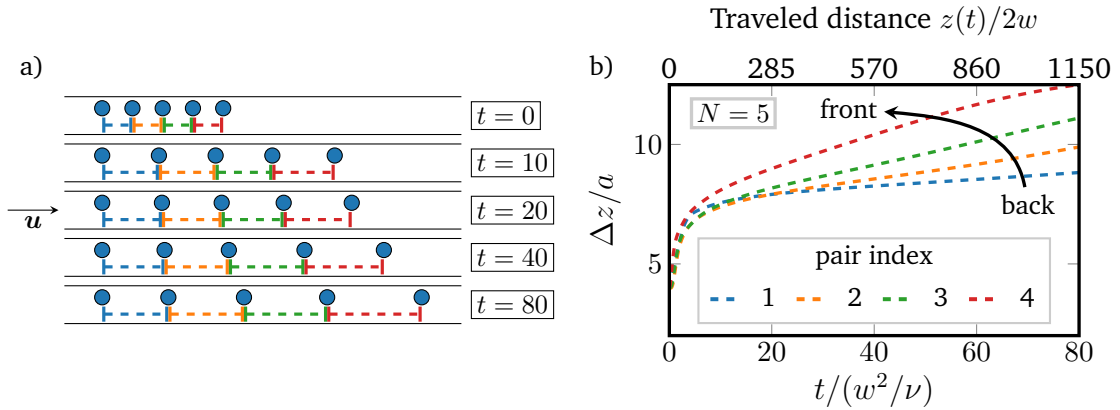

Figure 5.10: Expansion of a linear particle train consisting of 5 particles. **(a)** Snapshots at different times given in units of w^2/ν. At $t = 0$ all particles are initialized with the axial equilibrium distance of cross-streamline pairs. **(b)** Axial distance of neighboring particles as a function of time. From the back to the front the pairs are indexed by 1 to 4.
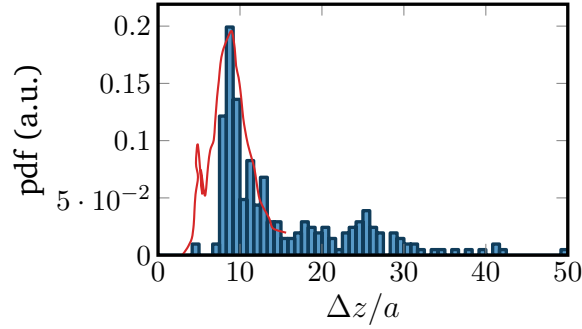
Figure 5.11: Histogram of particles distances for 4, 6, or 11 particles randomly initialized in the upper channel half after they have traveled at least a distance of $160w$ along the channel. The small peak at $\Delta z/a = 4$ corresponds to cross-streamline pairs, which formed despite the fact that all particles were initialized on the same channel side. The red line shows data from experiments by Kahkeshani *et al.* [42] for slightly smaller particles with $a/w = 0.34$. We rescaled the experimental data by a factor of 0.7 to match the height of the peak.

Finally, we calculate the statistics of the particle spacing in linear trains (Fig. 5.11). For this we randomly place 4, 6, or 11 particles in the upper channel half and ensure that there is no overlap between the particles. The channel length is chosen such that the volume fraction is fixed at $\varphi = 0.004$ as in Ref. [42]. After the particles traveled at least a distance of $160\,w$, we measure the distance to the nearest-neighbor particles. The recorded statistics shows good agreement with experimental data measured for slightly smaller particles with $a/w = 0.34$ compared to our particles with $a/w = 0.4$ (Fig. 5.11). Again, we observe a small peak at $\Delta z/a = 4.2$ which, in our case, corresponds to particles which move to the lower channel half.

5.3.2.3 Staggered particle train with defect

Besides the pure cross-streamline and same-streamline particle trains we also initialized a staggered train with a single defect. The results for the temporal evolution of the particle distances and some representative snapshots of the train are presented in Fig. 5.12.

To create a defect, the fourth and fifth particles are placed on the same channel side so that two staggered trains exist, which consist of four and five particles, respectively. The trains first contract individually while they drift apart from each other as the increasing distance of particle 4 and 5 indicates [red line in Fig. 5.12 (b)]. Only after the two trains have reached their equilibrium configuration, we observe that the lagging four-particle train catches up to the slightly slower train with five particles [see Fig. 5.7 (b)]. In the final state the particle distance of the defect is about twice the equilibrium particle distance of cross-streamline pairs similar to observations in [30, 159]. We note that this distance is not governed by any attractive interaction between the two particles but solely due to the fact that the larger leading train moves slower than the smaller trailing train. Indeed, when we swap the two trains such that the smaller one is leading, the two trains slowly drift apart in time.
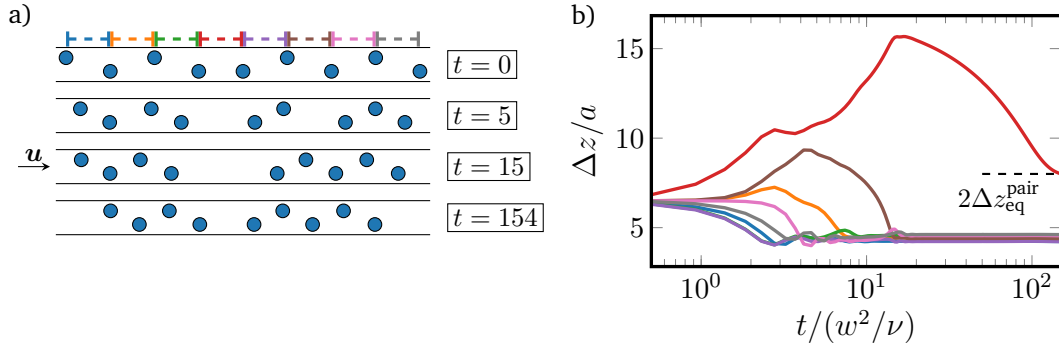
Figure 5.12: Staggered particle train with defect. **(a)** Snapshots at different times t of the non-uniform contraction from the initial ($t = 0$) toward the final ($t = 154$) configuration. **(b)** Distances between neighboring particles plotted versus time. The final particle distance of the defect is $2\Delta z_{\mathrm{eq}}$ as indicated by the dashed line.

5.4 Microfluidic phonons

Regular structures such as the staggered particle trains can be perturbed and thereby show propagating phononic excitations or microfluidic phonons. To study them in more detail, we analyze how a cross-streamline train reacts to a perturbation of a single particle position. We fit a train of 12 particles into a channel and adjust its length such that periodic boundary conditions generate an infinitely extended staggered train.

In Fig. 5.13 (a) we show the staggered train, where we initialized the 12 particles with an axial spacing of $\Delta z/a = 4.2$, which corresponds to the equilibrium distance of an isolated particle pair, and with lateral equilibrium positions at $\pm x_{\mathrm{eq}}/w = \pm 0.4$. To perturb the system, we move one particle inwards toward the channel center as indicated. Thus, it moves faster than the train and approaches the neighboring particle in front. Figure 5.13 (b) quantifies the reaction of all the particles by plotting their displacements $\Delta|x(t)| = |x(t)| - x_{\mathrm{eq}}$ from the equilibrium position where $\Delta|x| < 0$ means motion toward the channel center and $\Delta|x| > 0$ toward the channel wall. While approaching the neighboring particle, the first particle is pushed back to its equilibrium position and thereby pulls the neighboring particle from the opposite channel side toward the center. Thus, the whole process repeats such that a displacement pulse travels through the staggered train as illustrated by Fig. 5.13 (b). The particle motion is strongly damped since the inertial lift force pushes the particles back toward their equilibrium positions. The initially displaced particle (pink curve) overshoots by a small distance and then relaxes toward its equilibrium position. Also, the propagating displacement pulse is exponentially damped (dashed line in Fig. 5.13) with a damping rate γ, which we discuss in more detail further below. We observe that individual particles in a train return much faster to their equilibrium positions compared to isolated particles due to the coupling to neighboring particles, while the relaxation time of the whole pulse, γ^{-1}, is roughly twice as big. Below, we will also discuss in more detail the velocity of the displacement pulse.

The mechanism for the propagating displacement pulse can be explained as a sequence of
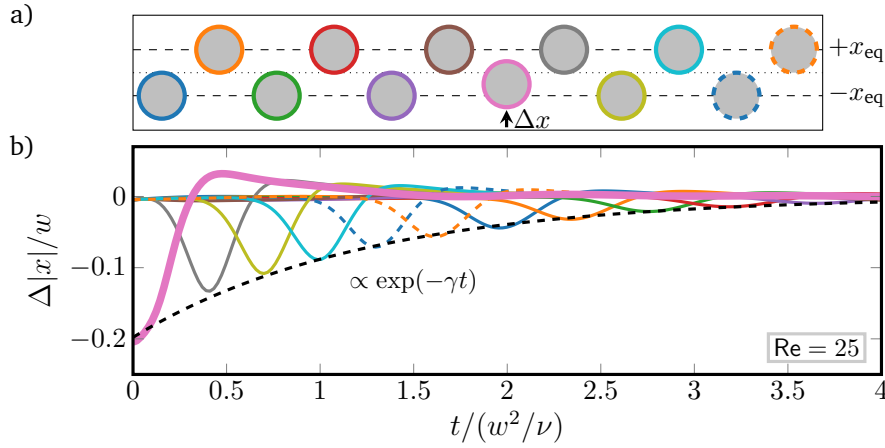
Figure 5.13: **(a)** Staggered particle train with an initial displacement of the seventh particle counted from the end (pink) and equilibrium axial particle distance is $\Delta z/a = 4.2$. **(b)** Lateral particle displacement from the equilibrium position, $\Delta|x(t)| = |x(t)| - x_{\text{eq}}$, plotted versus time for all the particles. The color coding is the same as in (a). Here $\Delta|x| < 0$ means motion toward the channel center and $\Delta|x| > 0$ toward the channel wall. The exponential decay of the pulse height with time is indicated (dashed line) and γ is damping rate. The Reynolds number is $\text{Re} = 25$.

swapping trajectories similar to the one we discussed in a previous chapter (*cf.* Sec. 4.2.1). As indicated in Fig. 5.14, the displaced particle approaches the next particle in line, and they swap their lateral positions such that $x_{\text{lead}}^{\text{after}} = -x_{\text{lag}}^{\text{before}}$ and *vice versa*. In principle, a propagating displacement pulse of the same type but without damping should also be possible in low-Reynolds-number flow, as swapping trajectories exist in this regime as well [141].

If the displacement brings the first particle close to or across the channel centerline such that $\Delta|x|/w \leq -0.4$, it becomes too fast and can no longer swap its position with the next particle. Instead, it moves through the staggered train (see Fig. 5.15) and leaves behind a defect, where two neighboring particles move on the same streamline. This is reminiscent of the passing trajectory for a particle pair identified in the previous chapter (*cf.* Sec. 4.2.1).
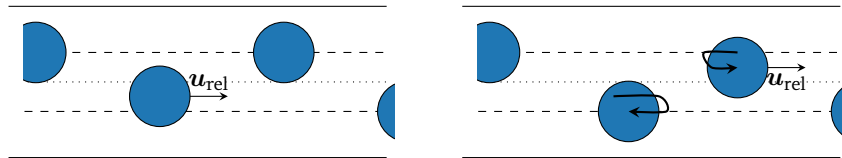

Figure 5.14: The swapping mechanism from the previous chapter explains how the displacement pulse is passed from the lagging to the leading particle. The curved arrows indicate the particle trajectories during swapping. The lateral equilibrium position of the particles and the channel center are marked by the dashed and dotted lines, respectively.
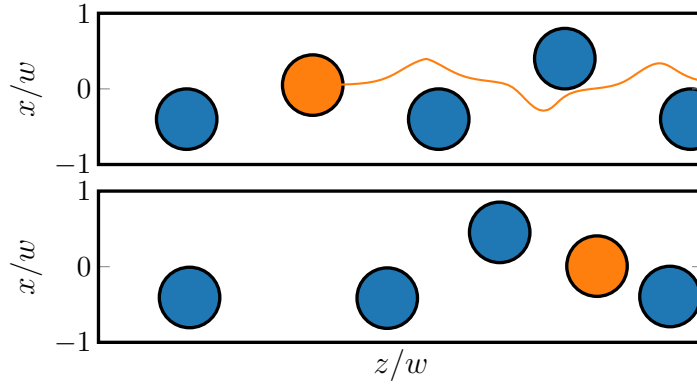
Figure 5.15: **Top:** Example of a passing trajectory in a staggered train when the initial lateral displacement from the equilibrium position is too large. **Bottom:** Snapshot after the particle has passed two of its neighbors.

5.4.1 Quantitative analysis of the displacement pulse

In Fig. 5.16 we plot the ratio of pulse velocity to train velocity $v_{\mathrm{pulse}}/v_{\mathrm{train}}$ and the damping rate γ of the displacement pulse as a function of the Reynolds number Re. This is similar to our analysis of the damped oscillations for a pair of rigid particles (*cf.* Sec. 4.2.2). The velocity ratio is roughly constant in Re so that we identify a linear dependence $v_{\mathrm{pulse}} \propto v_{\mathrm{train}} \propto$ Re, which makes sense since the fluid flow directly determines how fast displaced particles approach their neighbors. A similar scaling was observed for the oscillating frequency of a pair of rigid particles (Sec. 4.2.2). The pulse velocity is also larger than the train velocity since the displacement pulse is propagated by faster moving particles. For the damping rate γ of the displacement pulse we find good agreement with the damping rate of the oscillating particle pair in the regime of Re ≤ 20 [Fig. 5.16 (b)]. The γ values for the propagating pulse are slightly lower. The damping rate scales quadratically with Re, only for higher Reynolds numbers the scaling deviates slightly from
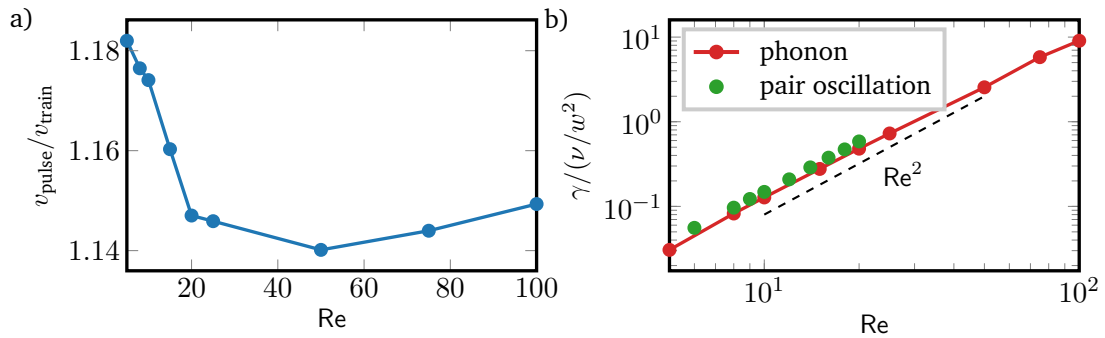

Figure 5.16: Ratio of pulse to train velocity **(a)** and damping rate γ **(b)** of the displacement pulse as a function of the Reynolds number. In all cases the initial axial spacing is $\Delta z_0/a \approx 4.2$ and the initial displacement is $\Delta |x|_0/w = -0.2$. For comparison, we also plot γ for an oscillating particle pair from the previous chapter.
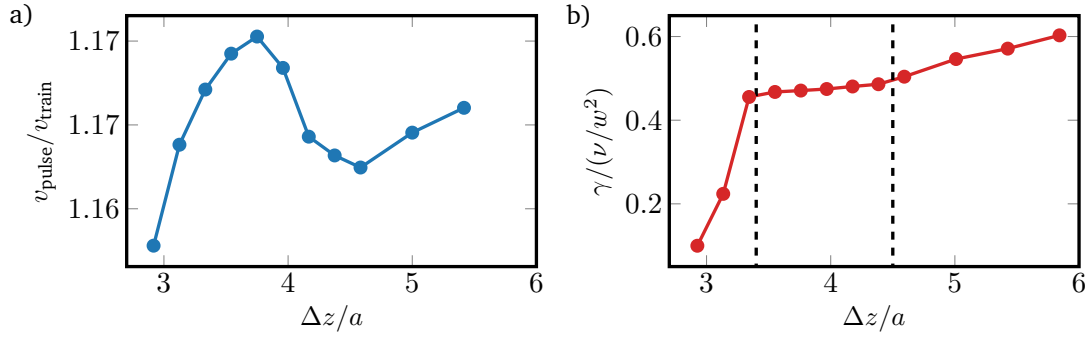
Figure 5.17: Ratio of pulse to train velocity **(a)** and damping rate γ **(b)** of the displacement pulse as a function of axial particle distance Δz. The other parameters are Re $= 20$ and $\Delta|x|_0/w = -0.2$. The dashed lines indicate a region with almost constant γ.

Re^2. Thus, damping of the propagating pulse is a clear inertial effect due to the acting inertial lift force and therefore the scaling with Re^2 is expected.

In our setting using periodic boundary conditions along the channel axis, we can compress or expand the infinitely extended particle train by changing the channel length. This allows to study pulse propagation under tension. A possible experimental realization are expanding or contracting channels, where the channel width changes abruptly. For example, in an expanding channel the particle spacing relaxes slowly to its larger distance [24, 47]. In Fig. 5.17 we show ratio of pulse to train velocity $v_{\text{pulse}}/v_{\text{train}}$ and the damping rate γ as a function of the axial particle distance Δz. The velocity ratio again is nearly constant with varying Δz, while the train velocity increases linearly with Δz due to the increased friction (not shown). For the damping rate we find three different regimes. When the staggered train is strongly compressed, the damping rate is strongly reduced, which is due to the strong repulsive interactions between particles. Additionally, we observe that the displacement pulse no longer travels in one direction only, rather it propagates in both directions at the same time. For axial distances around the equilibrium value ($3.5 < \Delta z/a < 4.5$) the damping rate is almost constant and it slightly increases for $\Delta z/a > 4.5$. Here, the regular train is not stable. Instead, the distances between two particles contract leaving larger gaps between particle pairs. Thus, the particles relax toward their equilibrium positions more like an individual particle, increasing the overall damping rate.

Finally, we also varied the initial displacement $\Delta|x|_0$ from the equilibrium position and plot in Fig. 5.18 ratio of pulse to train velocity $v_{\text{pulse}}/v_{\text{train}}$ and the damping rate γ. Positive $\Delta|x|_0$ means that the particle is moved toward the channel wall. Since it thereby slows down relative to the staggered train, it approaches the particle behind and the displacement pulse moves against the staggered train. For the velocity ratio this means $v_{\text{pulse}}/v_{\text{train}}$ jumps from a value larger than one to a value smaller than one when $\Delta|x|_0$ becomes positive, while the pulse velocity is relatively constant on both sides of the jump. The dependence of the damping rate is less intuitive. It is constant for large negative $\Delta|x|_0$, goes through a minimum and then increases linearly for increasing $\Delta|x|_0$ starting at $\Delta|x|_0 = -0.1$.
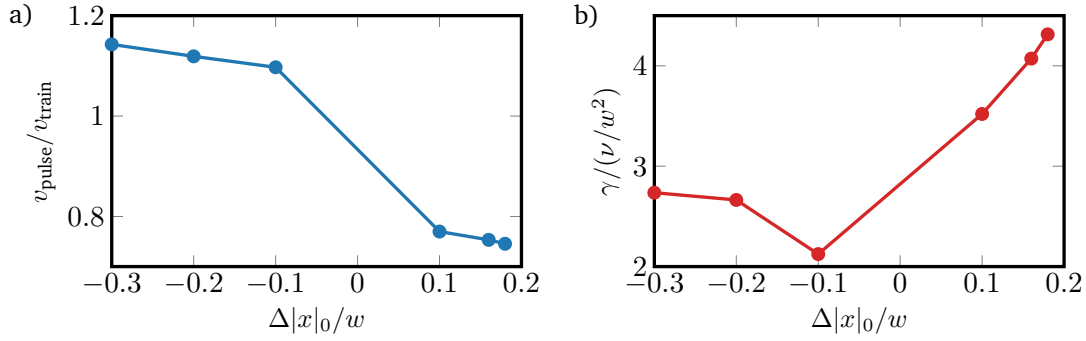
Figure 5.18: Ratio of pulse to train velocity **(a)** and damping rate γ **(b)** of the displacement pulse as a function of the initial displacement $\Delta|x|_0$. The other parameters are $\text{Re} = 20$ and $\Delta z/a = 4.2$.

5.4.2 Influence of a defect on the pulse propagation

Finally, we study how a defect in the staggered particle train strongly dampens the propagating pulse and show our results in Fig. 5.19. We reduce the number of particles to 11 and introduce a defect with two neighboring particles on the same streamline, as already investigated above. As illustrated in Fig. 5.19, the pulse is initiated at the fifth particle to the left of the defect. Up to the defect it propagates as before. However, having passed the defect it is strongly damped such that the pulse vanishes almost completely.

5.5 Conclusions

The axial alignment of particles in inertial microfluidic devices is an important feature for counting, manipulating, and sorting cells. Therefore, the stability of trains is a crucial ingredient for designing and understanding lab-on-a-chip devices. As the literature on this topic does not always agree with their findings, we focused on a detailed analysis for one specific set of parameters.

The stability of cross-streamline pairs is accepted in the literature. We showed that particles in such a pair attract each other over large distances while their lateral positions hardly change. A cross-streamline pair always contracts or expands to its equilibrium axial distance. For same-streamline pairs we thoroughly analyzed and thereby confirmed the result of the previous chapter that the same-streamline configuration does not have an equilibrium axial spacing. However, from smaller distances it quickly expands to a characteristic separation but even at long times very slowly drifts apart. Their dynamics is dominated by a repulsive interaction, which rapidly decays with increasing axial distance. Although our observations contradict the existence of stable same-streamline pairs [42, 46, 145], the distribution of axial distances agrees with experiments [47]. In particular, it has a well-defined peak at about twice the distance of cross-streamline pairs.

Then, we extended our analysis to particle trains with more than two particles and first analyzed how staggered trains relax to their equilibrium configurations. In particular,
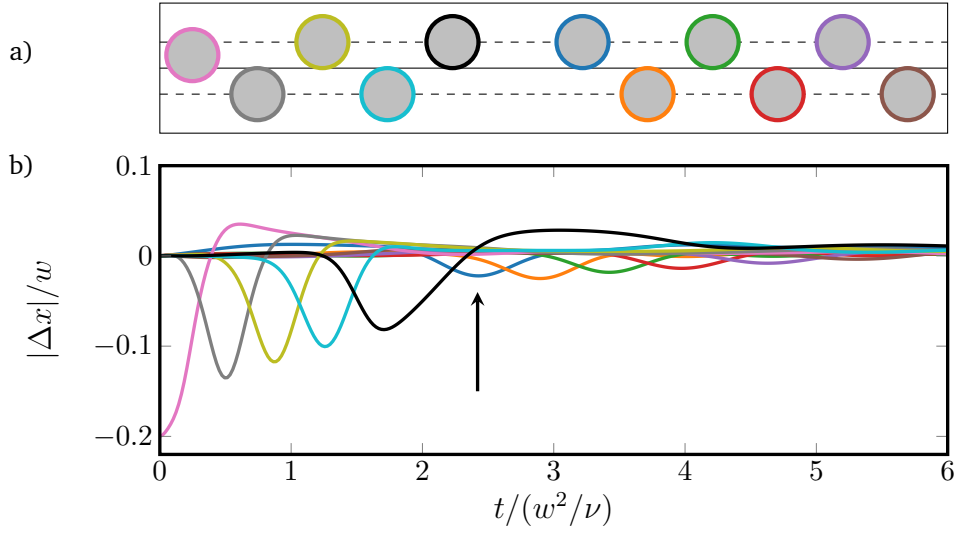
Figure 5.19: **(a)** Staggered particle train with a defect and an initial displacement of the first particle counted from the end (pink). The equilibrium axial particle distance is $\Delta z/a = 4.2$ and $\Delta z/a = 8.4$ between the defect particles. **(b)** Lateral particle displacement from the equilibrium position, $\Delta|x(t)| = |x(t)| - x_{\text{eq}}$, plotted versus time for all the particles in the upper and lower channel half. The color coding is the same as in (a). The arrow indicates the strongly damped displacement of the first particle after the defect has been passed.

a staggered train initialized with an axial particle spacing larger than the equilibrium distance contracts non-uniformly. The non-uniform contraction is related to two effects of collective drag reduction: (i) when two particles in a cross-streamline configuration approach each other they slow down since they exhibit less resistance to the driving Poiseuille flow and (ii) the center-of-mass velocity of staggered trains decreases the more particles are in the train (*peloton effect*). These two effects drive the non-uniform contraction in the back and front of a staggered train. While in the back trailing pairs of particles separate from the rest of the train, in the front the leading pair slows down and collects more and more particles. Only with time the pairs catch up with the particle train in front of them and form one large train. Finally, we found a master curve for the axial spacing within a staggered train. The spacing between the particles increases from the back to the front of the train and ultimately saturates for sufficiently long trains. So a staggered train is slightly expanded at the front relative to the back. In experiments a particle train slowly expands when it enters a channel with a suddenly expanding cross section [24, 47]. This could be a means to observe the scenario outlined here.

For linear trains we found a very similar behavior as for same-streamline pairs. Starting from a particle distance similar to the staggered train, the spacing relaxes in the beginning phase to a value close to experimental results [42] about twice the distance of cross-streamline pairs. Then, the particles continue to slowly drift apart non-uniformly. The leading particle moves the fastest and separates from the rest of the train. This confirms a similar observation reported by Gupta *et al.* for a smaller confinement ratio [153].

In addition, we were able to reproduce the statistics of particle distances observed in experiments [42].

Finally, we analyzed how a displacement pulse migrates as inertial microfluidic phonon through a staggered train. The displacement is transported from one particle to another via swapping trajectories, where the inertial lift forces damps the amplitude of the displacement pulse. When the initial displacement is too large, the displaced particle itself moves through the staggered train and leaves behind a defect. The ratio of pulse to train velocities is almost constant for varying Reynolds number and axial particle distance, whereas it is by ca. 30 % smaller for initial displacement toward the wall compared to perturbations toward the channel center. For the damping rate of the displacement pulse we confirm the quadratic scaling with the Reynolds number, which identifies damping as an inertial effect. The damping rate is almost constant for varying axial distance between the particles and thereby changing line density. Only when the particles are close together the damping rate is reduced. This is especially interesting when the line tension of staggered trains changes rapidly when entering sections of the channel with expanding or contracting cross sections [24, 47] since then the trains want to expand or contract.

6

Single deformable capsule

One fascinating application of lab-on-a-chip devices is the diagnoses of diseases based on mechanical properties of cells. The deformability of the capsule results in an additional lift force directed toward the channel center which is in parts compensated by the inertial lift force. While a deformable capsule is less complex than a real living cell, it allows us to get a deeper understanding of the relevant effects which determine the dynamics of single deformable particles in inertial microfluidics. We first analyze the equilibrium positions of a single deformable capsule in a microchannel with quadratic or rectangular cross section. We verify that the scaling of the lift force for a rigid particle also holds for a deformable capsule and analyze how the deformability influences the lift force scaling. We show, that the lift force for a deformable capsule is the sum of the inertial lift force of a rigid particle and the lift force derived for a deformable capsule without inertia. Finally, we use the Saffman effect to further control the equilibrium position of the capsule which should allow a finer separation of deformable capsules. The chapter is based on the publication of Ref. [A], where these results are presented.

Most applications of inertial microfluidics arise in the field of medical analysis. Due to its passive sorting capability with high throughput this technology might drastically reduce the cost for diagnosis. However, the deformability of cells yields an additional lift force which results in a migration of the capsule toward the channel center. This migration is also possible in the case of negligible fluid inertia as the deformable membrane breaks the kinematic reversibility of the Stokes equation. So far, deformable capsules were mostly studied in Stokes flow [49, 50, 163]. Only in recent years studies have been extended to the inertial regime [27, 164–168]. In particular, Hur *et al.* demonstrated with their experiments that particles can be separated from each other based on their elastic deformability [16] . Indeed, particles move closer to the channel center the softer and the larger they are. This effect was also studied in simulations [169, 170]. Although all results agree that soft particles move to the channel center, the influence of the Reynolds number is not completely clear. While in some cases the final equilibrium distance from the channel center seems to depend on the Reynolds number [36, 171], Kilimnik *et al.* found no evidence of such a behavior in their computer simulations [169]. In the following,

we analyze how this inwards directed deformability-induced migration compensates the outwards-directed inertial focusing.

6.1 Microfluidic setup

In the following analysis we focus on a single deformable particle in a microchannel with a quadratic cross-section. In Sec. 6.2.2 we vary the channel cross section to study the influence of the deformability on the equilibrium position. To ensure that the particle does not interact with its periodic images our simulations are conducted with a length-to-width ratio of $L/2w = 4$. For the deformable capsule we need a much higher resolutions compared to the rigid particles as the high shear rate induces defects in the mesh used to model the capsule. Hence, we choose 120 cubic unit cells along the full width of the channel when we record trajectories of the capsules, and 90 cells for determining the lift force profiles. Especially for soft particles (La = 1 to 10) and high Reynolds numbers (Re = 100) the lift force is not constant but oscillating in time. To avoid these oscillations, the resolution is further enhanced to 180 cells. The instability in the mesh is mainly caused by the bending contribution Eq. (2.71). By changing the formula for the bending one can improve the numerical stability of the mesh and reduce the required resolution [104].

In this chapter we characterize the deformable capsule by the capillary number Ca or the Laplace number La (*cf.* Sec. 2.6.3) and analyze the change introduced by varying the particle radius a and the channel Reynolds number Re. We defined the capillary number and the Laplace number as follows (*cf.* Sec. 2.6.3)

$$\text{Ca} = \frac{\rho \nu u_{\max} a}{w \kappa_s} \quad \text{and} \quad \text{La} = \frac{\kappa_s a}{\rho \nu^2} \,. \tag{6.1}$$

We vary the Laplace number in the interval between 1 (very soft) and 1000 (almost rigid) which corresponds to a capillary number between $1 \cdot 10^{-4}$ and 10. For the Reynolds number we choose the values 5, 10, 50 and 100.

6.2 Equilibrium position of a deformable capsule

6.2.1 Influence of deformability on the equilibrium position

We first study the equilibrium position of one single capsule as a function of its deformability. To determine the equilibrium position of the capsule we use two different methods. The first method is closer to the experiment, the second uses lift force profiles and will be explained further below. In the first method, the particle is put at a specific position and can then move freely. Figure 6.1 shows a collection of example trajectories in the lateral plane. In the initial phase the particles migrate in the direction of the channel center. When the particles are close to their equilibrium distance they change direction and move in a polar direction toward their final equilibrium positions, which is located on the
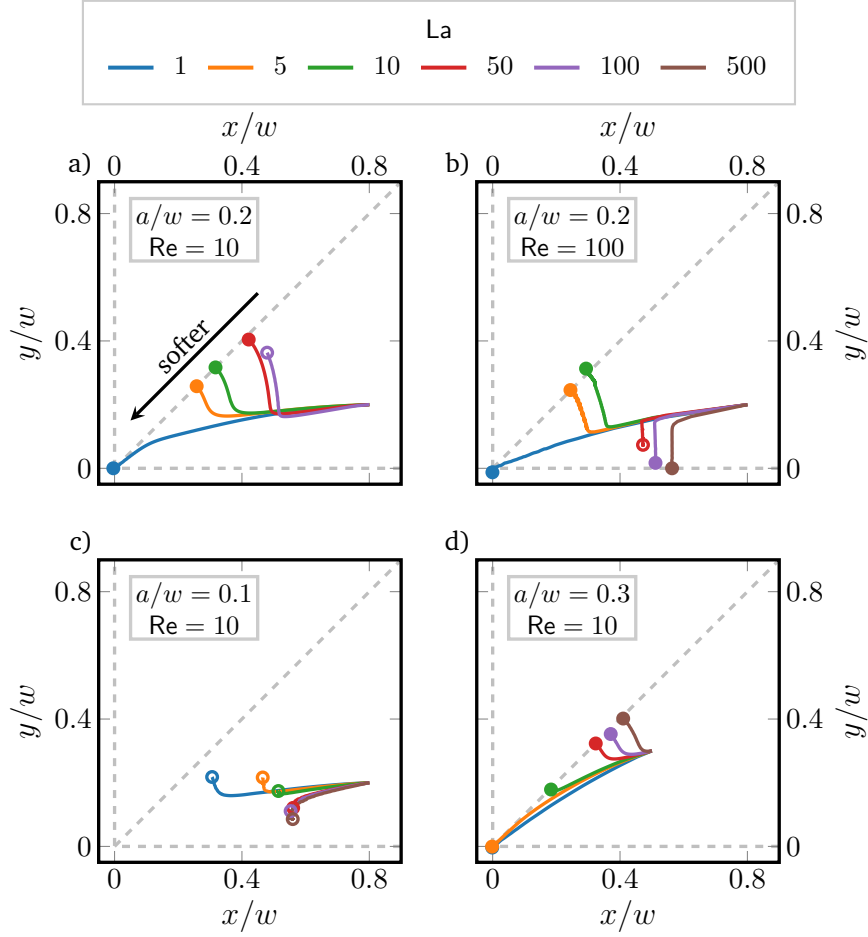
Figure 6.1: Trajectories of the capsules in the cross-sectional plane of the channel with different rigidity quantified by the Laplace number La. The trajectories are plotted for different particle sizes a/w and Reynolds numbers Re as indicated in **(a)–(d)**. The capsules start at the same position and the endpoint of the trajectories are shown by filled circles. Some simulations did not reach their steady state indicated by the open symbols. The more deformable the capsule is (smaller La), the closer the particle migrates toward the channel center at $x = y = 0$. The migration process is split into two different processes. First the particle migrates fast radially toward the channel center. When the particle reaches its approximated equilibrium distance, it changes the direction and slowly migrates toward its equilibrium position.
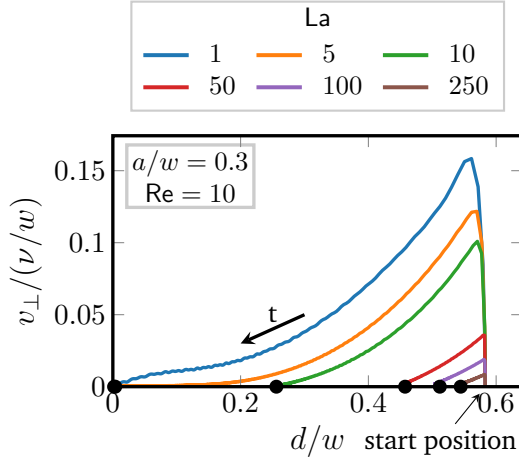
Figure 6.2: Lateral velocity $v_\perp$ plotted versus the distance d to the channel center for different Laplace numbers La. All particles start at the same initial position ($d/w = 0.583$) and with time move inwards to their equilibrium positions indicated by a black dot.

diagonal for most particles. Only small capsules with $a/w = 0.1$ and capsules at Re $= 100$, which are sufficiently rigid (La > 50), clearly migrate toward the x axis [Fig. 6.1 (b,c)].

While this method gives a good indication for the migration process it is also computationally costly. Especially the small particles with $a/w = 0.1$ at Re $= 10$ migrate slowly and do not reach a steady state, even in the longest simulation runs [Fig. 6.1 (c)]. The reason is that the lift force driving the particle motion strongly scales with particle radius a and Reynolds number as we discuss later in this chapter. However, in most cases one clearly sees to which position the particles migrate. The trajectories are similar to those of rigid particles, which has been thoroughly studied in Ref. [38]. One key result is that larger particles migrate toward the diagonal, where they are further away from the walls, while smaller particles migrate toward the main axes.

As Fig. 6.1 gives no indication of the time scale of the migration, we analyze the lateral velocity $v_\perp$ as a function of the distance d from the center (Fig. 6.2). For this we focus on the trajectories visualized in Fig. 6.1 (d). In all simulations the particle starts at the same position at a distance $d/w = 0.58$. After a rapid increase in the beginning, the velocity gradually decreases to zero as the particles move toward their equilibrium distance. Clearly, softer particles (small La) show a larger lateral migration velocity than rigid particles. The migration process splits into two phases. In the first phase the gradual decrease of the lateral velocity corresponds to the inwards directed motion. When the capsules are close to their final equilibrium distance, the radial movement stops and the lateral velocity is close to zero. In the second phase the particles slowly drift along the polar direction toward their equilibrium positions. The velocity is so small that it is hardly recognizable in Fig. 6.2. These two different phases indicate a similar process as discussed in Sec. 2.5.6, where the fast inwards directed motion was related to a shear-induced migration while the second process was attributed to the rotation-induced migration.

As mentioned, the free trajectories require long simulation times. To determine the equilibrium positions more efficiently, we measure the lift force profiles using the method outlined in Sec. 3.5. The equilibrium positions correspond to the stable fix points. We discuss the lift force profiles in more detail in Sec. 6.4. Figure 6.3 shows the 2D lift
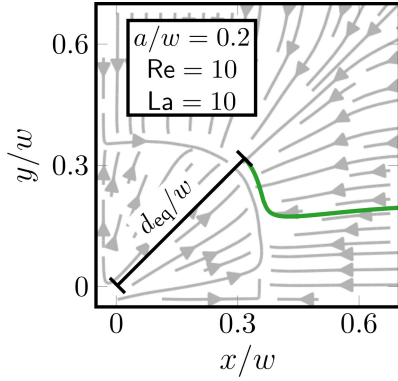
Figure 6.3: 2D-lateral lift force profile for the La = 10 trajectory in Fig. 6.1 (a). The streamlines correspond to the lift force at that position and agrees with the lateral trajectory (green line).

force streamline which corresponds to the actual trajectory observed for the free flowing particle. To obtain these lift force streamlines, we fix the lateral position of the capsule and calculate the force and interpolate in-between. As most equilibrium positions are located on the diagonals, we only determine the lift force profiles along that line.

In Figure 6.4 (a) we plot the equilibrium distance as a function of the deformability of the capsule for different Reynolds numbers Re. For the rigid particles we observe that the particles move closer toward the channel wall as the Reynolds number increases. This was already predicted by analytical calculations [92] and observed by experiments [32, 44] and simulations [35]. The shift toward the center is related to a change in the vorticity production around the particle. When the deformability-induced lift force becomes more dominant, the capsule migrates to an equilibrium position which is closer to the channel center. As the strength of the inertial forces increase with Re^2, the capillary number needs to be much larger at higher Reynolds numbers for the particle to assemble at the channel center.

All curves roughly have the same shape and shift to the right with increasing Re. This
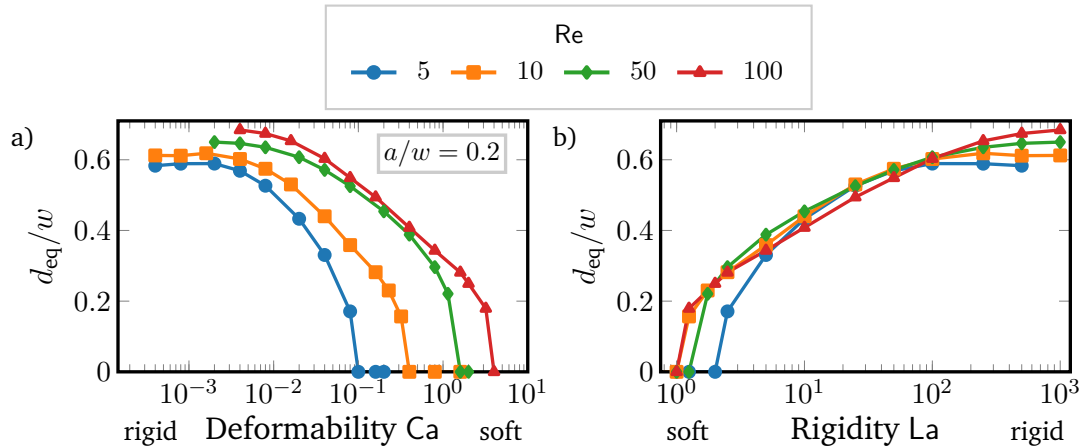

Figure 6.4: Equilibrium distance d_{eq}/w from the channel center as a function of **(a)** the capillary number Ca and **(b)** the Laplace number La for different Reynolds numbers Re. The particle radius is $a/w = 0.2$.
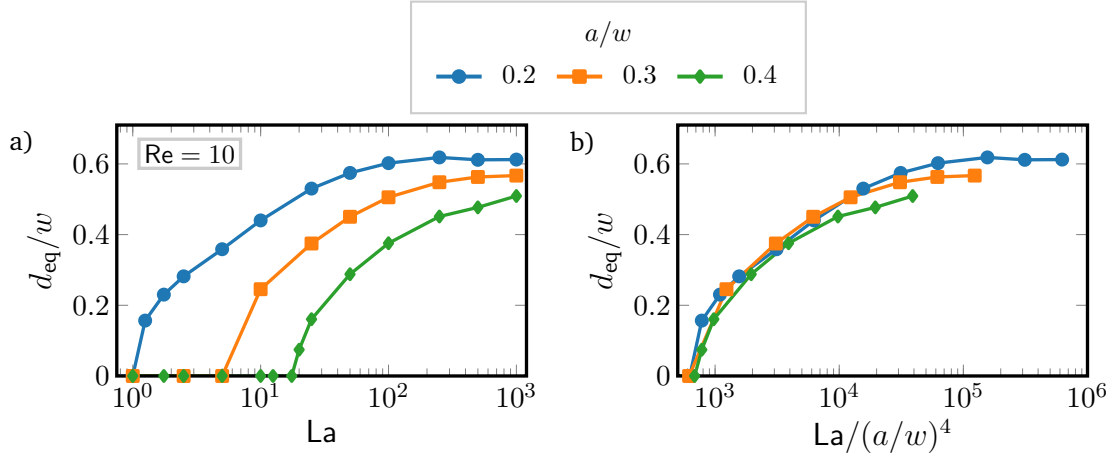
Figure 6.5: Equilibrium distance d_{eq}/w from the channel center for different particle radii. **(a)** d_{eq}/w plotted versus La, **(b)** d_{eq}/w versus $La/(a/w)^4$. The Reynolds number is Re = 10.

indicates a more general dependency of the equilibrium distance. As we already discussed in Sec. 2.6.3, the capillary number Ca is proportional to the absolute flow velocity u_{max}. Indeed, removing this dependency and plotting the equilibrium distance versus the Laplace number La, which measures the rigidity of the capsule, all curves roughly fall onto one master curve [Fig. 6.4 (b)]. This was already observed by Kilimnik *et al.* [169]. Deviations from the master curve occur for rigid capsules (large La), which move closer to the channel walls with increasing Re [32, 35, 92]. Also, for very low values of La, the value where the capsule starts to move away from the channel center is sensitive to Re. This might be due to the fact that the shapes of two capsules, located either in the channel center or close-by, differ strongly as we will discuss below. Our results for the equilibrium distance were later also confirmed by finite volume calculations [61].

The fact that the equilibrium position can be scaled on a master curve may seem surprising, since the shear deformation increases with the Reynolds number. However, the analytical expression for the deformability-induced lift force in Stokes flow [Eq. (2.76)] is also proportional to u_{max}^2, which is the same scaling as in the inertial lift force [*cf.* Eq. (2.65)]. While this formula was derived for vanishing Reynolds numbers and small deformations, the formula still holds close to the centerline as we discuss later in Sec. 6.4.

Furthermore, the particle radius a/w plays an important role for the equilibrium distance, as Fig. 6.5 (a) demonstrates. Larger particles leave the channel center at larger La and thereby assemble closer to the channel center compared to smaller particles. One reason for this behavior is that La $\propto a$. Additionally, the lift force, which drives the capsule away from the center, roughly scales with a^3 as discussed in Ref. [15] and Sec. 6.4. So, if we plot d_{eq} versus $La/(a/w)^4$, the equilibrium distances collapse on a master curve in the regime where the capsules are deformable [Fig. 6.5 (b)]. For rigid particles (large La) the curves do not collapse since smaller particles move closer to the channel walls [16, 35].

6.2.2 Influence of the channel cross section on the equilibrium position

So far we only discussed a quadratic channel cross section. However, as illustrated in Fig. 2.10 the number of equilibrium positions for a rigid particle can be adjusted by varying the aspect ratio. For rigid particles it was reported that the diagonal equilibrium position, where larger particles are located, switches toward the short axis at $w/h \approx 0.75$ [38]. We mark the location of stable fixed points by a black dot and unstable fixed points by a white dot. Half filled dots indicate saddle fixed points which are stable only along one direction [38].

As discussed earlier, deformable capsules in a quadratic cross section mostly migrate toward the diagonal. When we now decrease the aspect ratio w/h, we find that relatively stiff particles (La = 250) still assemble close to the diagonal while this equilibrium position completely moves toward the short axis at $w/h = 0.5$ (see Fig. 6.6). This agrees with the results for rigid particles [38].

We now fix the channel's aspect ratio to $w/h = 0.5$ and study what happens if the particle becomes softer (Fig. 6.7). While the equilibrium position of the rigid particle with La = 250 was located on the short axis, a softer particle with La = 100 moves in the direction of the diagonal. For an even softer particle (La = 10) the equilibrium position moves again to a main axis but in this case toward the long axis. On the long axis the shear rate is smaller which decreases the elastic stress on the particle. This trend was already observed by Ref. [172]. However, they do not comment on this result. For very deformable particles (La = 1), the equilibrium position is again located at the channel center. We note that the particle with $a/w = 0.4$ and La = 10 is already focus at the channel center in case of a quadratic cross section (*cf.* Fig. 6.5). Thus, aspect ratio of the channels further allows to fine-tune the position of the equilibrium position which might offer new possibilities for cell sorting.

In the following we again concentrate on quadratic channel cross sections.

6.3 Deformation of the capsule

In Fig. 6.8 we illustrate the shapes of capsules at their equilibrium positions for different Laplace numbers (La) and two values of the Reynolds number Re = 10 and Re = 100. At La = 1 the capsules are located in the channel center and show the expected form of a parachute, which is more visible at larger Reynolds numbers [173]. At La = 2.5, the capsules have left the center with $d_{\text{eq}}/w \approx 0.28$ and the deformation is more asymmetric. The capsules are less deformed with increasing La, although the capsules move further away from the channel center, where the viscous shear stresses increase due to the parabolic flow profile. Interestingly, although the shapes of capsules with the same La differ for the two Re values, in Fig. 6.4 we demonstrated that their equilibrium distances to the channel center are roughly the same independent of Re. This indicates, that the shape and the deformation of a capsule is a result of the local shear rate and has only limited effect on the equilibrium position.
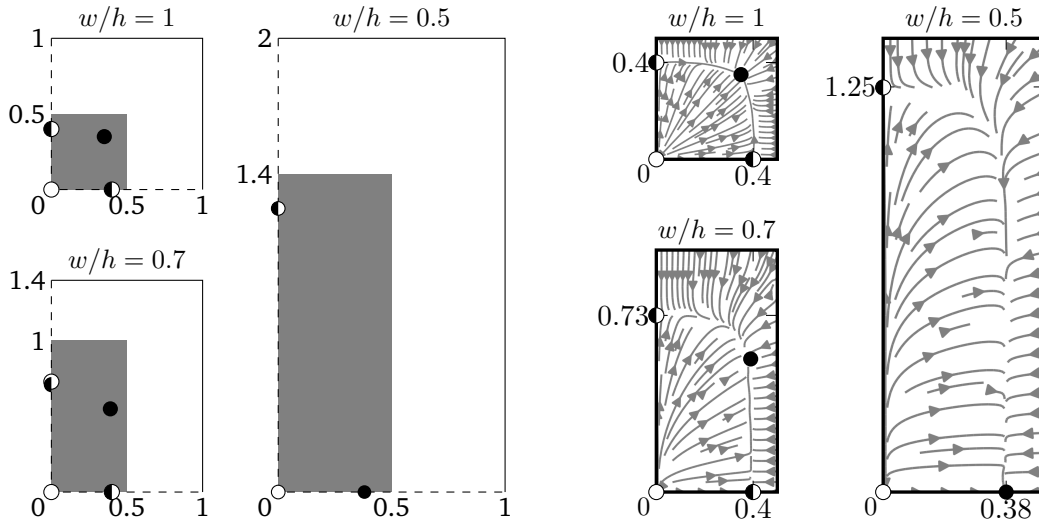
Figure 6.6: **Left** Upper left quadrant of the channel cross section for different aspect ratios. The origin is in the channel center. The gray areas mark the areas for which the lift force profiles on the right are plotted. **Right** Streamlines of the lateral lift force profiles. The lines indicate possible trajectories based on the lift force. The markers indicate stable (filled circles), saddle (half-filled circles) and unstable (empty circles) fixed points. With decreasing aspect ratio the fixed points move closer toward the short axis and vanish for aspect ratios $w/h \geq 0.5$. The parameters are $a/w = 0.4$, Re $= 20$ and La $= 250$.
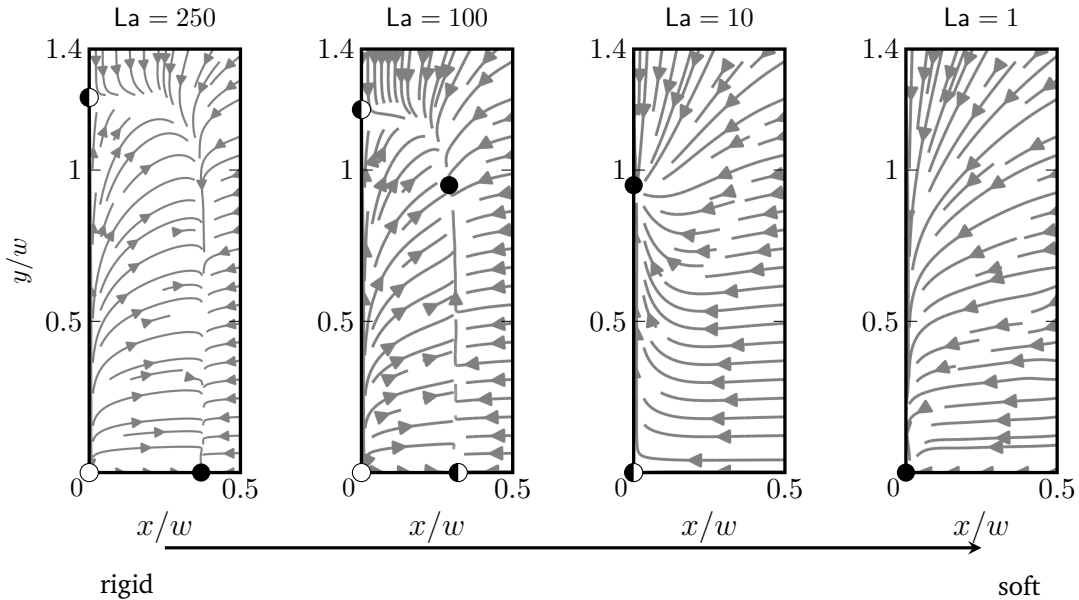
Figure 6.7: Lateral lift force profiles for different Laplace numbers for a channel with rectangular cross section ($w/h = 0.5$). Stiff capsules (La $= 250$) migrate toward the short channel axis in agreement to rigid particles. With decreasing rigidity (La ≈ 100) a new stable fixed point emerges close to the diagonal. For a Laplace number La $= 10$ the equilibrium position is located at the long channel axis. Very soft particles (La $= 1$) still migrate toward the channel center. The other parameters are $a/w = 0.4$ and Re $= 20$.

La	1	2.5	10	100	
Re					

10					$\overrightarrow{u}$
	0	0.28	0.44	0.60	d_{eq}/w

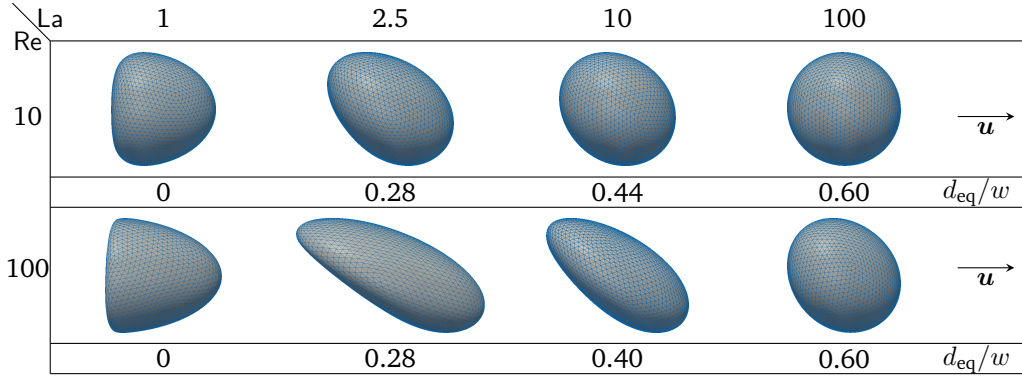| 100					$\overrightarrow{u}$
	0	0.28	0.40	0.60	d_{eq}/w

Figure 6.8: Shapes of the capsules for different Laplace and Reynolds numbers. Below each picture is the corresponding equilibrium distance. The flow is directed to the right.

To quantify the deformation of the capsule, we determine the Taylor deformation index D (*cf.* Sec. 2.6.5) at the equilibrium position of the particles. As mentioned above, the deformation is the result of the shear rate which is proportional to the Reynolds number Re. To compare the different deformation indices we normalize by the Reynolds number. In Fig. 6.9 we plot $D/$Re versus Laplace number La for different Re. Very rigid particles (La $= 500$) assemble around halfway between the channel walls and the center and are hardly deformed (small D). The softer the particles become, the more they are deformed asymmetrically, which means increasing D. This happens although capsules migrate to smaller equilibrium distances d_{eq}, where shear gradients are lower. At small La values, where the equilibrium distances d_{eq} in Fig. 6.4 (b) sharply decrease to zero, the deformation indices also sharply decrease to small values since the capsules have a more symmetric parachute shape in the channel center. The sharp decrease of D becomes less prominent with decreasing Re since the capsules are less deformed. For stiff particle (La ≈ 50) the deformation follows the analytical solution for a capsule in linear shear flow [Eq. (2.78)] where we use the mean shear rate (violet line in Fig. 6.9).
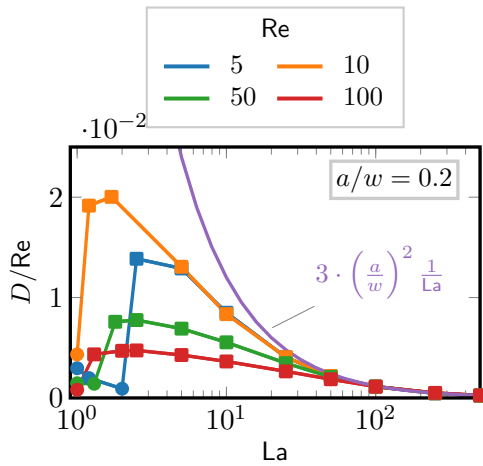
Figure 6.9: Taylor deformation index D of an elastic capsule at the equilibrium location plotted versus Laplace number La for different Reynolds numbers Re. The deformation index in scaled by the Reynolds number. The symbols correspond to the symmetric shapes in the channel center (●) and to the asymmetric shapes occurring not in the center (■). Violet line shows the analytical expression for a deformable capsule in linear shear flow.
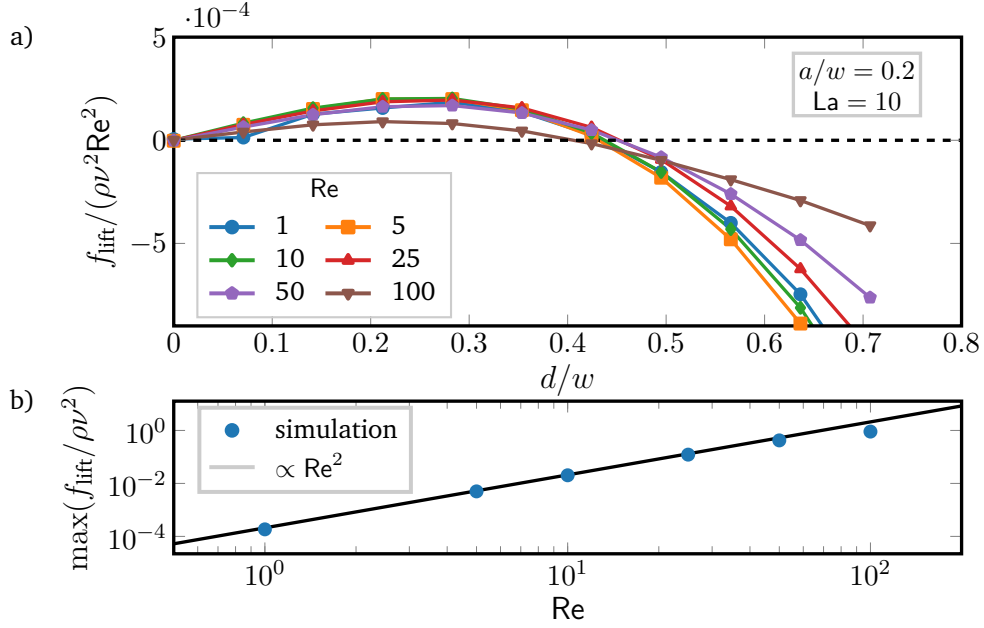
Figure 6.10: **(a)** Inertial lift force f_{lift} along the diagonal in units of $\rho\nu^2\text{Re}^2$ plotted versus distance d/w to the center for different Reynolds numbers Re. Other parameters are La $= 10$ and $a/w = 0.2$. **(b)** Maximum of f_{lift} plotted versus Re.

6.4 Lift force profile

6.4.1 Lift force scaling

The dynamics and equilibrium positions of an elastic capsule are determined by the lift force profile. In this section we study how the inertial lift force scales with Reynolds and Laplace number as well as particle radius and compare it to rigid particles. For rigid particles with radii much smaller than the channel width the analytical solution [64, 92] for the lift force predicts the scaling $f_{\text{lift}} \propto \text{Re}^2(a/w)^4$. For larger rigid particles, of similar size as ours, numerical solutions of the Navier-Stokes equations give a scaling proportional to $\text{Re}^2(a/w)^3$ near the channel center and $\text{Re}^2(a/w)^6$ near the channel walls [54]. To measure the lift force we follow the procedure described in Sec. 3.5. As almost all capsules travel to equilibrium positions on the diagonal (*cf.* Sec. 6.2.1), we study the lift force profiles along this direction.

We usually observe the typical form of the lift force profile with two equilibrium positions of the capsule, where the lift force vanishes [see, for example, Fig. 6.10 (a)]: one unstable fix point in the channel center ($d = 0$) and one stable fix point between channel center and walls. In the previous section we found that the equilibrium position is almost independent of the Reynolds number, in particular, in an intermediate range of capsule rigidity measured by La. This independence of the Reynolds number is also visible in the lift force profiles measured for different Reynolds numbers where all zero crossings coincide [see Fig. 6.10 (a)]. Furthermore, the profiles for small Re fall on top of each

a)

b)

Figure 6.11: **(a)** Inertial lift force f_{lift} along the diagonal in units of $\rho\nu^2(a/w)^3$ plotted versus distance d/w to the center for different particle radii a/w. Other parameters are La $= 10$ and Re $= 10$. **(b)** Maximum of f_{lift} plotted versus a/w.

Figure 6.12: Inertial lift force f_{lift} along the diagonal in units of $\rho\nu^2(a/w)^3$ plotted versus distance d/w to the center for different particle radii a/w. Other parameters are La $= 500$ and Re $= 10$. In contrast to the softer particles (Fig. 6.11), the $(a/w)^3$ scaling also holder for larger particles.
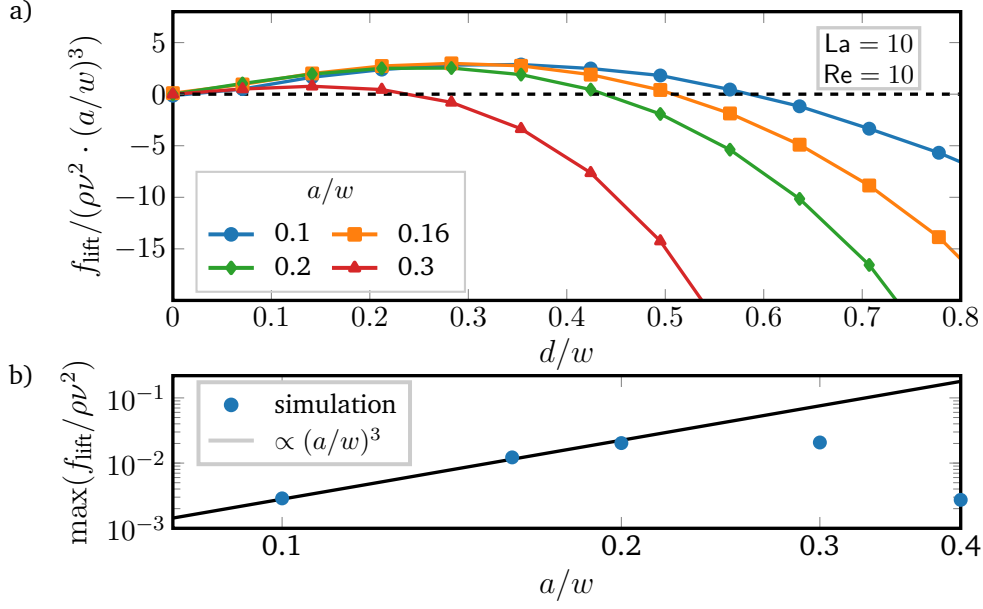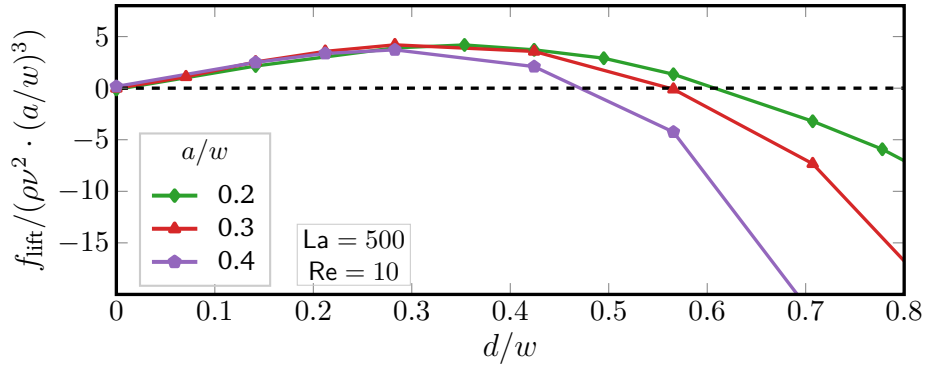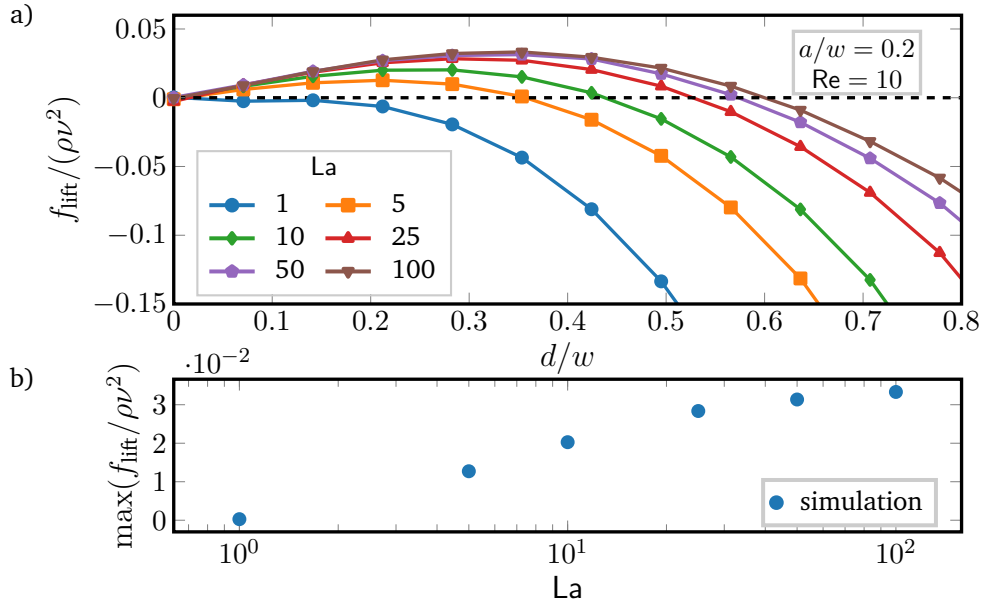
Figure 6.13: **(a)** Inertial lift force f_{lift} along the diagonal in units of $\rho\nu^2$ plotted versus distance d/w to the center for different Laplace numbers La. Other parameters are Re $= 10$ and $a/w = 0.2$. **(b)** Maximum of f_{lift} plotted versus La.

other when we scale f_{lift} by Re^2. This scaling is confirmed in Fig. 6.10 (b), where we plot the maximum lift force versus Re. Only for high Reynolds number (Re $= 100$) we obtain a deviation from $f_{\text{lift}} \propto$ Re^2. Indeed, by measuring the particle–wall interaction of rigid particles, the authors of Ref. [89] noticed an increase of the wall lift coefficient around Re ≈ 100 due to an imperfect bifurcation of the wake structure. This might explain our observation. However, in total the scaling law $f_{\text{lift}} \propto$ Re^2 also seems to be valid for soft spheres at moderate Re.

As a next step, we analyze how the lift force scales with the particle radius. Fig. 6.11 (a) confirms the scaling $f_{\text{lift}} \propto (a/w)^3$ for small distances, while closer to the walls the force profiles clearly differ. Strong deviations also occur for larger particles with $a/w \geq 0.3$, which is also visible in the maximum lift force plotted versus a/w in Fig. 6.11 (b). This is in contrast to Ref. [15] and [35], where the scaling was verified for rigid particles with radii up to $a/w = 0.38$. The different behavior can be attributed to the deformability of the capsules. Indeed, for La $= 500$ we verify the scaling up to a particle radius of $a/w = 0.4$ (Fig. 6.12).

6.4.2 Influence of the deformability on the lift force profile

So far we have confirmed that the scaling for the Reynolds number and the particle radii also holds for deformable capsules. The last remaining quantity is the scaling with the Laplace number [see Fig. 6.13 (a)]. For large Laplace numbers the lift force is that of a rigid particle. Making the particles softer, the stable equilibrium position moves toward
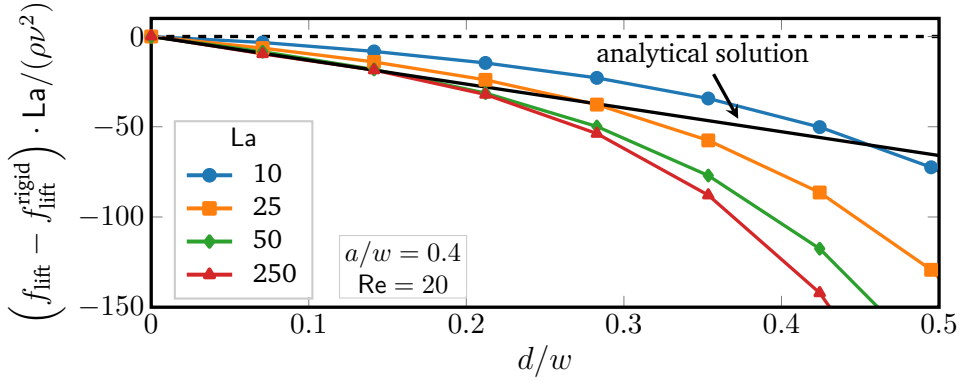
Figure 6.14: Deformability-induced lift force profile along the diagonal of a quadratic cross section. Here we subtract the lift force of a rigid particle $f_{\text{lift}}^{\text{rigid}}$ and scaled the difference with the Laplace number. For particles with $\text{La} > 25$ this lift force close to the center $x/w < 0.25$ follows approximately the analytical solution given by Eq. (2.76).

the channel center and ultimately for $\text{La} = 1$ reaches the center, as already discussed in Sec. 6.2. Also, the maximum value of the lift force decreases the softer the particles become as illustrated in Fig. 6.13 (b). At this point we cannot extract a scaling of the lift force with the Laplace number.

To get a better understanding of the deformability-induced lift force we subtract the lift force of a rigid particle (see Fig. 6.14). The remaining contribution is the deformability-induced lift force which follows the analytical expression [Eq. (2.76)] in the vicinity ($x < 0.2$) of the channel center and for $\text{La} > 25$. The analytical expression for the deformability-induced lift force was derived under the assumption of small deviations (large La) and vanishing Reynolds numbers (*cf.* Sec. 2.6.4). Furthermore, the particle-wall interactions were neglected. When these assumptions are no longer fulfilled we find a deviation of the analytical form and the next higher order needs to be considered.

In summary, we conclude that the lift force of a deformable capsule close to the center can be written as a combination of the inertial Segré-Silberberg force $f_{\text{lift}}^{\text{rigid}}$ and the deformability-induced lift force derived at vanishing Reynolds numbers $f_{\text{lift}}^{\text{deform}}$

$$f_{\text{lift}} \propto a^3 \text{Re}^2 \left(f_{\text{lift}}^{\text{rigid}} + \frac{1}{\text{La}} f_{\text{lift}}^{\text{deform}} \right) . \tag{6.2}$$

6.5 External control force

Experiments and simulations showed that the lateral position of rigid particles can be controlled by an external force which is applied along the channel axis [38, 88]. Depending on the sign of the external force the particle is either accelerated or decelerated relative to the channel flow. This changes the relative velocity between particle surface and surrounding fluid resulting in a Saffman force (*cf.* Sec. 2.5.5).
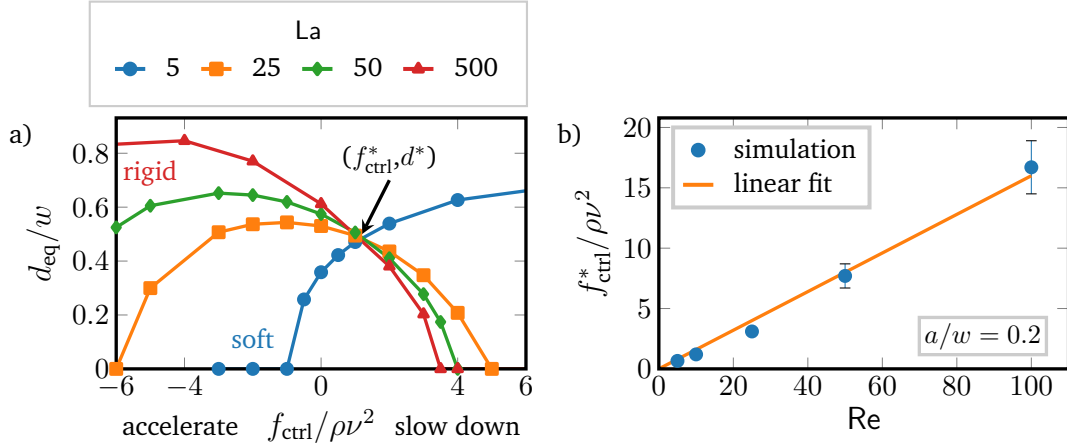
Figure 6.15: **(a)** Equilibrium distance d_{eq} plotted versus the external control force f_{ctrl} for different Laplace numbers La. Other parameters are Re $= 10$ and $a/w = 0.2$. **(b)** Control force of the intersection point f^*_{ctrl} plotted versus Reynolds number Re. At lower Reynolds numbers the error-bars are on the order of the symbol size.

In the following, we analyze how such an external force influences the equilibrium position of a deformable capsule. For this we apply a constant force on the elastic capsule which is evenly distributed on the membrane vertices. We follow the convention that a positive force is directed against the flow and thus slows down the particle [38]. In Fig. 6.15 (a) we plot the equilibrium distance to the channel center as a function of the external control force f_{ctrl}. As before, we determined the equilibrium positions from the stable fix points of the lift force profiles along the diagonal of a quadratic cross section. For a rigid capsule (La $= 500$) the results agree with previous simulations [38]: when the particle is slowed down ($f_{ctrl} > 0$), it moves toward the channel center and ultimately reach it for sufficiently large $f_{ctrl} > 0$, while an accelerated particle moves closer to the channel walls.

With increasing deformablity we observe that the equilibrium distance decreases for strongly negative control forces. At La $= 25$ the off-centered equilibrium position along the diagonal vanishes for large absolute values of the control forces. For an even softer capsule (La $= 5$) the behavior reverses and the capsule behaves opposite to a rigid particle. When the particle is slowed down, it moves away from the channel center. When it is accelerated, it approaches the center and ultimately stays there.

Förtsch *et al.* observed a similar kind of migration for a soft capsule under gravity at
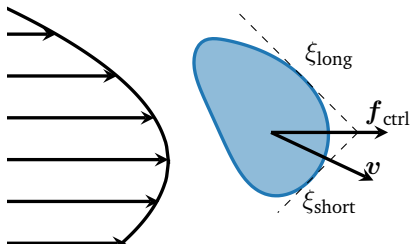

Figure 6.16: Illustration of the anisotropic drag reduction for a deformable capsule. Due to its elongated shape the capsule experiences a different drag coefficient along its short axis and its long axis. When an external control force $\boldsymbol{f}_{ctrl}$ pulls on the particle, the velocity $\boldsymbol{v}$ contains a contribution perpendicular to the force.

vanishing Reynolds numbers [174]. They showed by simulation and analytical calculations that this can be explained by the anisotropic drag coefficient. Due to its elongated shape the resistance of the soft capsule is different along its main axes (Fig. 6.16). Pulling on such a deformed capsule with a force directed along the flow, results in an additional lateral velocity component.

Furthermore, we find that all curves in Fig. 6.15 (a) for different La intersect in one point at a positive control force of about $f^*_{\text{ctrl}} = 1.2\rho\nu^2$. At this control force all particles assemble at the same equilibrium distance d^*_{eq} independent of their deformability. This property seems to be generic as we also find it for other Reynolds numbers. While the intersection point moves to higher control forces with increasing Reynolds number, in fact, $f^*_{\text{ctrl}} \propto \text{Re}$ as Fig. 6.15 (b) demonstrates, the distance from the channel center stays almost the same at $d^*/w \approx 0.46$. We do not have a clear understanding of this behavior. However, we checked that it is generic and not a numerical artifact. In particular, this behavior does not change when we increase the channel length to investigate the influence of the periodic boundary condition or when we increase the resolution of the lattice-Boltzmann grid to check for discretization errors.

Using an external force, allows a much finer control of the particle's equilibrium position compared to the passive system. For example, in the absence of a control force ($f_{\text{ctrl}} = 0$ in Fig. 6.15) the equilibrium position of particles with La = 5 and La = 25 are quite close to each other. By applying $f_{\text{ctrl}} = -1.2\rho\nu^2$ the softer particle moves toward the center while the equilibrium position of the less deformable particle hardly changes. This effect should help to enhance particle separation based on its deformability. One way to implement an external force experimentally could be using buoyancy where fluid and particles have a different density. When the channel is directed upright, gravity could act as an axial force.

6.6 Conclusions

In this chapter we studied the Segré-Silberberg effect for a deformable capsule. While the fluid inertia focuses particles onto off-centered equilibrium positions, the deformability results in an additional lift force with pushes the particle toward the channel center. The rigidity, quantified by the Laplace number, determines which effect is more dominant.

We found that most particles assemble along the diagonal of the channel. The softer the particles are, the closer they move toward the channel center. Their final equilibrium distance depends on the particle rigidity, its radius and the channel Reynolds number. By introducing the Laplace number as ratio of elastic force to the intrinsic viscous force scale, the equilibrium position for different Reynolds numbers collapse on a single master curve. The equilibrium distance is thus independent of the flow velocity. Additionally, we also identified such a data collapse for different particle radii.

By changing the aspect ratio of the channel we could further fine-tune the position of the equilibrium position. For a channel with a rectangular cross section a rigid particle is focused along the short axis. For more deformable particles we observed, that their equilibrium position moves in the direction of the diagonal. With increasing deformability

the equilibrium position first moves toward the long axis of the channel cross section where the shear gradient is smaller. Only very soft particles get focused in the center of the channel. However, the Laplace number for the center position is a magnitude lower than in the case of a square channel.

In contrast to the equilibrium distance we found that the deformation of the capsules strongly depends on the Reynolds number. The deformation of the off-centered capsules increases with decreasing Laplace number although the capsules migrate in areas with a smaller shear gradient. Very soft capsules assemble at the channel center and have a symmetric parachute shape.

The lift force profiles of deformable capsules behave pretty much the same as those of rigid particles, where the lift force scales as $f_{\mathrm{lift}} \propto \mathrm{Re}^2(a/w)^3$. For deformable capsules, we observed deviations from this scaling law only for high Reynolds number ($\mathrm{Re} = 100$) and large particles ($a/w = 0.3$). We were not able to identify a scaling involving the Laplace number. However, we found that the force on a deformable capsule can be written as sum of the inertial lift force for a rigid particle and the deformability-induced lift force derived for capsules in the absence of inertia.

Finally, we demonstrated that the particle equilibrium position can be controlled by an external force along the channel axis. For almost rigid particles ($\mathrm{La} = 500$) we confirmed previous results [38], but found a new behavior for soft particles. While rigid particles migrate toward the channel center when they are slowed down, moderately soft particles with $La \approx 25$ migrate toward the channel center both for positive and negative control forces. For even lower La the capsules behave opposite to rigid particles as they move toward the channel wall when slowed down. Interestingly, we observed that all graphs with different Laplace numbers intersect in one point at a non-zero control force.

7

Conclusions

In this thesis, we analyzed pairs and trains of rigid particles as well as a single deformable capsule in a microfluidic channel in the inertial regime. In the following we shortly review the main results.

First, we analyzed the dynamics of a pair of rigid particles moving in the x-z-plane in chapter 4. We determined the possible types of trajectories as a function of the initial lateral positions of the leading and lagging particles. We found four different types of trajectories which we named *swapping*, *passing*, *moving-apart* and *damped oscillations*. While the first three types result in an unbound configuration where the particles ultimately move apart, the damped oscillations end in a bound state characterized by a distinct axial spacing. We quantified the frequency and the damping rate of the oscillations. The scaling of both quantities indicates that the oscillations are driven by the viscous disturbance flow and the inertial lift forces push the particles towards their equilibrium position resulting in the damping. Furthermore, we determined the two-particle lift force profiles as a function of the lateral positions, the axial spacing and the Reynolds number. The presence of the second particle increases the strength of the lift force compared to the single-particle case and influences the shape of the profile. The effect of the second particle is mostly determined by the axial spacing between the two particles and rapidly decreases with increasing distance. The lift forces acting on the particles exhibit a strong asymmetry between the leading and the lagging particle as a consequence of inertial secondary flows. By determining the scaling of the lift force with the Reynolds number we found that the two-particle lift force exhibits a viscous scaling at close particle separations. Only when the spacing increases, the inertial scaling is recovered. Finally, we used the calculated lift force profiles to explain the damped oscillations.

We extended our research to multiple rigid particles in chapter 5 and focused on the stability of pairs and trains. In contrast to the previous chapter we initialized the particles at their lateral equilibrium position but not at their axial equilibrium spacing. First, we demonstrated that cross-streamline pairs attract each other over large distances resulting always in the same axial spacing even when both particle were initialized at the same lateral distance from the channel center. In contrast, we did not observe an equilibrium spacing for same-streamline pairs. Instead, we found that the strong repulsion at close distances combined with a rapid decay of the influence of the second particle resulted in a

characteristic peak in the distribution of the axial spacing in agreement with experimental results [47]. Adding more particles, we studied how a staggered train relaxes towards its equilibrium configuration. When the axial particle spacing is larger than the equilibrium distance, the train contracts non-uniformly due to a collective drag reduction. Similarly, linear trains drift apart in a non-uniform way where the leading particle separates from the train in agreement to Ref. [153]. Finally, we studied how a displacement pulse travels through a staggered train which is related to the swapping and passing trajectories of the previous chapter. We conclude this chapter with a quantitative analysis of the damping and the pulse to train velocity ration.

In the last chapter of this thesis we focus on a single deformable capsule. This deformability leads to an additional lift force which is directed to the center of the channel. In chapter 6 we study the combination of deformability-induced migration and the Segré-Silberberg effect. We find that a capsule moves to an equilibrium position closer to the channel center with increasing deformability. In quadratic channels we observe that most particles move towards the diagonals, while in rectangular channels the position of the equilibrium position changes with the Laplace number. We demonstrate that the Laplace number is suitable to characterize the rigidity of the particles as it enables us to scale the equilibrium distance on a master curve independent of the Reynolds number. Furthermore, we confirm that the scaling of the lift force for a single rigid particle also holds for a deformable capsule. The inertial lift force acting on a deformable capsule can be expressed as a sum of the lift force for a rigid particle and a deformable contribution which is inversely proportional to the Laplace number. Finally, we studied how a deformable particle moves under the influence of an external axial force which speeds up or slows down the particle relative to the flow resulting in a Saffman force. Surprisingly, we find the behavior of a soft capsule is reversed compared to a rigid particle. This can be understood by the anisotropic drag coefficient of the elongated capsule [174]. Moreover, we observe that a specific axial force exists at which the particles assemble at an equilibrium position which is independent of the deformablity. This effect might be helpful to enhance sorting and separation of particles based on their size and deformability.

Our work raises further interesting questions, and we outline directions for future research in the following. We restricted our analysis of rigid particles to monodisperse particles of radius $a/w = 0.4$. However, many applications involve polydisperse particle distributions. Recently, Gao *et al.* experimentally studied trains at a low confinement ratio with particles of two different radii [45]. The authors observed that the larger particles typically lead the trains. Simulations of polydisperse systems offer new insights on the relevant effects for rigid particles in inertial microfluidics.

Biomedical applications typically use deformable cells or droplets. While we only considered a single deformable capsule in this thesis, the interactions of multiple deformable particles is certainly another interesting research field. A pair of soft particles at vanishing Reynolds number shows attractive behavior [175] and can even form microfluidic crystals [176]. Extending our work of chapter 4 and 5 to deformable particles promises valuable insights.

List of publications

Related to this work

[A]   C. Schaaf and H. Stark, "Inertial Migration and Axial Control of Deformable Capsules", *Soft Matter* **13**, 3544 (2017).

[B]   C. Schaaf, F. Rühle, and H. Stark, "A Flowing Pair of Particles in Inertial Microfluidics", *Soft Matter* **15**, 1988 (2019).

[C]   C. Schaaf and H. Stark, "Particle Pairs and Trains in Inertial Microfluidics", *Eur. Phys. J. E* **43**, 50 (2020).

Other publications

[D]   C. Schaaf and S. Gekle, "Dielectric response of the water hydration layer around spherical solutes", *Phys. Rev. E* **92**, 032718 (2015).

[E]   C. Schaaf and S. Gekle, "Spatially Resolved Dielectric Constant of Confined Water and Its Connection to the Non-Local Nature of Bulk Water", *The J. Chem. Phys.* **145**, 084901 (2016).

[F]   J. Grawitter, R. van Buel, C. Schaaf, and H. Stark, "Dissipative Systems with Nonlocal Delayed Feedback Control", *New J. Phys.* **20**, 113010 (2018).

[G]   R. van Buel, C. Schaaf, and H. Stark, "Elastic Turbulence in Two-Dimensional Taylor-Couette Flows", *EPL* **124**, 14001 (2018).

[H]   F. Rühle, C. Schaaf, and H. Stark, "Optimal Control of Colloidal Trajectories in Inertial Microfluidics Using the Saffman Effect", *Micromachines* **11**, 592 (2020).

Bibliography

[1] S. H. Strogatz, *Sync: the emerging science of spontaneous order*, 1st ed. Hyperion, 2003.

[2] G. Segré and A. Silberberg, "Radial Particle Displacements in Poiseuille Flow of Suspensions", *Nature* **189**, 209 (1961).

[3] G. Segré and A. Silberberg, "Behaviour of Macroscopic Rigid Spheres in Poiseuille Flow Part 2. Experimental Results and Interpretation", *J. Fluid Mech.* **14**, 136 (1962).

[4] H. L. Goldsmith and S. G. Mason, "Axial Migration of Particles in Poiseuille Flow", *Nature* **190**, 1095 (1961).

[5] S. Rubinow and J. Keller, "The Transverse Force on a Spinning Sphere Moving in a Viscous Fluid", *J Fluid Mech* **11**, 447 (1961).

[6] P. G. T. Saffman, "The Lift on a Small Sphere in a Slow Shear Flow", *J. Fluid Mech.* **22**, 385 (1965).

[7] B. P. Ho and L. G. Leal, "Inertial Migration of Rigid Spheres in Two-Dimensional Unidirectional Flows", *J Fluid Mech* **65**, 365 (1974).

[8] J. A. Schonberg and E. J. Hinch, "Inertial Migration of a Sphere in Poiseuille Flow", *J. Fluid Mech.* **203**, 517 (1989).

[9] C. Bächer, L. Schrack, and S. Gekle, "Clustering of Microscopic Particles in Constricted Blood Flow", *Phys. Rev. Fluids* **2**, 013102 (2017).

[10] T. Krüger, D. Holmes, and P. V. Coveney, "Deformability-Based Red Blood Cell Separation in Deterministic Lateral Displacement Devices—A Simulation Study", *Biomicrofluidics* **8**, 054114 (2014).

[11] J.-T. Wang, J. Wang, and J.-J. Han, "Fabrication of Advanced Particles and Particle-Based Materials Assisted by Droplet-Based Microfluidics", *Small* **7**, 1728 (2011).

[12] T. M. Squires and S. R. Quake, "Microfluidics: Fluid Physics at the Nanoliter Scale", *Rev. Mod. Phys.* **77**, 977 (2005).

[13] E. Sollier, C. Murray, P. Maoddi, and D. Di Carlo, "Rapid Prototyping Polymers for Microfluidic Devices and High Pressure Injections", *Lab Chip* **11**, 3752 (2011).

[14] G. M. Whitesides, "The Origins and the Future of Microfluidics", *Nature* **442**, 368 (2006).

[15] D. Di Carlo, J. F. Edd, K. J. Humphry, H. A. Stone, and M. Toner, "Particle Segregation and Dynamics in Confined Flows", *Phys. Rev. Lett.* **102**, 094503 (2009).

[16] S. C. Hur, N. K. Henderson-MacLennan, E. R. B. McCabe, and D. Di Carlo, "Deformability-Based Cell Classification and Enrichment Using Inertial Microfluidics", *Lab. Chip* **11**, 912 (2011).

[17] G. Y. H. Lee and C. T. Lim, "Biomechanics Approaches to Studying Human Diseases", *Trends Biotechnol.* **25**, 111 (2007).

[18] S. Suresh, J. Spatz, J. P. Mills, A. Micoulet, M. Dao, C. T. Lim, M. Beil, and T. Seufferlein, "Connections between Single-Cell Biomechanics and Human Disease States: Gastrointestinal Cancer and Malaria", *Acta Biomater.* **1**, 15 (2005).

[19] S. Suresh, "Biomechanics and Biophysics of Cancer Cells", *Acta Biomater* **3**, 413 (2007).

[20] J. Guck, S. Schinkinger, B. Lincoln, F. Wottawah, S. Ebert, M. Romeyke, D. Lenz, H. M. Erickson, R. Ananthakrishnan, D. Mitchell, J. Käs, S. Ulvick, and C. Bilby, "Optical Deformability as an Inherent Cell Marker for Testing Malignant Transformation and Metastatic Competence", *Biophys. J.* **88**, 3689 (2005).

[21] H. A. Cranston, C. W. Boylan, G. L. Carroll, S. P. Sutera, Williamson, I. Y. Gluzman, and D. J. Krogstad, "Plasmodium Falciparum Maturation Abolishes Physiologic Red Cell Deformability", *Science* **223**, 400 (1984).

[22] J. Guck and E. R. Chilvers, "Mechanics Meets Medicine", *Sci. Transl. Med.* **5**, 212fs41 (2013).

[23] A. Mietke, O. Otto, S. Girardo, P. Rosendahl, A. Taubenberger, S. Golfier, E. Ulbricht, S. Aland, J. Guck, and E. Fischer-Friedrich, "Extracting Cell Stiffness from Real-Time Deformability Cytometry: Theory and Experiment", *Biophys. J.* **109**, 2023 (2015).

[24] Y. Deng, S. P. Davis, F. Yang, K. S. Paulsen, M. Kumar, R. Sinnott DeVaux, X. Wang, D. S. Conklin, A. Oberai, J. I. Herschkowitz, and A. J. Chung, "Inertial Microfluidic Cell Stretcher (iMCS): Fully Automated, High-Throughput, and Near Real-Time Cell Mechanotyping", *Small* **13**, 1700705 (2017).

[25] Z. T. F. Yu, K. M. A. Yong, and J. Fu, "Microfluidic Blood Cell Sorting: Now and Beyond", *Small* **10**, 1687 (2014).

[26] M. Dhar, E. Pao, C. Renier, D. E. Go, J. Che, R. Montoya, R. Conrad, M. Matsumoto, K. Heirich, M. Triboulet, J. Rao, S. S. Jeffrey, E. B. Garon, J. Goldman, N. P. Rao, R. Kulkarni, E. Sollier-Christen, and D. Di Carlo, "Label-Free Enumeration, Collection and Downstream Cytological and Cytogenetic Analysis of Circulating Tumor Cells", *Sci. Rep.* **6**, 35474 (2016).

[27] A. J. Mach and D. Di Carlo, "Continuous Scalable Blood Filtration Device Using Inertial Microfluidics", *Biotechnol. Bioeng.* **107**, 302 (2010).

[28] M. Dhar, J. N. Lam, T. Walser, S. M. Dubinett, M. B. Rettig, and D. Di Carlo, "Functional Profiling of Circulating Tumor Cells with an Integrated Vortex Capture and Single-Cell Protease Activity Assay", *Proc. National Acad. Sci.* **115**, 9986 (2018).

[29] J. Che, V. Yu, E. B. Garon, J. W. Goldman, and D. Di Carlo, "Biophysical Isolation and Identification of Circulating Tumor Cells", *Lab on a Chip* **17**, 1452 (2017).

[30] J. F. Edd, D. Di Carlo, K. J. Humphry, S. Köster, D. Irimia, D. A. Weitz, and M. Toner, "Controlled Encapsulation of Single-Cells into Monodisperse Picolitre Drops", *Lab Chip* **8**, 1262 (2008).

[31] M. Li, M. van Zee, K. Goda, and D. Di Carlo, "Size-Based Sorting of Hydrogel Droplets Using Inertial Microfluidics", *Lab on a Chip* **18**, 2575 (2018).

[32] J.-P. Matas, J. F. Morris, and É. Guazzelli, "Inertial Migration of Rigid Spherical Particles in Poiseuille Flow", *J. Fluid Mech.* **515**, 171 (2004).

[33] A. A. S. Bhagat, S. S. Kuntaegowdanahalli, and I. Papautsky, "Continuous Particle Separation in Spiral Microchannels Using Dean Flows and Differential Migration", *Lab. Chip* **8**, 1906 (2008).

[34] B. Chun and A. J. C. Ladd, "Inertial Migration of Neutrally Buoyant Particles in a Square Duct: An Investigation of Multiple Equilibrium Positions", *Phys. Fluids* **18**, 031704 (2006).

[35] C. Prohm, M. Gierlak, and H. Stark, "Inertial Microfluidics with Multi-Particle Collision Dynamics", *Eur. Phys. J. E* **35**, 80 (2012).

[36] T. Krüger, B. Kaoui, and J. Harting, "Interplay of Inertia and Deformability on Rheological Properties of a Suspension of Capsules", *J. Fluid Mech.* **751**, 725 (2014).

[37] J. Zhou and I. Papautsky, "Fundamentals of Inertial Focusing in Microchannels", *Lab Chip* **13**, 1121 (2013).

[38] C. Prohm and H. Stark, "Feedback Control of Inertial Microfluidics Using Axial Control Forces", *Lab. Chip* **14**, 2115 (2014).

[39] J. P. Matas, J. F. Morris, and E. Guazzelli, "Lateral Forces on a Sphere", *Oil Gas Sci. Technol.* **59**, 59 (2004).

[40] J.-P. Matas, V. Glezer, É. Guazzelli, and J. F. Morris, "Trains of Particles in Finite-Reynolds-Number Pipe Flow", *Phys. Fluids* **16**, 4192 (2004).

[41] K. J. Humphry, P. M. Kulkarni, D. A. Weitz, J. F. Morris, and H. A. Stone, "Axial and Lateral Particle Ordering in Finite Reynolds Number Channel Flows", *Phys. Fluids* **22**, 081703 (2010).

[42] S. Kahkeshani, H. Haddadi, and D. Di Carlo, "Preferred Interparticle Spacings in Trains of Particles in Inertial Microchannel Flows", *J. Fluid Mech.* **786**, R3 (2016).

[43] Y. Gao, P. Magaud, L. Baldas, C. Lafforgue, M. Abbas, and S. Colin, "Self-Ordered Particle Trains in Inertial Microchannel Flows", *Microfluid. Nanofluid* **21**, 154 (2017).

[44] Z. Pan, R. Zhang, C. Yuan, and H. Wu, "Direct Measurement of Microscale Flow Structures Induced by Inertial Focusing of Single Particle and Particle Trains in a Confined Microchannel", *Phys. Fluids* **30**, 102005 (2018).

[45] Y. Gao, P. Magaud, C. Lafforgue, S. Colin, and L. Baldas, "Inertial Lateral Migration and Self-Assembly of Particles in Bidisperse Suspensions in Microchannel Flows", *Microfluid. Nanofluidics* **23**, 93 (2019).

[46] K. Hood and M. Roper, "Pairwise Interactions in Inertially Driven One-Dimensional Microfluidic Crystals", *Phys. Rev. Fluids* **3**, 094201 (2018).

[47] W. Lee, H. Amini, H. A. Stone, and D. Di Carlo, "Dynamic Self-Assembly and Control of Microfluidic Particle Crystals", *Proc. Natl. Acad. Sci.* **107**, 22413 (2010).

[48] R. Skalak, A. Tozeren, R. P. Zarda, and S. Chien, "Strain Energy Function of Red Blood Cell Membranes", *Biophys. J.* **13**, 245 (1973).

[49] D. Barthès-Biesel, "Motion and Deformation of Elastic Capsules and Vesicles in Flow", *Annu. Rev. Fluid Mech.* **48**, 25 (2016).

[50] P. Bagchi, "Mesoscale Simulation of Blood Flow in Small Vessels", *Biophys. J.* **92**, 1858 (2007).

[51] D. Bell, C. Wongsrichanalai, and J. W. Barnwell, "Ensuring Quality and Access for Malaria Diagnosis: How Can It Be Achieved?", *Nat. Rev. Microbiol.* **4**, S7 (2006).

[52] J. Zhang, S. Yan, D. Yuan, G. Alici, N.-T. Nguyen, M. E. Warkiani, and W. Li, "Fundamentals and Applications of Inertial Microfluidics: A Review", *Lab Chip* **16**, 10 (2015).

[53] D. Di Carlo, D. Irimia, R. G. Tompkins, and M. Toner, "Continuous Inertial Focusing, Ordering, and Separation of Particles in Microchannels", *PNAS* **104**, 18892 (2007).

[54] D. Di Carlo, "Inertial Microfluidics", *Lab. Chip* **9**, 3038 (2009).

[55] H. Amini, W. Lee, and D. Di Carlo, "Inertial Microfluidic Physics", *Lab. Chip* **14**, 2739 (2014).

[56] O. Otto, P. Rosendahl, A. Mietke, S. Golfier, C. Herold, D. Klaue, S. Girardo, S. Pagliara, A. Ekpenyong, A. Jacobi, M. Wobus, N. Töpfner, U. F. Keyser, J. Mansfeld, E. Fischer-Friedrich, and J. Guck, "Real-Time Deformability Cytometry: On-the-Fly Cell Mechanical Phenotyping", *Nat. Methods* **12**, 199 (2015).

[57] F. P. Incropera, A. S. Lavine, T. L. Bergman, and D. P. DeWitt, *Fundamentals of heat and mass transfer*, Wiley, 2007.

[58] E. M. Purcell, "Life at Low Reynolds Number", *Am. J. Phys.* **45**, 3 (1977).

[59] R. Vernekar and T. Krüger, "Breakdown of Deterministic Lateral Displacement Efficiency for Non-Dilute Suspensions: A Numerical Study", *Med. Eng. Phys.* **37**, 845 (2015).

[60] H. W. Hou, A. A. S. Bhagat, A. G. Lin Chong, P. Mao, K. S. Wei Tan, J. Han, and C. T. Lim, "Deformability Based Cell Margination—A Simple Microfluidic Design for Malaria-Infected Erythrocyte Separation", *Lab. Chip* **10**, 2605 (2010).

[61] A. H. Raffiee, S. Dabiri, and A. M. Ardekani, "Elasto-Inertial Migration of Deformable Capsules in a Microchannel", *Biomicrofluidics* **11**, 064113 (2017).

[62] D. Stoecklein and D. Di Carlo, "Nonlinear Microfluidics", *Anal. Chem.* **91**, 296 (2019).

[63] D. Yuan, Q. Zhao, S. Yan, S.-Y. Tang, G. Alici, J. Zhang, and W. Li, "Recent Progress of Particle Migration in Viscoelastic Fluids", *Lab. Chip* **18**, 551 (2018).

[64] G. Segre and A. Silberberg, "Behavior of Macroscopic Rigid Spheres in Poiseuille Flow. Part 2: Experimental Results and Interpretation", *J Fluid Mech* **14**, 136 (1962).

[65] G. Segré and A. Silberberg, "Behaviour of Macroscopic Rigid Spheres in Poiseuille Flow Part 1. Determination of Local Concentration by Statistical Analysis of Particle Passages through Crossed Light Beams", *J. Fluid Mech.* **14**, 115 (1962).

[66] S. N. Sahasrabudhe, V. Rodriguez-Martinez, M. O'Meara, and B. E. Farkas, "Density, Viscosity, and Surface Tension of Five Vegetable Oils at Elevated Temperatures: Measurement and Modeling", *Int. J. Food Prop.*, 1 (2017).

[67] A. A. S. Bhagat, S. S. Kuntaegowdanahalli, and I. Papautsky, "Enhanced Particle Filtration in Straight Microchannels Using Shear-Modulated Inertial Migration", *Phys. Fluids* **20**, 101702 (2008).

[68] A. A. S. Bhagat, S. S. Kuntaegowdanahalli, and I. Papautsky, "Inertial Microfluidics for Continuous Particle Filtration and Extraction", *Microfluid. Nanofluidics* **7**, 217 (2009).

[69] T. Krüger, H. Kusumaatmaja, A. Kuzmin, O. Shardt, G. Silva, and E. M. Viggen, *The Lattice Boltzmann Method: Principles and Practice*, Springer International Publishing, 2017.

[70] P. Thompson, *Compressible-Fluid Dynamics*, 1988.

[71] L. Landau and E. Lifshitz, *Hydrodynamik*, Akadamie Verlag, 1991.

[72] M. Greenspan and C. Tschiegg, "Speed of Sound in Water by a Direct Method", *J. Res. National Bureau Stand.* **59**, 249 (1957).

[73] H. Bruus, *Theoretical Microfluidics*, Oxford University Press, 2008.

[74] G. Batchelor, *An Introduction to Fluid Dynamics*, Cambridge University Press, 2000.

[75] S. Kim and S. J. Karrila, *Microhydrodynamics: Principles and Selected Applications*, Dover Publications, 2005.

[76] P. Joseph and P. Tabeling, "Direct Measurement of the Apparent Slip Length", *Phys. Rev. E* **71**, 035303 (2005).

[77] D. C. Tretheway and C. D. Meinhart, "Apparent Fluid Slip at Hydrophobic Microchannel Walls", *Phys. Fluids* **14**, L9 (2002).

[78] L. Landau and E. Lifshitz, *Mechanics*, Elsevier Science, 1982.

[79] G. G. Stokes *et al.*, *On the effect of the internal friction of fluids on the motion of pendulums*, vol. 9. Pitt Press Cambridge, 1851.

[80] C. Oseen, *Über Die Stoke'sche Formel Und Über Eine Verwandte Aufgabe in Der Hydrodynamik: Mitteilung 2*, Almqvist & Wiksell, 1911.

[81] H. A. Lorentz, *Abhandlungen Über Theoretische Physik*, B.G. Teubner, 1907.

[82] H. Faxén, "Der Widerstand gegen die Bewegung einer starren Kugel in einer zähen Flüssigkeit, die zwischen zwei parallelen ebenen Wänden eingeschlossen ist", *Ann. der Physik* **373**, 89 (1922).

[83] J. K. G. Dohnt, *An Introduction to Dynamics of Colloids*, Elsevier, 1996.

[84] C. Prohm, "Control of Inertial Microfluidics", Doctoral thesis, Technische Universität Berlin, 2014.

[85] F. P. Bretherton, "The Motion of Rigid Particles in a Shear Flow at Low Reynolds Number", *J. Fluid Mech.* **14**, 284 (1962).

[86] J. D. Jackson and J. D. Jackson, *Classical Electrodynamics*, vol. 3. Wiley New York etc., 1962.

[87] P. G. T. Saffman, "The Lift on a Small Sphere in a Slow Shear Flow - Corrigendum", *J. Fluid Mech.* **31**, 624 (1968).

[88] Y. W. Kim and J. Y. Yoo, "Axisymmetric Flow Focusing of Particles in a Single Microchannel", *Lab. Chip* **9**, 1043 (2009).

[89] L. Zeng, S. Balachandar, and P. Fischer, "Wall-Induced Forces on a Rigid Sphere at Finite Reynolds Number", *J. Fluid Mech.* **536**, 1 (2005).

[90] P. Cherukat and J. B. McLaughlin, "The Inertial Lift on a Rigid Sphere in a Linear Shear Flow Field near a Flat Wall", *J. Fluid Mech.* **263**, 1 (1994).

[91] C. Liu, G. Hu, X. Jiang, and J. Sun, "Inertial Focusing of Spherical Particles in Rectangular Microchannels over a Wide Range of Reynolds Numbers", *Lab Chip* **15**, 1168 (2015).

[92] E. S. Asmolov, "The Inertial Lift on a Spherical Particle in a Plane Poiseuille Flow at Large Channel Reynolds Number", *J. Fluid Mech.* **381**, 63 (1999).

[93] K. Hood, S. Lee, and M. Roper, "Inertial Migration of a Rigid Sphere in Three-Dimensional Poiseuille Flow", *J. Fluid Mech.* **765**, 452 (2015).

[94] P. C.-H. Chan and L. G. Leal, "The Motion of a Deformable Drop in a Second-Order Fluid", *J. Fluid Mech.* **92**, 131 (1979).

[95] R. Fåhræus and T. Lindqvist, "The Viscosity of the Blood in Narrow Capillary Tubes", *Am. J. Physiol. Content* **96**, 562 (1931).

[96] D. Abreu, M. Levant, V. Steinberg, and U. Seifert, "Fluid Vesicles in Flow", *Adv. Colloid Interface Sci.* **208**, 129 (2014).

[97] C. Dupont, A.-V. Salsac, D. Barthès-Biesel, M. Vidrascu, and P. Le Tallec, "Influence of Bending Resistance on the Dynamics of a Spherical Capsule in Shear Flow", *Phys. Fluids* **27**, 051902 (2015).

[98] T. Krüger, *Computer Simulation Study of Collective Phenomena in Dense Suspensions of Red Blood Cells under Shear*, Springer Spektrum, 2012.

[99] S. Shrivastava and J. Tang, "Large Deformation Finite Element Analysis of Non-Linear Viscoelastic Membranes with Reference to Thermoforming:" *The J. Străin Anal. for Eng. Des.* (1993).

[100]   P. B. Canham, "The Minimum Energy of Bending as a Possible Explanation of the Biconcave Shape of the Human Red Blood Cell", *J. Theor. Biol.* **26**, 61 (1970).

[101]   W. Helfrich, "Elastic Properties of Lipid Bilayers: Theory and Possible Experiments", *Z Naturforsch C* **28**, 693 (1973).

[102]   G. Gompper and D. M. Kroll, "Random Surface Discretizations and the Renormalization of the Bending Rigidity", *J. Phys. I France* **6**, 1305 (1996).

[103]   M. Deserno, "Fluid Lipid Membranes: From Differential Geometry to Curvature Stresses", *Chem. Phys. Lipids* **185**, 11 (2015).

[104]   A. Guckenberger, M. P. Schraml, P. G. Chen, M. Leonetti, and S. Gekle, "On the Bending Algorithms for Soft Objects in Flows", *Comput. Phys. Commun.* **207**, 1 (2016).

[105]   J. L. McWhirter, H. Noguchi, and G. Gompper, "Ordering and Arrangement of Deformed Red Blood Cells in Flow through Microcapillaries", *New J. Phys.* **14**, 085026 (2012).

[106]   A. Helmy and D. Barthes-Biesel, "Migration of a Spherical Capsule Freely Suspended in an Unbounded Parabolic Flow", *J Mec. Theor. Appl.* **1**, 859 (1982).

[107]   G. I. Taylor, "The Formation of Emulsions in Definable Fields of Flow", *Proc. R. Soc. Lond. Math. Phys. Eng. Sci.* **146**, 501 (1934).

[108]   S. Ramanujan and C. Pozrikidis, "Deformation of Liquid Capsules Enclosed by Elastic Membranes in Simple Shear Flow: Large Deformations and the Effect of Fluid Viscosities", *J. Fluid Mech.* **361**, 117 (1998).

[109]   D. Barthes-Biesel and J. M. Rallison, "The Time-Dependent Deformation of a Capsule Freely Suspended in a Linear Shear Flow", *J. Fluid Mech.* **113**, 251 (1981).

[110]   P. A. Thompson, *Compressible-Fluid Dynamics*, McGraw-Hill, 1971.

[111]   B. Dünweg and A. J. Ladd. "Lattice Boltzmann Simulations of Soft Matter Systems". In: *Advances in Polymer Science*. Advances in Polymer Science. Springer Berlin Heidelberg, 2008, pp. 1–78.

[112]   P. L. Bhatnagar, E. P. Gross, and M. Krook, "A Model for Collision Processes in Gases. I. Small Amplitude Processes in Charged and Neutral One-Component Systems", *Phys. Rev.* **94**, 511 (1954).

[113]   X. Shan, X.-F. Yuan, and H. Chen, "Kinetic Theory Representation of Hydrodynamics: A Way beyond the Navier–Stokes Equation", *J. Fluid Mech.* **550**, 413 (2006).

[114]   R. Rubinstein and L.-S. Luo, "Theory of the Lattice Boltzmann Equation: Symmetry Properties of Discrete Velocity Sets", *Phys. Rev. E* **77**, 036709 (2008).

[115]   S. Wolfram, "Cellular Automaton Fluids 1: Basic Theory", *J. Stat. Phys.* **45**, 471 (1986).

[116]   U. Frisch, B. Hasslacher, and Y. Pomeau, "Lattice-Gas Automata for the Navier-Stokes Equation", *Phys Rev Lett* **56**, 1505 (1986).

[117] S. Chen and G. D. Doolen, "Lattice Boltzmann Method for Fluid Flows", *Annu. Rev. Fluid Mech.* **30**, 329 (1998).

[118] D. dHumieres, I. Ginzburg, M. Krafczyk, P. Lallemand, L.-S. Luo, and D. M. Bushnell, "Multiple-Relaxation-Time Lattice Boltzmann Models in 3D", *ICASE-2002-20* (2002).

[119] J. Latt and B. Chopard, "Lattice Boltzmann Method with Regularized Pre-Collision Distribution Functions", *Math. Comput. Simul.* **72**, 165 (2006).

[120] S. Ansumali, "Minimal Kinetic Modeling of Hydrodynamics", Doctoral thesis, ETH Zurich, 2004.

[121] Z. Guo, C. Zheng, and B. Shi, "Discrete Lattice Effects on the Forcing Term in the Lattice Boltzmann Method", *Phys. Rev. E* **65**, 046308 (2002).

[122] S. Chapman and T. Cowling, *The Mathematical Theory of Non-Uniform Gases: An Account of the Kinetic Theory of Viscosity, Thermal Conduction and Diffusion in Gases*, Cambridge University Press, 1970.

[123] R. Du, B. Shi, and X. Chen, "Multi-Relaxation-Time Lattice Boltzmann Model for Incompressible Flow", *Phys. Lett. A* **359**, 564 (2006).

[124] C. M. Bender and S. A. Orszag, *Advanced Mathematical Methods for Scientists and Engineers I: Asymptotic Methods and Perturbation Theory*, Springer-Verlag, 1999.

[125] J. Latt, B. Chopard, O. Malaspinas, M. Deville, and A. Michler, "Straight Velocity Boundaries in the Lattice Boltzmann Method", *Phys Rev E* **77**, 056703 (2008).

[126] J. Latt, "Hydrodynamic Limit of Lattice Boltzmann Equations", Doctoral thesis, University of Geneva, 2007.

[127] Z. Guo, C. Zheng, and B. Shi, "An Extrapolation Method for Boundary Conditions in Lattice Boltzmann Method", *Phys. Fluids* **14**, 2007 (2002).

[128] E.-J. Ding and C. K. Aidun, "Extension of the Lattice-Boltzmann Method for Direct Simulation of Suspended Particles Near Contact", *J. Stat. Phys.* **112**, 685 (2003).

[129] C. S. Peskin, "Flow Patterns around Heart Valves: A Digital Computer Method to Solve the Equations of Motion", PhD thesis, Albert Eistein College of Medicine, 1972.

[130] Z.-G. Feng and E. E. Michaelides, "The Immersed Boundary-Lattice Boltzmann Method for Solving Fluid–Particles Interaction Problems", *J. Comput. Phys.* **195**, 602 (2004).

[131] C. S. Peskin, "The Immersed Boundary Method", *Acta Numer.* **11**, 479 (2002).

[132] T. Krüger, F. Varnik, and D. Raabe, "Efficient and Accurate Simulations of Deformable Particles Immersed in a Fluid Using a Combined Immersed Boundary Lattice Boltzmann Finite Element Method", *Comput. Math. Appl.* **61**, 3485 (2011).

[133] C. Pan, L.-S. Luo, and C. T. Miller, "An Evaluation of Lattice Boltzmann Schemes for Porous Medium Flow Simulation", *Comput. & Fluids* **35**, 898 (2006).

[134] K. Suzuki and T. Inamuro, "Effect of Internal Mass in the Simulation of a Moving Body by the Immersed Boundary Method", *Comput. & Fluids* **49**, 173 (2011).

[135] Z.-G. Feng and E. E. Michaelides, "Robust Treatment of No-Slip Boundary Condition and Velocity Updating for the Lattice-Boltzmann Simulation of Particulate Flows", *Comput. Fluids* **38**, 370 (2009).

[136] X. Yang, X. Zhang, Z. Li, and G.-W. He, "A Smoothing Technique for Discrete Delta Functions with Application to Immersed Boundary Method in Moving Boundary Simulations", *J. Comput. Phys.* **228**, 7821 (2009).

[137] T. Inamuro, "Lattice Boltzmann Methods for Moving Boundary Flows", *Fluid Dyn. Res.* **44**, 024001 (2012).

[138] M. P. Allen, D. J. Tildesley, *et al.*, *Computer Simulation of Liquids*, Clarendon press Oxford, 1987.

[139] K. J. Åström and R. M. Murray, *Feedback Systems: An Introduction for Scientists and Engineers*, Princeton University Press, 2008.

[140] *The Palabos Project*, version 1.4, `http://www.palabos.org/`.

[141] S. Reddig and H. Stark, "Nonlinear Dynamics of Spherical Particles in Poiseuille Flow under Creeping-Flow Condition", *J Chem Phys* **138**, 234902 (2013).

[142] G. K. Batchelor and J. T. Green, "The Hydrodynamic Interaction of Two Small Freely-Moving Spheres in a Linear Flow Field", *J. Fluid Mech.* **56**, 375 (1972).

[143] G. Subramanian and D. L. Koch, "Centrifugal Forces Alter Streamline Topology and Greatly Enhance the Rate of Heat and Mass Transfer from Neutrally Buoyant Particles to a Shear Flow", *Phys. Rev. Lett.* **96**, 134503 (2006).

[144] G. Subramanian and D. L. Koch, "Inertial Effects on the Transfer of Heat or Mass from Neutrally Buoyant Spheres in a Steady Linear Velocity Field", *Phys. Fluids* **18**, 073302 (2006).

[145] C. Dietsche, B. R. Mutlu, J. F. Edd, P. Koumoutsakos, and M. Toner, "Dynamic Particle Ordering in Oscillatory Inertial Microfluidics", *Microfluid. Nanofluid* **23**, 83 (2019).

[146] P. M. Kulkarni and J. F. Morris, "Pair-Sphere Trajectories in Finite-Reynolds-Number Shear Flow", *J. Fluid Mech.* **596**, 413 (2008).

[147] A. De Rosis, S. Ubertini, and F. Ubertini, "A Comparison Between the Interpolated Bounce-Back Scheme and the Immersed Boundary Method to Treat Solid Boundary Conditions for Laminar Flows in the Lattice Boltzmann Framework", *J Sci Comput.* **61**, 477 (2014).

[148] H. Diamant, "Hydrodynamic Interaction in Confined Geometries", *J. Phys. Soc. Jpn.* (2009).

[149] S. R. Bazaz, A. Mashhadian, A. Ehsani, S. C. Saha, T. Krüger, and M. Ebrahimi Warkiani, "Computational Inertial Microfluidics: A Review", *Lab on a Chip* **20**, 1023 (2020).

[150] A. A. S. Bhagat, S. S. Kuntaegowdanahalli, N. Kaval, C. J. Seliskar, and I. Papautsky, "Inertial Microfluidics for Sheath-Less High-Throughput Flow Cytometry", *Biomed Microdevices* **12**, 187 (2010).

[151] W. Tang, D. Tang, Z. Ni, N. Xiang, and H. Yi, "Microfluidic Impedance Cytometer with Inertial Focusing and Liquid Electrodes for High-Throughput Cell Counting and Discrimination", *Anal. Chem.* **89**, 3154 (2017).

[152] H. Haddadi, H. Naghsh-Nilchi, and D. Di Carlo, "Separation of Cancer Cells Using Vortical Microfluidic Flows", *Biomicrofluidics* **12**, 014112 (2018).

[153] A. Gupta, P. Magaud, C. Lafforgue, and M. Abbas, "Conditional Stability of Particle Alignment in Finite-Reynolds-Number Channel Flow", *Phys. Rev. Fluids* **3**, 114302 (2018).

[154] X. Hu, J. Lin, and X. Ku, "Inertial Migration of Circular Particles in Poiseuille Flow of a Power-Law Fluid", *Phys. Fluids* **31**, 073306 (2019).

[155] T. Beatus, T. Tlusty, and R. Bar-Ziv, "Phonons in a One-Dimensional Microfluidic Crystal", *Nat. Phys.* **2**, 743 (2006).

[156] U. D. Schiller, J.-B. Fleury, R. Seemann, and G. Gompper, "Collective Waves in Dense and Confined Microfluidic Droplet Arrays", *Soft Matter* **11**, 5850 (2015).

[157] J.-B. Fleury, U. D. Schiller, S. Thutupalli, G. Gompper, and R. Seemann, "Mode Coupling of Phonons in a Dense One-Dimensional Microfluidic Crystal", *New J. Phys.* **16**, 063029 (2014).

[158] T. Beatus, I. Shani, R. H. Bar-Ziv, and T. Tlusty, "Two-Dimensional Flow of Driven Particles: A Microfluidic Pathway to the Non-Equilibrium Frontier", *Chem Soc Rev* **46**, 5620 (2017).

[159] S. Claire Hur, H. T. Kwong Tse, and D. D. Carlo, "Sheathless Inertial Cell Ordering for Extreme Throughput Flow Cytometry", *Lab. Chip* **10**, 274 (2010).

[160] X. Hu, J. Lin, D. Chen, and X. Ku, "Stability Condition of Self-Organizing Staggered Particle Trains in Channel Flow", *Microfluid. Nanofluidics* **24** (2020).

[161] M. Reichert and H. Stark, "Circling Particles and Drafting in Optical Vortices", *J. Physics: Condens. Matter* **16**, S4085 (2004).

[162] P. J. A. Janssen, M. D. Baron, P. D. Anderson, J. Blawzdziewicz, M. Loewenberg, and E. Wajnryb, "Collective Dynamics of Confined Rigid Spheres and Deformable Drops", *Soft Matter* **8**, 7495 (2012).

[163] F. Risso, F. Collé-Paillot, and M. Zagzoule, "Experimental Investigation of a Bioartificial Capsule Flowing in a Narrow Tube", *J. Fluid Mech.* **547**, 149 (2006).

[164] D. Salac and M. J. Miksis, "Reynolds Number Effects on Lipid Vesicles", *J. Fluid Mech.* **711**, 122 (2012).

[165] S. K. Doddi and P. Bagchi, "Lateral Migration of a Capsule in a Plane Poiseuille Flow in a Channel", *Int. J. Multiph. Flow* **34**, 966 (2008).

[166] D.-K. Sun and Z. Bo, "Numerical Simulation of Hydrodynamic Focusing of Particles in Straight Channel Flows with the Immersed Boundary-Lattice Boltzmann Method", *Int. J. Heat Mass Transf.* **80**, 139 (2015).

[167] B. Kim, C. B. Chang, S. G. Park, and H. J. Sung, "Inertial Migration of a 3D Elastic Capsule in a Plane Poiseuille Flow", *Int. J. Heat Fluid Flow* **54**, 87 (2015).

[168] Z. Wang, Y. Sui, A.-V. Salsac, D. Barthès-Biesel, and W. Wang, "Motion of a Spherical Capsule in Branched Tube Flow with Finite Inertia", *J. Fluid Mech.* **806**, 603 (2016).

[169] A. Kilimnik, W. Mao, and A. Alexeev, "Inertial Migration of Deformable Capsules in Channel Flow", *Phys. Fluids* **23**, 123302 (2011).

[170] Y.-L. Chen, "Inertia- and Deformation-Driven Migration of a Soft Particle in Confined Shear and Poiseuille Flow", *RSC Adv* **4**, 17908 (2014).

[171] S. J. Shin and H. J. Sung, "Inertial Migration of an Elastic Capsule in a Poiseuille Flow", *Phys. Rev. E* **83**, 046321 (2011).

[172] D.-K. Sun, Y. Wang, A.-P. Dong, and B.-D. Sun, "A Three-Dimensional Quantitative Study on the Hydrodynamic Focusing of Particles with the Immersed Boundary – Lattice Boltzmann Method", *Int. J. Heat Mass Transf.* **94**, 306 (2016).

[173] J. Horwitz, P. Kumar, and S. Vanka, "Three-Dimensional Deformation of a Spherical Droplet in a Square Duct Flow at Moderate Reynolds Numbers", *Int. J. Multiph. Flow* **67**, 10 (2014).

[174] A. Förtsch, M. Laumann, D. Kienle, and W. Zimmermann, "Migration reversal of soft particles in vertical flows", *EPL* **119**, 64003 (2017).

[175] O. Aouane, A. Farutin, M. Thiébaud, A. Benyoussef, C. Wagner, and C. Misbah, "Hydrodynamic Pairing of Soft Particles in a Confined Flow", *Phys. Rev. Fluids* **2** (2017).

[176] Z. Shen, T. M. Fischer, A. Farutin, P. M. Vlahovska, J. Harting, and C. Misbah, "Blood Crystal: Emergent Order of Red Blood Cells Under Wall-Confined Shear Flow", *Phys. Rev. Lett.* **120**, 268102 (2018).